Optofluidic microreactor for the photocatalytic hydrogen generation via water splitting reaction

A Thesis

Submitted in Partial Fulfilment of the Requirement for the Degree of

DOCTOR OF PHILOSOPHY

By

PONNALA RAMBABU

Department of Chemical Engineering

Indian Institute of Technology Guwahati

Guwahati-781039, Assam, India.

2022

Dedicated To My Family & My Brother-in-law

Indian Institute of Technology Guwahati

Department of Chemical Engineering

Declaration

I certify that the work contained in this thesis entitled "Optofluidic microreactor for the photocatalytic hydrogen generation via water splitting reaction" is original and has been done by me at the Department of Chemical Engineering, Indian Institute of Technology Guwahati, Guwahati, India, under the supervision of Dr. Nageswara Rao Peela. The work has not been submitted to any other Institute for any degree or diploma. I have followed the guidelines provided by the Institute in preparing the thesis. I have confirmed to the norms and guidelines given in the Ethical Code of Conduct of the Institute. Whenever I have used materials (data, theoretical analysis, figures, and text) from other sources, I have given due credit to them by citing them in the text of the thesis and giving their details in the references. Further, I have taken permission from the copyright owners of the sources, whenever necessary.

Date: 21th November 2022
Place: IIT Guwahati

Ponnala Rambabu
(Research Scholar)
Roll No: 166107024
Department of Chemical Engineering
IIT Guwahati, Guwahati – 781039
Assam, India

Indian Institute of Technology Guwahati

Department of Chemical Engineering

Certificate

It is certified that the work described in this thesis entitled "Optofluidic microreactor for the photocatalytic hydrogen generation via water splitting reaction" by Ponnala Rambabu for the award of the degree of Doctor of Philosophy is an authentic record of the results obtained from the research work carried out under my supervision at the Department of Chemical Engineering, Indian Institute of Technology Guwahati, Guwahati, India, and this work has not been submitted elsewhere for a degree.

Dr. Nageswara Rao Peela

(Supervisor)

Associate Professor

Department of Chemical Engineering

IIT Guwahati, Guwahati – 781039

Assam, India

Acknowledgment

First and foremost, I feel it is a great privilege to express my deepest and most sincere gratitude to my supervisor Dr. Nageswara Rao Peela for his invaluable guidance, encouragement and support during my Ph.D. research work. His inspiring guidance, motivation and sincere advice have enabled me to overcome all the difficulties during my research. And I look forward to working with him and further developing our relationship.

I am grateful to Prof. Ramgopal V.S. Uppaluri, the Chairman of the Doctoral Committee, Department of Chemical Engineering, IIT Guwahati, for providing valuable suggestions on my work throughout the years. In addition, I want to express my sincere gratitude to Dr. Partho Sarathi Gooh Pattader and Dr. Pavan Kumar Kancharla, distinguished members of the Doctoral Committee, for giving their valuable suggestions and encouragement, which helped in the successful completion of this thesis. I also thank Prof. Kastubha Mohanty, Head of the Department of Chemical Engineering, for his administrative support. Furthermore, I would like to thank other faculty members and research scholars for supporting the Department of Chemical Engineering staff, IIT Guwahati, for their kind cooperation in all aspects.

I genuinely thank the fellowships offered by the Ministry of Human Resource Development (MHRD) and our institute for the duration of the Ph.D. programme. The analytical resources from Central Instruments Facilities (CIF) and the Department of Chemical Engineering of the Indian Institute of Technology Guwahati are also acknowledged. I would like to thank the Department of Science and Technology (DST), New Delhi, India, for partial financial support provided under Clean Energy Research Initiative (CERI) with Grant Number: DST/TM/CERI/C19(G).

I am thankful to my senior members from our group, Dr. Yedla Santosh Kumar, Dr. Mehboob Alam, and Dr. Devipriya Gogoi, for their encouragement and guidance. In addition, I want

thank my lab colleagues, Dr. Bharath, Mr. Prasad, Mr. Hanumanth, Mr. Ameer, Ms. Sarmistha Mr. Masresha and Mr. Prince for their contact, suggestions, and friendship.

I am thankful to my friends- Mukhesh, Dr. Vikas, Dr. Anasuya, Anuja, Prem, Kanishka, Sunil Kumar, Anirudha, Prerana, Rajashekar, Dr. Mallikarjun, Dr. Ramesh, Pruthvi Raj, Dr. Sathya Narayana, Anudeep, Pilli, Nagendra Prasad, Srinu, and Durga for their support and motivation throughout my research career at IIT Guwahati.

I also thank my close friends- Jithendar, Dr. Paul Praveen, Upendar, Shiva, Sushovan, Raghu, Bhaskar, Krishna Prasad, and Jithu for their lovely support.

Finally, I want to express my deepest gratitude and indebtedness to my parents (Rajaiah-Bhadramma) for giving me this life to explore myself and reach my aspirations while also teaching me priceless life lessons. In addition, I would like to thank my wife, Jyothsna, with the utmost pleasure. Her extensive longer patience and support gave me a lot of strength to finish my Ph.D and I keep my respect throughout my life. I also like to express my gratitude to my brother-in-law (Marapally Srikanth), my aunt (Marapally Thirupathi), and my uncle (Marapally Sampath) for their assistance. Above all, I am grateful to Almighty God for blessed me with my lovely children Jaswik Babu and Vigneswara Babu, they have made my life lovely.

PONNALA RAMBABU

Abstract

The increasing demand for energy and environmental concern lead to the exploration of renewable energy resources, among which, the solar energy is a prominent resource as its availability in more uniform across the globe. The hydrogen (H_2) is the most viable future energy carrier due to its high gravimetric energy density and non-polluting nature. The direct conversion of solar to green hydrogen via photocatalytic water splitting has a great potential and the optofluidic microreactors (OFMRs) are highly useful in this regard. The OFMRs in photocatalysis enables the concurrent and fine control of fluid flow, photon harvesting, and reaction with the shorter transfer path lengths. The design of the OFMR plays a significant role to stimulate the transport properties, which in turn improve the photocatalytic reaction performance. The OFMRs are being developed for several applications. However, due to complex and expensive fabrication, these devices are not well established in practical applications. In this study, we describe a simple, rapid, and inexpensive method to fabricate microchannels with various geometries on the glass substrate and tested them for the production of green hydrogen via photocatalytic water splitting reaction after coating with a sustainable photocatalyst.

For the fabrication of microchannels on glass substrate, we used adhesive tape as a mask, a surgical knife to make patterns, and wet chemical etching to remove unwanted parts from the glass. The adhesive tape as mask resulted in deeper channels (up to 550 µm), and higher etch factor (1.2) as compared to those obtained with UV photolithography. The semi-circular shaped microchannel with sharp edges and without any wall irregularities was obtained with adhesive tape as mask and using 49% HF solution as chemical etchant at room temperature for 120 min.

The CdS photocatalyst was coated, using sol-gel method, on OFMRs with various geometries, such as serpentine, planner and micropillered, and tested them for photocatalytic hydrogen

production. The effect of OFMR geometry, liquid flow rate (0.05 – 1 mL min^{-1}) and sacrificial reagent (SR, Na_2SO_3/Na_2S) concentration (0.05 – 0.5 M) on the hydrogen generation under visible light was studied. A higher H_2 production rate was observed with the serpentine OFMR as compared to that in planar and micropillared OFMRs. The serpentine OFMR, having higher surface-to-volume ratio, induced the micromixing that enhanced the mass transfer of the sacrificial reagent and resulted in higher H_2 formation. A maximum H_2 production rate of 2.65 µmol h^{-1} cm^{-2} was observed at a reactant flow rate of 1.0 mL min^{-1} and a sacrificial reagent (Na_2SO_3/Na_2S) concentration of 0.5 M. The laminar flow in microreactor limits the mixing. There is a necessity to enhance the mixing, which results in the mass transfer enhancement. The slugs creation by introducing inert gas is one possible way to enhance the internal circulation of reactant molecules over the photocatalyst. The serpentine OFMR was used for the gas-liquid photocatalytic hydrogen production. The effect of gas and liquid flow rates on the hydrogen production rate in the presence of 0.1 M SR (Na_2SO_3/Na_2S) under the UV light (254 nm) irradiation was investigated. A higher H_2 production rate (0.298 µmol h^{-1}) was observed at the gas and liquid flow rates of 1 and 0.8 mL min^{-1}, respectively. With increase of inert gas flow rate, the hydrogen evolution rate was increased at lower flow rates and then decreased with gas flow rate, reaching maximum at a flow rate of 0.8 mL min^{-1}. The increase of H_2 production rate at lower flow rates can be due to the enhanced mixing and mass transfer, while its decrease at higher flow rates was due to the gas phase occupying more photocatalyst active area.

An effective corrugated serpentine OFMR (C-SOFMR) with advanced features, such as expansion/contraction and wavy microstructures, was fabricated using the adhesive tape based method as described before. A flow visualization study reveals a laminar flow with no back mixing in plain serpentine OFMR (P-SOFMR), and stretching and folding of fluid along with back mixing in C-SOFMR. Further, the CdS nanowires on g-C_3N_4 nanosheet (CN/CdS)

heterojunction was synthesized *in situ* both P-SOFMR and C-SOFMR and utilized the device for the photocatalytic green hydrogen generation. The CN/CdS heterojunction endowed with narrow band gap energy (2.01 eV). The longer CdS nanowires (~110 nm) benefit the electronic interface with CN in the CN/CdS heterojunction and lead to the spatial separation (reduced recombination) of excitons along the CdS axial direction. The charges generated were utilized efficiently for the HER reaction in both P-SOFMR and C-SOFMR at higher flow rates attributing to the rapid micro-mixing and mass transfer. The CN/CdS2 heterojunction showed the highest photocatalytic activity (6.38 µmol h^{-1} in C-SOFMR and 6.16 µmol h^{-1} in P-SOFMR at 1.0 mL min^{-1}) due to its good optronic properties.

The new approach developed in this study is a step forward in fabricating highly efficient, advanced and inexpensive optofluidic microdevices for the green hydrogen production directly from solar energy.

Contents

List of Figures

List of Tables

Abbreviations

3D	Three-dimensional
BE	Binding Energy
CB	Conduction Band
CdS	Cadmium Sulfide
CN	g-C_3N_4
EDX	Electron Dispersive X-ray
FESEM	Field Emission Scanning Electron Microscope
FETEM	Field Emission Transmission Electron Microscope
FTIR	Fourier-transform Infrared
GC	Gas Chromatography
HEP	Hydrogen Evolution Photocatalyst
HER	Hydrogen Evolution reaction
HRTEM	High-resolution Transmission Electron Microscopy
LA	Lactic acid
NHE	Normal Hydrogen Electrode
OFMR	Optofluidic microreactor
P-SOFMR	Planar serpentine OFMR
C-SOFMR	Corrugated serpentine OFMR
PC	Photocatalyst
PL	Photoluminescence

SAED	Selected-area Electron Diffraction SPR Surface Plasmon Resonance
SR	Sacrificial Reagent
TEA	Triethanolamine
UV-vis	Ultraviolet-visible
VB	Valance Band
XPS	X-ray Photoelectron Spectroscopy
XRD	X-ray Powder Diffraction

Symbols

E_g	Bandgap Energy
µm	Micrometer
nm	Nanometer
Å	Angstrom
H_2	Hydrogen
O_2	Oxygen
E	Photon energy
h	Planck's constant
ν	Frequency
V	Volts
ΔG^{o}	Gibbs free energy
n_{H2}	H_2 evolution rate (mol s^{-1})
N_A	Avogadro's constant (6.022×10^{23} mol^{-1})

Publications

P. Rambabu, S. Patel, D. Gogoi, R.V. Uppaluri, and N.R. Peela, Optofluidic microreactor for the photocatalytic water splitting to produce green hydrogen, International Journal of Hydrogen Energy 47 (2022) 2152-2163.

P. Rambabu and N. R. Peela, In-situ synthesis of CN/CdS heterojunction construction in 3D-serpentine microreactor for the photocatalytic hydrogen generation from water, International Journal of Hydrogen Energy 48 (2023) 15406-15420.

P. Rambabu and N. R. Peela, Multiphase photocatalytic hydrogen generation via water splitting reaction in serpentine optofluidic microreactor (Manuscript is under preparation).

Conferences

P. Rambabu, and N. R. Peela, Multiphase photocatalytic hydrogen generation in optofluidic microreactor, 74th Annual Session of Indian Institute of Chemical Engineers CHEMCON-2021, Dec 2021.

P. Rambabu and N. R. Peela, Optofluidic microreactor for the photocatalytic water splitting to produce green hydrogen, ChemPlus 2022, IIT Madras.

Chapter 1

Background of the Work and Research Objectives

This chapter discusses the basic concepts of the photocatalytic water splitting reaction over the semiconductor. An inclusive review on the photo driven charge transportation dependence of the semiconductor optronic and chemical stability is described. Comparison between the traditional batch and OFMR is provided. A brief literature survey on glass fabrication and water splitting reaction in OFMR is given. Finally, the knowledge gaps and contests are concised and the research objectives are specified.

1

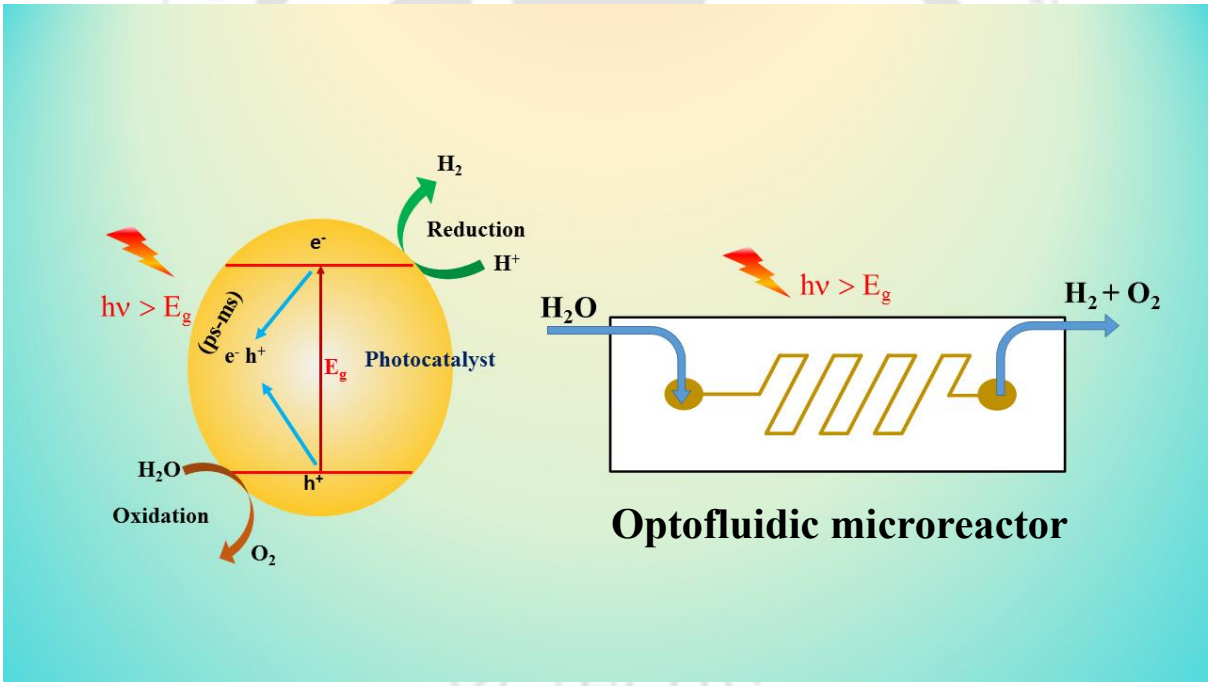

1.1 Energy outlook

Presently, 96% of energy demand of the world is met through fossil fuels resources, which leads to environmental pollution and results in long term energy crisis[1,2]. The increasing demand for energy and environmental concerns leads to the exploration of renewable energy resources, such as solar, wind, biomass and geothermal[3,4]. Among the renewable energy resources available, the solar energy is more prominent to substitute fossil fuels as its availability in more uniform across the globe[5]. Various solar to more useful energy conversion technologies are being developed or are in the commercial use. For example, solar to electrical energy and solar thermal technologies are already in commercial use. On the other hand, the technologies for the direct conversion of the solar to chemical energy (green hydrogen) are attracting intense research all over the world[6].

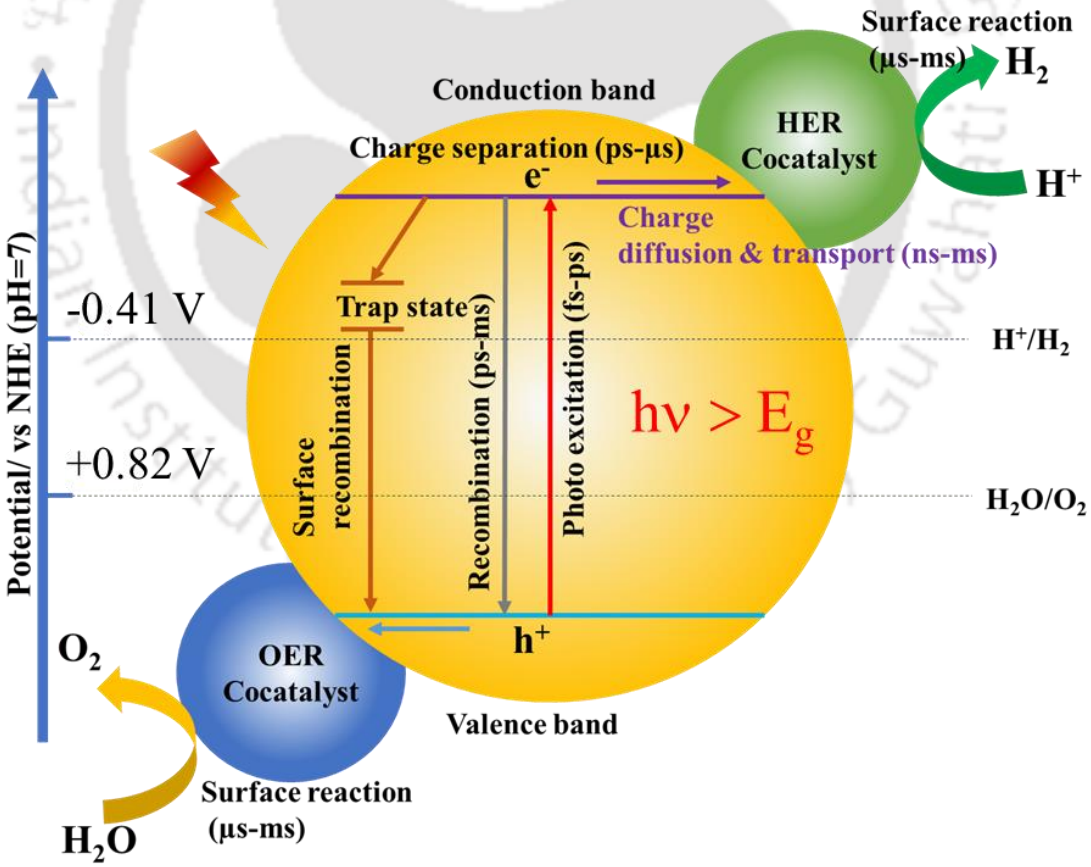

Figure 1.1: Photocatalytic water splitting mechanism on the photocatalyst.

Hydrogen is the most promising, efficient and clean energy carrier due to its environmental-friendly and non-polluting nature. Solar hydrogen energy production has the potential to supply sustainable green energy to the world's demand, replace the limited fossil fuels, and combat climate changes due to CO_2 emissions. The hydrogen (H_2) is the most viable future energy carrier[7]. The gravimetric higher heating value (HHV, 141.8 MJ kg^{-1}) and lower heating value (LHV, 120 MJ kg^{-1}) of H_2 are much greater than those of gasoline (46.5 and 43.3 MJ kg^{-1}) at 298 K. Currently, major portion of H_2 is being produced from the fossil fuels. The H_2 produced from fossil fuels without carbon capture is called the grey hydrogen and that produced with carbon capture is called the Blue hydrogen. While, the H_2 produced from renewable sources, such as solar and wind, is known as the green hydrogen. The green hydrogen production is a sustainable technology as the resources used are long lasting and sustainable. At present, the green hydrogen is being produced from solar energy in two steps: solar to electricity conversion followed by electrolysis of water to produce green hydrogen. This process is complex and produce some wastes[6,8,9,10,11]. Therefore, the photocatalytic conversion of solar to green hydrogen is a highly attractive alternative. However, the major hurdle in this technology in the poor solar-to-hydrogen conversion efficiency (STH)[12].

1.2 Photocatalytic water splitting

Fujishima-Honda discoverd the electrochemical water splitting to produce hydrogen and oxygen[13]. The water splitting reaction to produce H_2 and O_2 is a thermodynamically uphill reaction (ΔG° = 237.13 kJ mol^{-1}).

The overall water splitting reaction is as follows:

$$2H_2O \xrightarrow{h\nu} H_2 + O_2 \qquad \Delta G^0 = 237.13 \text{ kJ } mol^{-1} \qquad \mathbf{1.1}$$

The involved reactions are:

$$Photocatalyst \xrightarrow{hv} e^{-1} + h^{+} \quad \mathbf{1.2}$$

$$\textbf{\textit{Photoxidation}}: H_2O + h^{+} \rightarrow 2H^{+} + \frac{1}{2}O_2 \quad \mathbf{1.3}$$

$$\textbf{\textit{Photoreduction}}: 2H^{+} + 2e^{-1} \rightarrow H_2 \quad \mathbf{1.4}$$

The photocatalysts must have suitable band gap and edge potentials. The conduction and valence band edge potentials should be more negative and more positive, respectively, with respect to the reduction and oxidation potentials of water[14]. The minimum potential required for the reduction of H^+ to H_2 and for the oxidation of H_2O to O_2 are -0.41 and +0.82 V vs. NHE at pH 7 (**Figure 1.1)**. When the energy of the incident photon is greater than the band gap energy of photocatalyst, the electrons and holes are generated and the electrons are excited to the conduction band (CB) leaving holes in valence band. The photo driven excitons diffuse to the semiconductor surface to split the water into H_2 and O_2. Here, the separation of excitons plays an important role to reduce the recombination of electron and hole. Photocatalytic water splitting reaction activity/efficiency depends three major factors: 1) Photon absorption, 2) charge generation and separation, and 3) redox reactions on the photocatalyst surface.

1.2.1 Photon absorption

The photon absorption is influence by the light penetration depth and absorption by photocatalyst. The light penetration depth depends on the reactor design[15]. While, the absorption by photocatalyst depends on band gap and film thickness or particle size of the photocatalyst[16]. The light transfer length should be short and clear to avoid loss of incident photon due to the scattering and reflection[17]. In particulate photocatalysis, the light scattering is higher than the absorption due to the unsteady (movement of) photocatalyst which in turn leads to loss of energy. Fixed thin films of the desired thickness are effective at capturing light,

lengthening photon lifetimes through void resonance, and avoid the need for catalyst post-processing[18].

1.2.2 Photo driven electron and hole generation and separation

The photon absorption and generation of excitons depends on the semiconductor physical and electronic properties[19]. The semiconductor under light irradiation generates the excitons which need to be separated and used in the redox reactions otherwise recombines quickly. The recombination may occur in bulk or at surface at a time scale of picosecond to nanosecond (Figure 1). Surface states or defects of the semiconductor acts as the recombination centres. A defects free semiconductor with high active surface area and high crystallinity is beneficial to enhance the photo-activity. The semiconductor-semiconductor heterojunctions and metal-doping in semiconductor help in spatial separation of excitons[20]. The noble metals such as Pt, Ag, Ru, Au, Rh, and Ir interface with the semiconductor, form a Schottky barrier and reduces the activation energy that enhances the charge separation[21]. The noble metals also extends the visible light absorption due to local surface plasmon resonance (SPR). The doping of metals on the semiconductor structures such as rods, wires, cubes, and core-shell[22] enables efficient light harvesting and photosensitization of broader band gap materials such as TiO_2, $SrTiO_3$, and CdS. The alkali and alkaline earth metals are able to modify the crystal structure without affecting the band structure of semiconductor. The co-catalysts are majorly used to reduce the charge carrier recombination[23], improve the charge transfer kinetics and change reaction pathway. These act as an exciton scavenger and reaction sites for the redox reactions. The concentration of co-catalyst should be optimum. The lower concentrations result lower activity due to insufficient co-catalyst sites. The higher concentrations also result in lower activity but due to the blockage of active sites on the semiconductor and thus reducing its active surface area.

Semiconductor-semiconductor heterojunction interface enables the effective spatial separation of photo-generated charges[21]. Two semiconductors are owed to be different band structure, which can be band aligned. Three types of heterojunction are well known: Straggling gap (Type 1), Staggered gap (Type 2), and Broken gap (Type 3)[24,25]. In Type 1 heterojunction, the semiconductor I (SC I) have the higher CB and lower VB energy levels than the semiconductor II (SC II) and therefore, the migration of photo-generated electron and holes is from SC I to the SC II, under the light irradiation (**Figure 1.2a**). The charge separation and redox ability of Type 1 heterojunction are effective due to the accumulation of excitons and redox reactions on the lower potential semiconductor. In Type 2 heterojunction, SC II have the higher CB and VB energy levels than the SC II. The photo-generated electrons are transferred from SC I to SC II, and the holes are transferred from SC II to SC I (**Figure 1.2b**). The separation of excitons is effective in Type 2 than that in Type 1 heterojunction. However, the redox ability is high due to the fact that the redox reactions occur on the lower potential semiconductor. The charge-transfer mechanism in Type 3 heterojunction is similar to that of Type 2, but the band gaps of semiconductors do not overlap and, therefore, the photo generated charge carrier separation is not feasible (**Figure** 1.2**c**).

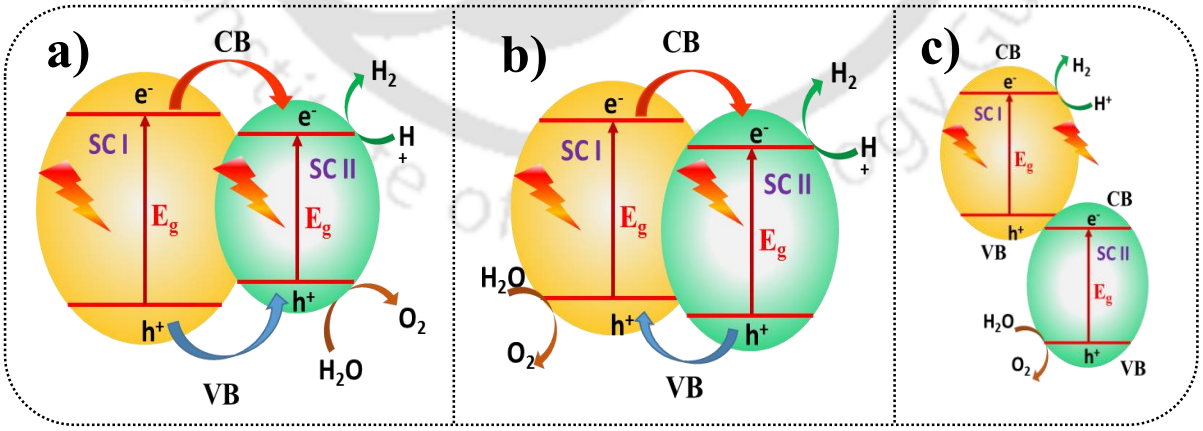

Figure 1.2: The photo-generated charge separation mechanisms in heterojunction-based photocatalysts: (a) Type 1, (b) Type 2, and (c) Type 3.

In 1979, Bard introduced the Z-scheme water splitting, motivated by the natural photosynthesis **Figure 1.3a**[26]. The two-step Z-scheme process utilizes the visible light and requires lower energy. The Z-scheme[27,28] is the combination of H_2 and O_2 evolution photocatalysts in presence of a redox mediator (acceptor/donor (A/D)) such as I^{3-}/I^-, Fe^{3+}/Fe^{2+}, and IO^{3-}/I^-. In this process, the D forms when A scavenge the electron from CB of the oxidation photocatalyst and A forms when D scavenge the hole from VB of the reduction photocatalyst[29]. The photo generated free electron reduces the water and the hole oxidizes the water to produce H_2 and O_2, respectively. Demerits of this process are the lower charge transfer rate due to slow ion pairs diffusion and light shielding effect of the ion pairs, which affects the utilization of light and the generation of photo-charge carriers by the semiconductor[30]. A direct contact between the two semiconductors in the presence of electron mediator (such as Ag, Pt, and Au) reduces the light shielding effect, enhances the charge transfer rates, and thus enhances the water splitting reaction[31,32] (**Figure 1.3b)**.

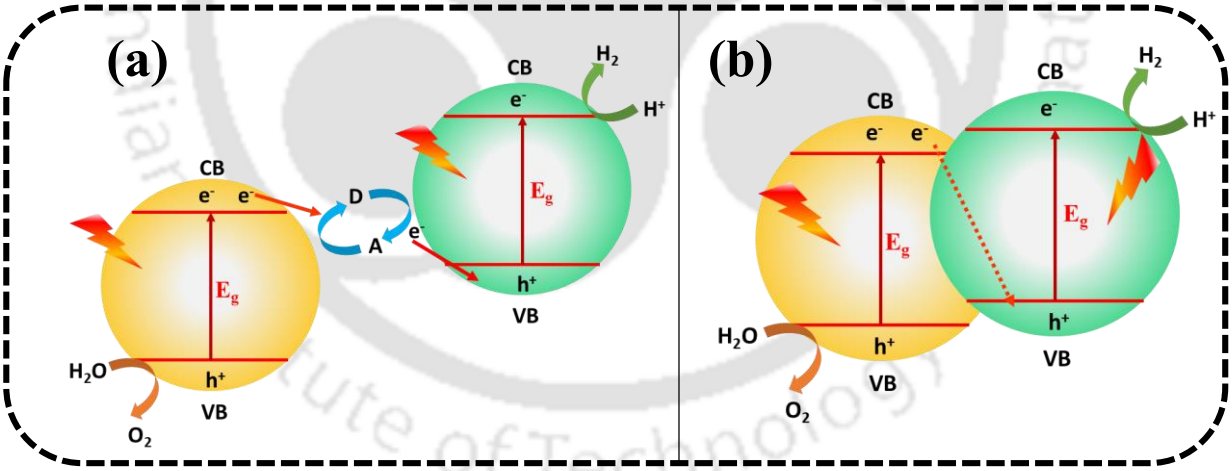

Figure 1.3: Electron-hole separation in (a) Conventional Z-scheme (b) Direct Z-scheme.

The photo-generated charge carrier scavengers reduce the recombination and back reaction of water splitting[33]. The inorganic scavengers, such as SO_3^{2-}/S^{2-}, I^-/IO^{3-}, and Ce^{4+}/Ce^{3+}, and the organic scavengers, such as methanol, ethanol, triethanolamine, and lactic acid, are able to scavenge holes from H_2 evolution photocatalysts[34,35]. The oxidizing agents, such as Ag^+ and Fe^{3+}, scavenge the electrons and support in the production of O_2 from water[36].

1.2.3 Redox reactions on surface

After light absorption, charge generation, and separation, the photogenerated charge carriers are to be utilized for the redox reactions[33]. The redox reactions occur at the interface between semiconductor and reactant. The mechanistic steps involved are reactant adsorption, surface reaction utilizing the excitons for the redox reactions, and products desorption. The overall efficiency of the surface redox reactions depends on the transport properties and surface reaction kinetics[37].

Pure water adsorption onto the catalyst is not a limiting step in the photocatalytic water splitting reaction. The decomposition of pure water is an inefficient process depending on the bandgap and band edge-potentials. In such cases, the external sacrificial reagents are added to the photo-reactor for improving the overall efficiency. In a batch reactor operation (**Figure 1.4a**), the photocatalyst is in suspension, an inert gas, such as nitrogen, is used as a sweep gas, and mechanical stirring for mixing of the reactants. This has disadvantages such as non-uniform light absorption, light scattering and larger penetration length. Moreover, oxidation or reduction of sacrificial reagents forms the intermediates that show the negative effect on catalyst activity. Therefore, the transport properties, such as mass transfer, light absorption, adsorption/desorption of reactants/products, should be enhanced to improve the efficiency of the overall process. In this context, the OFMRs are highly helpful.

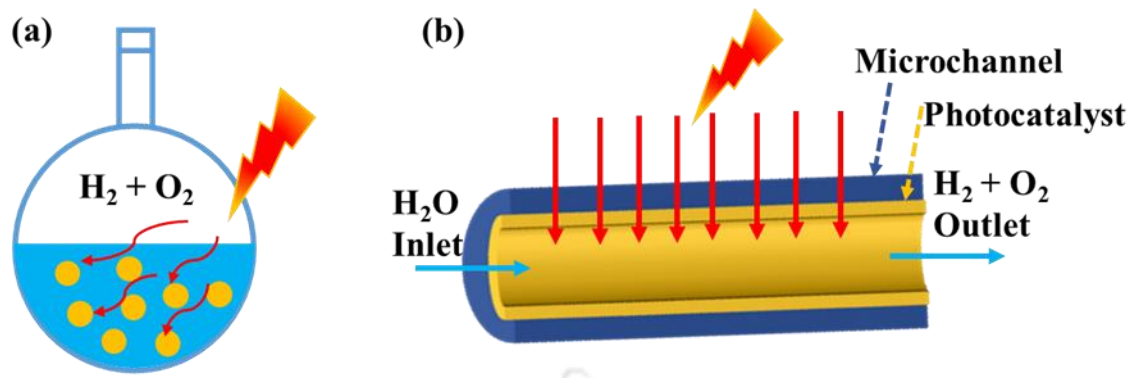

Figure 1.4: (a) Batch reactor (b) Optofluidic microreactor.

1.3 Optofluidic microreactor

The OFMR [38,39] is a multifunctional miniatured device[40,41] that integrates the functions of optics, microfluidics and reaction (**Figure 1.4b**). The energy conversion in microreactors is being explored rapidly. The micro-configuration overcomes several drawbacks of conventional batch reactors, such as longer processing time, poor selectivity and efficiency. This could be attributed to higher surface to volume ratio which in turn significantly reduces the mass and light diffusion path lengths. High surface to volume ratio of microreactor allows for the high amount of photocatalyst utilization[42] and provides uniform photon distribution. The microchannel shape plays a vital role in the confinement of fluids in the microchannel area. Semi-circular microchannels are regarded to be better than rectangular channels due to finer control of fluid flow.[43] The laminar flow or low Reynolds numbers in the microreactor limits the mixing. Therefore, the mixing needs to be enhanced by, for example, introduction of microstructures, and inert gas.

The short residence time and rapid micromixing in microreactor leads to rapid scavenging of photo-generated charge carriers, reducing the recombination[44]. The continuous flow with effective transport phenomenon in microreactor can prevent the surface recombination and photo-corrosion of the photocatalyst. The OFMR coated with the thin film of nano-structured

158 semiconductor heterojunction is believed to improve the photocatalytic activity by the
159 enhanced charge separation, transport, and utilization with the confined flow dynamics at
160 micro-scale.

161 The photocatlytic reaction physically depends on the photon transport and photoredox
162 reactions. Most of the work has been carried out in the batch reactor. This has the following
163 disadvantages due to which the productivity and selectivity are low [45]: 1) unsteady photon and
164 mass transfer path lengths due to the photocatalyst motion in the reactor 2) inhomogeneous
165 photon absorption by the catalyst due to photocatlyst motion, and 3) difficult to scale up for
166 the energy transformation. The reactant exposure to light can be controlled by the flow rates in
167 OFMR. The precise control on adsorption, desorption, and residence time of reaction medium
168 in OFMR avoids the formation of undesired products. The laminar flow induced diffusive
169 mixing in OFMR is a dominant factor for the photoreaction, passive mixers creates chaotic
170 advection and reduces the mixing time (<1 s) and length[46,47,48]. The micromixers improve the
171 local mass transfer between the fluid stream interfaces and maintain homogeneity in
172 concentration in OFMR[48]. The diffusion effect on the reaction relies on the Damköhler number
173 (Da), a ratio of reaction to mass transfer rate. The chemical conversions are mass transfer
174 controlled when Da > 1, mixed mass transfer and reaction rate limited when Da = 1, and
175 reaction rate controlled when Da < 1. The requirement for the chemical reaction is transport
176 resistance elimination. Enhanced mass transfer within a short time improves the reactivity and
177 selectivity for the chemical transformation[49,50]. The OFMR has major advantages of short
178 photon and mass transfer path lengths[51]. The planar and micropillared OFMRs have been
179 studied for the photocatalytic water splitting. Micropillared OFMR has shown the higher
180 photocatalytic performance than the planar due to the intensive mass transfer by the
181 micropillars. The development of the OFMR with the high surface to volume ratio is required
182 to shorten the diffusion path length and to further improve the mass transfer.

1.3.1 Fabrication of OFMR

OFMRs are usually fabricated using polymeric materials and glass substrates. Among these, using polymeric materials,[52] such as polydimethylsiloxane (PDMS), micro-devices can easily and rapidly be fabricated. However, the limitations of polymer surface chemistry and limited optical transparency restrict their use to narrow applications.[53,54,55] On the other hand, glass has better properties such as optical transparency, thermomechanical resistance and chemical stability which allow it to be used in a large number of optofluidic and microfluidic applications.

Conventional and frontier fabrication methods for microchannel fabrication on glass refer to photolithography followed by wet chemical etching, combination of soft lithography and photolithography, and femtosecond laser micromachining. These methods use time-consuming and complex procedures, they are restriced to clean room, and requires expensive infrastructure.[56-57]

Ongoing efforts to develop inexpensive microchannel facilitated glass systems refer to utilizing free and open source hardware to enhance features associated to microdevice manufacturing platforms at a lower cost (**Table 1.1**).[58,59] Alternatively, Bartholomeusz and co-workers[60] introduced a rapid and inexpensive xurography technique to create a micro-pattern in an adhesive layer with a razor blade. Adhesive tape has also been explored in additive manufacturing[61,62] and pattern transfer[63-64] through a peel-off process. Thereby, adhesives have been amenable to target new micro-nano fabrication applications. In other words, adhesive tape microfabrication is intense, robust in comparison to lithography intricate methods. The advantages of adhesive tape in microfabrication are its adhesive nature, flexibility in employing, and optical transparency[65].

Adhesive based microchannel fabrication was targeted for PDMS systems through a combination of soft lithography and xurography using CO_2 laser[66] or knife plotter.[67] However, the CO_2 laser process left grooves and is not highly promising. Adhesive tape was also used to seal PDMS microfluidic chips directly.[68,69] The utility of adhesive tape for glass microchannel fabrication was targeted by Santana and co-workers[70] by following xurography and adopting the vinyl adhesive layer for peeling off the pattern on glass. The method was not highly effective due to the contribution of adhesive glue layer towards the microchannel irregularities that arise during etching based delamination. Zhang et al. (**Table 1.1**; entry 1)[71] used dry film photoresist (DFR) as a pattern transfer mask in the wet chemical etching process to develop glass microfluidic devices. In this work, they utilized a single step lamination approach to create a DFR mask on the glass which decreases the complexity and cost of fabrication. This method is superior to the conventional masking method, which requires the metal layer and photoresist spin coating.

According to Nagarah et al. (**Table 1.1**; entry 2),[72] utilization of ProTEK PSA (an HF photoresist resistant, HFPR), during wet chemical etching of fused silica, produces patterns with feature size ~600 µm. The substrate made using this masking method requires basic photolithography tools and can create a pit free etched surface with an average roughness of around 10 nm. However, the process resulted in a notable undercut. They claimed the undercut can be controlled when the HFPR is combined with Cr/Au or polySi films, but at the cost of substantial surface pitting and prolonged etch time.

According to Iliescu et al. (**Table 1.1**; entry 3),[73] the composition of the glass is important for the quality of the surface created. In Corning 7740, the only insoluble component present is Al_2O_3, with a concentration approximately 2 wt.%. This explains both the smooth surface created following an extended HF etching period and the minimal change in surface roughness when HCl was added to the etching solution. On the other hand, in the case of soda lime, the

generated surface is significantly impacted by the presence of HCl in the etchant. With 12.9 wt.% of HCl, many of the oxides present in soda lime glass generate insoluble compounds, such as CaO, MgO, and Al_2O_3, in HF.

Tay et al. (**Table 1.1**; entry 4),[74] reported that glass may be wet etched up to 500 µm depth using a Cr/Au mask and photoresist. To achieve deeper channels on glass, the authors suggested that the glass must be annealed, select a glassware with stable etch rate, use a low stress masking layer, and use an adhesion layer of good quality that is free of chromium oxide contamination.

The annealed PECVD amorphous silicon layer was reportedly employed as an etching mask by Iliescu et al. (**Table 1.1**; entry 5).[75] The authors claimed that the maximum etch depth in glass can approach 300 µm, if there are no pinholes on the surface and no notch defects along the edges. The residual stress reduction in the produced amorphous silicon layer is crucial for successful glass etch outcomes. By optimizing the annealing process at 400 °C for different duration, the comprehensive stress can almost be completely eliminated. The freestanding, comprehensive strained amorphous silicon layer at the fractured edges and without annealing can allow for a maximum etch dept of only 100 µm.

On soda-lime glass substrates, Lin et al. (**Table 1.1**; entry 6),[76] reported a quick, inexpensive, but trustworthy approach for the production of microfluidic systems using buffered oxide etching (BOE). For BOE of soda-lime glass, a thin layer of AZ 4620 positive photoresist (PR) was employed as an etch mask rather than an expensive metal or polysilicon/nitride layer. A unique two-step baking procedure extends the PR mask's time in the etchant, preventing major PR peeling issues. The glass substrate was submerged in a 1 M HCl solution to eliminate precipitated particles produced during the etching process. In an ultrasonic bath, a microfluidic

channel with a depth of 35.95±0.39 µm was formed after 40 minutes of BOE. The final channel had a smooth profile and a surface roughness of less than 45.95±7.96 Å.

Coltro et al. (**Table 1.1**; entry 7), used the toner layers as mask transfer onto the glass. The wet chemical etching of the so formed glass substrate in 25% (v/v) HF as etchant at 130ºC temperature resulted in an etch rate of 7.1 µm min^{-1}.[70] The toner-mediated lithographic method effectively uses toner layers as an etching mask to create glass microchannels instantly at low cost. Santana et al. (**Table 1.1**; entry 9)[77] proposes that the vinyl adhesive film masks created using xurography are appropriate for quickly creating glass microchannels through wet chemical etching.

Table 1.1: Glass microchannel depth attained by various fabrication methods.

S.No.	Method	Conditions	Depth (µm)	Etch factor	Reference
1	Dry film photoresist as pattern transfer mask for photolithography followed by etching	Etch time = 5-30 min NH_4F(40%)/HF(49%) = 1/1 to 1/8 Temperature (20-40°C)	102	1.02	[71]
2	Photolithography and etching	%HF = 40 Etch time = 1h	250-300	--	[72]
3	Photolithography and etching	HF(49%)/HCl(37%) = 10:0 to 10:1.5 Etch time = 10 - 40 min	350	--	[73]

4	Cr/Au masking using lithography and etching	%HF = 10-49 Etch time = 15-60 min	Upto 500	--	[78]
5	PECVD followed by lithography and etching	%HF = 49 Etch time = 15 min	300	--	[79]
6	Xurography followed by etching	%HF = 20 Etch time = 4 min	20		[76]
7	Toner mediated lithographic technology	%HF = 25 Etch time = 7 min	35	0.18	[80]
8	Xurography in vinyl adhesive layer followed by etching	%HF = 20 Etch time = 4 min	20	0.1	[70]
9	Xurography of double coated tape followed by etching	Etchant = 1HF: $3HNO_3$:$10H_2O$ Etch time = 17 min	25	0.18	[77]

1.4 Visible light-responsive photocatalysts

1.4.1 Cadmium sulfide (CdS)

Till date, the TiO_2 and Pt/TiO_2 coated planar and micropillar microreactors have been reported for the photocatalytic production of Hydrogen through the water splitting under UV light irradiation [81],[82],[83]. However, the solar spectrum contains less than 4% of UV light. Therefore, complete utilization of the solar spectrum is not possible with UV light active photocatalysts in microreactors specifically. In this regard, the CdS, with a narrow band gap of 2.4 eV, offers a plausible alternative towards the production of hydrogen. The band gap energy and the edge potentials of CdS are appropriate for the water reduction under visible light irradiation [84],[85].

The major issues with CdS are the recombination of photo-excited charge carriers and photo-corrosion. These issues can be curtailed by reducing the charge-carrier path length (using nanoparticles, nanowires, etc. of CdS) and using suitable sacrificial reagent, respectively [86]. The CdS is declared as human carcinogen relative to the lung, kidneys, and bone fracture[87,88]. Cadmium can easily be bioaccumulated by the crops, aquatic life, vegetables and rice foodstuff. Consumption of cadmium contained food is harmful to human health[89]. The biosynthesis of CdS NP from living organisms has been attracted due to its applications in the biomedical and diagnostics[90].

Lu et al. (**Table 1.2**; entry 1),[91] synthesized a series of MoS_2-CdS nanorod (NR) heterostructures by calcination of various MoO_xS_y-CdS NR precursors in the sulfur environment and tested them for photocatalytic hydrogen generation. The maximum H_2 generation (31.5 mmol h^{-1} g^{-1}) was achieved by MoS_2-tipped CdS NRs. This is attributed by the authors to: (i) the crystalline MoS_2 on the tips of CdS NRs, which intensified the photogenerated charges separation; and (ii) redox sites separation.

Pan et al. (**Table 1.2**; entry 2),[92] reported the direct hydrothermal procedure for the modification of CdS nanorods with the nickel-cobalt bimetallic sulphide to enhance the reactive sites. The CdS/Ni–Co–S (~6.56 mmol/g·h) showed a higher HER activity than the bare CdS. The authors claim that the Ni-Co-S bimetallic sulphide altered the CdS nanorods to generate more active sites which enhance the photocatalytic HER performance.

Banerjee et al. synthesised the semiconductor composites of mesoporous carbon(MC)/CdS (**Table 1.2**; entry 3)[82] and reported that the band gap of the semiconducting material (CdS) can be tuned by the addition of mesoporous carbon matrix. The band gap increases rapidly with the increase of the MC content in the CdS-carbon composites and the maximum band gap reported

is 2.48 eV for 40-MC/CdS. The efficient charge separation of MC/CdS promotes the evolution of H_2 under visible light, reducing the recombination seen in pure CdS.

Su et al. (**Table 1.2**; entry 4)[93] reported 38 times greater HER activity (58.1 mmol h^{-1} g^{-1}) activity with porous WS_2/CdS than that of the bare CdS. The n-n type heterojunction in the porous WS_2/CdS is claimed to be the reason for enhanced charge carrier separation and reduced recombination, which in turn enhance the HER activity. The sluggish photo effect created by the porous WS_2 structure helped in lengthening of the light path, which in turn caused the CdS photocatalyst to absorb more amount of light and produce more photocurrent.

Devipriya et al. (**Table 1.2**; entry 5),[94] reported the rationally designed step-scheme 5CdS/MnO_x-$BiVO_4$ photocatalyst for the photocatalytic overall water splitting reaction. Based on the PL and EIS investigations, the creation of a heterostructure between MnOx-BiVO4 and CdS NWs demonstrated and claimed an effective separation and transport of photoinduced charge carriers. With H_2 and O_2 generation rate of 1.01 and 0.51 mmol h^{-1} g^{-1}, respectively, and an apparent quantum yield (AQY) of 11.3% at = 420 nm in the absence of any sacrificial reagent, the 5CdS/MnO_x-$BiVO_4$ photocatalyst is active in the overall water-splitting (OWS) reaction. In the S-scheme system, the CdS NWs and MnO_x-$BiVO_4$ are serving as the H_2 and O_2 generation sites, respectively. The dual co-catalysts Pt and MnO_x on hole- and electron rich facets of $BiVO_4$ support the spatial separation of water oxidation and reduction processes and contributed to the enhanced OWS performance.

According to Tian et al.[95] (**Table 1.2**; entry 7) vanadium diboride (VB_2), a highly efficient cocatalyst, can be added to CdS to significantly improve its H_2 evolution activity under the visible light (420 nm). The HER (12.1 mmol h^{-1} g^{-1}) was 11 times higher with VB_2/CdS than that of the bare CdS. The authors claimed that the higher apparent quantum yield (AQE) (4.4%) and higher H_2 generation are obtained due to the increased charge separation by VB_2 cocatalyst.

Table 1.2: Comparison of the hydrogen production rates in this study using serpentine OFMR with those obtained using batch reactors in the literature.

S.No.	Photocatalyst	Catalyst amount mg	H_2 production mmol g^{-1} h^{-1}	Irradiation area cm^2	Reference
1	MoS_2-CdS nanorod	10	31.5	--	[91]
2	CdS/Ni–Co–S	50	37.6	--	[92]
3	Mesoporous carbon/CdS	20	10.6	--	[96]
4	Porous WS_2/CdS	3	58.1	13.4	[93]
5	5CdS/MnO_x-$BiVO_4$	10	1.01	104	[94]
6	CdS	10	~1.75	--	[97]
7	VB_2/CdS	40	12.1	--	[95]
8	CdS	5	5.82	1.95	[98]
9	1%Pt/CdS	100	29.1	9.8	[99]
10	Cd/CdS	2	0.59	0.27	[100]

1.4.2 Graphitic carbon nitride (g-C_3N_4)

The graphitic carbon nitride (g-C_3N_4)[101,102,103,104] (E_g = 2.7 eV) is an earth abundant polymeric semiconductor reported for photocatalytic hydrogen generation. The g-C_3N_4 is active in visible

light owing to its appropriate optronic, stable chemical and thermal properties and band gap energy for visible light H_2 production[102].

Researchers have attempted to modify the band gap and charge transfer path of g-C_3N_4 through morphological control, doping of foreign element, and heterojunction fabrication in order to boost the solar to hydrogen Different structures of g-C_3N_4 can be produced using various material synthesis techniques[105,106,107]. The noble metal nanoparticles that are typically deposited to alter surface are Ag, Pt, Pd, and Au, to name a few[108,109,110]. Heterogeneous structures can be produced by mixing g-C_3N_4 with metal oxides, other inorganic compounds, co-catalysts, and carbon-based materials[111,112,113].

In contrast to surface doping, which only provide a few local states, the uniformly distributed nitrogen vacancies in the g-C_3N_4 organic network are able to tailor the band edge of the absorption to 850 nm.[114] Inorganic semiconductors can only have atomic replacement or gap defects. While the simultaneous atomic and molecular substitution can be achieved with the organic semiconductors. In contrast to inorganic semiconductors, different chemical and ionic substances, including acids and bases, are used as dopants in organic semiconductors[115]. The dopants dispersion may have a negative impact on photocatalyst performance depending on the concentration of dopant.[113] **Error! Reference source not found.** represents the different types of g-C_3N_4 based photocatalysts utilized for the water splitting.

Table 1.3: g-C_3N_4 based photocatalysts for photocatalytic water splitting.

S.No.	**Catalyst**	**Catalyst amount, mg**	**H_2 production mmol g^{-1} h^{-1}**	**Irradiation area cm^2**	**Reference**
1	g-C_3N_4	10	1.2	104	[116]

2	2D/2DMo2C/ g-C_3N_4	20	0.652	--	[117]
3	g-C_3N_4	10	0.108	--	[118]
4	g-C_3N_4	0.1	0.01	--	[119]
5	Bulk g-C_3N_4	10	0.335	--	[120]
6	g-C_3N_4	50	8.8	--	[121]
7	Bulk g-C_3N_4	20	0.28	--	[122]
8	CN/0.05MoP	10	3.5	--	[123]
9	g-C_3N_4-NS/TO-NW	50	5.1	--	[124]
10	g-C_3N_4-Pt	5	9.6	--	[100]

1.4.3 g-C_3N_4/CdS Heterojunction

The demerits of CdS and g-C_3N_4 photocatalysts are fast recombination of charges and nominal surface area. The CdS undergoes photocorrosion upon photo-illumination. Constructing heterojunction between CdS and g-C_3N_4 semiconductors and doping of metals as cocatalysts accelerate the photo excited charge carrier transfer and separation, enhancing the photo driven processes[24,125,126,25,127,128,25]. Designing heterojunctions in photocatalysts has been a practical and effective technique for the spatial separation of electron-hole pairs.

Numerous studies have been reported on the assembling of CN and CdS to enhance the photocatalytic activity for the hydrogen production in batch photocatalytic reactors[129,130,126,131]. In-situ strong coupling of the CN and CdS photocatalysts facilitates the higher redox sites and reduces the recombination via interfacial excitons migration[132,133,134]. The reduction of band gap energy enables broader light absorption by the photocatalyst. The heterojunctions between

g-C_3N_4 and CdS efficiently boost the absorption of visible light for g-C_3N_4, decrease the photo-corrosion for CdS, and promote the charge separation[135] due to their well-aligned band energies. Despite extensive studies on CdS quantum dots/bulk g-C_3N_4 and CdS nanorods/graphene nanosheet hybrid photocatalysts[136,137], there are currently a very few reports on the in situ[115] development of CdS nanorods on g-C_3N_4 nanosheets in aqueous solutions[119,138]. To boost the photocatalytic H_2 production, it is therefore intriguing to establish in situ growth of CdS nanorods on g-C_3N_4 nanosheets with near interface contacts, which is considered as one of the most effective techniques for developing enhanced photocatalysts[139,140]. The CdS nano-structure[34,141] on g-C_3N_4 nanosheet heterojunction[142,143,134] would facilitate the spatial separation of photo-generated charge carriers effectively, and provide more photocatalytic active surface and light harvesting area. **Error! Reference source not found.** represents the summary of different types of g-C_3N_4 based heterojunctions for photocatalytic water splitting.

Table 1.4: Various types of g-C_3N_4 based heterojunction composites for photocatalytic water splitting.

S.No.	Catalyst	Catalyst amount, mg	H_2 production mmol g^{-1} h^{-1}	Irradiation area cm^2	Reference
1	g-C_3N_4–CdS–9% NiS	2	2.56	--	[135]
2	A-GCN 5	10	3.09	--	[144]
3	CdS/Cu7S4-0.33/g-C_3N_4	50	3.5	--	[145]
4	CdS/0.7g-C_3N_4	5	15.3	--	[146]

5	CdS/PdAg/g-C_3N_4	50	3.09	--	[142]
6	g-C_3N_4/CdS	25	3.37	--	[129]
7	$Ni(OH)_2$–CdS/g-C_3N_4	1	12.6	--	[134]
8	P-8Cd2CN	50	7.6	--	[143]
9	Pt-CdS/CNNS	60	38	--	[147]
10	NiCoP-g-C_3N_4/CdS	20	55.63	--	[148]

375

376 The planar OFMR fabrication and its testing for the photocatalytic water splitting over Pt/TiO_2
377 in the presence of redox mediator (I^-/IO_3^-) under the UV irradiation is reported by Ahsan et
378 al.,[149] (**Table 1.5**; entry 1). The authors demonstrated a 2-fold increase in reaction rate with the
379 increase of flow rate from 25 to 400 µL min^{-1} and attributed the enhancement in the rate to the
380 improved mass transfer in microfluidic platform. Li et al.,[82] (**Table 1.5**; entry 2&3) reported a
381 comparison of the rate of water splitting reaction over Pt/TiO_2 photocatalyst coated on planar
382 and micro-pillared OFMRs, which are fabricated using the photolithography method. The
383 micro-pillared OFMR showed the higher performance than the planar OFMR. The authors
384 ascribed the higher rate with micro-pillared OFMR to an increased surface-to-volume ratio
385 which in turn enhances the mass transfer.

386 Chen et al.[83] (**Table 1.5**; entry 4&5) used the replica molding and photolithography approach
387 to fabricate the PDMS micro-grooved OFMR and casting-transfer procedure for the
388 photocatalyst (Pt/TiO_2) coating and tested them for the photocatalytic (PC) water splitting. The
389 authors claimed that the coating method shows higher durability than the conventional methods

such as dip coating and spray coating. Moreover, they demonstrated that the micro-grooved OFMR shows higher water splitting rate due to enhanced mass transfer and higher reaction area than the conventional planar OFMR.

Yosuke et al.[15] (**Table 1.5**; entry 6) used multiple arrays of large scale panel type reactors with photocatalyst RhCrOx/$SrTiO_3$:Al coating for the PC water splitting under the natural sunlight with 1 mm thin water layer on the panel. The H_2 and O_2 bubbles (produced at a high rate of 5.6 mL cm^{-2} h^{-1}) are separated from the panel using acrylic hydrophilic window. However, after 6 h, the activity reduces to 60% of the original due to back reactions.

Xiong et al.[150] (**Table 1.5**; entry 7), have developed a panel (5 cm x 5 cm) by drop-casting the mixed $Rh_{2y}Cr_yO_3/(Ga_{1x}Zn_x)(N_{1x}O_x)$ photocatalyst powder with SiO_2 between two frosted glass plates. They studied the effect of the hydrophilic SiO_2 particle size in the catalyst film on the photocatalytic activity. They revealed the addition of SiO_2 microparticles proved to be an effective method for creating photocatalyst panels. The porosity of the photocatalyst layer facilitates the transfer of water and the release of the evolved gases.

Schröder et al. (**Table 1.5**; entry 8)[151] fabricated a large-scale stainless steel photoreactor with drop-casted (Nafion as binder) mesoporous carbon nitride as photocatalyst for the water splitting under the illumination of sunlight. An average hydrogen production rate of 0.22 L kWh^{-1}. The maximum solar-to-hydrogen (STH) conversion was 0.12% by correlating the sunlight intensity and hydrogen.

From our group, Pala and Peela (**Table 1.5**; entry 9),[152] developed an optofluidic planar microreactor for photocatalytic water splitting with methanol acting as a sacrificial agent while being illuminated by both solar simulator (a 300 W xenon lamp with an AM1.5G filter) and a 400 W metal halide lamp with UV filter. The rate of hydrogen synthesis rose linearly with increasing solar light intensity and catalyst coating thickness and it reached a maximum with

414 increasing reactant flow rate. Under the visible light irradiation, the Pt/TiO_2 film with a
415 thickness of 1650 ± 119 nm produced hydrogen at a rate of 16.35 mmol h^{-1} g^{-1} (4.7 μmol h^{-1} cm^{-2}) at an optimal reactant flow rate of 0.3 mL min^{-1} using 20 vol % methanol in DI water.
416
417 The recycle stability test demonstrated a good adherence of the photocatalyst film, which is
418 necessary for the scale-up of a planar microreactor. At an intensity of about 100 mW cm^{-2}, a
419 solar simulated light driven hydrogen generation rate of 0.766 mmol h^{-1} g^{-1} (0.22 μmol h^{-1} cm^{-2}) with an STH of 0.015% was achieved.
420

421 **Table 1.5:** The hydrogen production performance of optofluidic devices reported in
422 literature.

S.No.	Microreactor	Catalyst	Light source	H_2 production rate, mol h^{-1}	Irradiation area, cm^2	Reference
1	Planar[#]	Pt/TiO_2	UV	1.8×10^{-10}	--	[149]
2	Micropillared[#]	Pt/TiO_2	UV	1.8×10^{-8}	--	[82]
3	Planar[#]	Pt/TiO_2	UV	1.2×10^{-8}	--	[82]
4	Grooved[#]	Pt/TiO_2	UV	3.72×10^{-9}	--	[83]
5	Flat[#]	Pt/TiO_2	UV	1.42×10^{-9}	--	[83]
6	Panels[†]	$SrTiO_3$:Al with co-catalyst, RhCrOx (Rh 0.1wt%, Cr 0.1wt%)	300 W Xe lamp	680×10^{-6}	25	[15]

7	Panels	$Rh_{2-y}Cr_yO_3/(Ga_{1-x}Zn_x)(N_{1-x}O_x)$	300 W Xe lamp	117×10^{-6}	25	[150]
8	Planar large scale	Pt@mp-CN	Sunlight	7420×10^{-6}	7560	[151]
9	Planar	Pt/TiO_2	Visible light	35.25	7.5	[152]

Notes: [#]In these studies, the iodide depletion is used as a measure of hydrogen production rate. [†]Reduced gas pressure (10 kPa) is used to remove the produced hydrogen quickly.

1.5 Knowledge gap and hypothesis

As observed from the literature review, a significant number of studies are published on photocatalytic hydrogen generation using batch photo-reactors. The batch reactors have limitations in terms of light absorption, transport properties, higher light scattering, and scale up. The OFMRs mitigate some of these challenges. However, the OFMRs themselves pose some challenges (knowledge gaps) which are summarized here. The expensive fabrication methods are required to make microchannels in glass. Both conventional and cutting-edge manufacturing techniques are reported to fabricate microchannels in glass, including photolithography, wet chemical etching, a combination of soft lithography and photolithography, etc. These methods are limited to clean rooms, require expensive infrastructure, and involve sophisticated procedures. Therefore, a cheaper, simpler and reliable fabrication method is highly warranted. In-situ synthesis of heterojunction photocatalysts, with the adherent and uniform photocatalyst coating, favours efficient charge separation, light absorption, and faster scaling up of the OFMRs. However, this synthesis method is underdeveloped as per the literature reports. A study of hydrodynamics is needed to

comprehend how fluid flows over an immobilised photocatalyst and how fluid transport characteristics affect photocatalytic reactions.

1.6 Objectives of the work

The overall objective of this Ph.D. thesis is to develop cheaper, simpler and more reliable method for the fabrication of OFMRs with various geometries (planar, pillared, serpentine and corrugated serpentine) and to test them, after (in situ) coating them with suitable photocatalyst, for the green hydrogen production from solar energy through water-splitting reaction.

The overall objective is divided into the sub-objectives as follows:

- To fabricate OFMRs of various geometries (planar, pillared, serpentine and corrugated serpentine).
- To synthesize and characterize CdS and (in situ) CdS/g-C_3N_4 photocatalysts.
- To study the production of green hydrogen in multiphase serpentine OFMR.
- To correlate the microchannel geometry effects with the hydrogen production rates, flow visualization studies.
- To test the OFMR, coated with various photocatalysts, for the photocatalytic water splitting to produce green hydrogen, under various reaction conditions.

1.7 Organisation of the thesis

The thesis is organized into five chapters.

Chapter 1: Background of the work and objectives

This chapter introduces about the research area, gives an overeview of literature, knowledge gaps, objectives and organisation of the thesis.

Chapter 2: Materials and methodology

This chapter discusses the materials and methods used to synthesize photocatalysts, fabricate OFMRs and produce green hydrogen. This also includes the methodologies for the H_2 analysis and for the characterization of OFMRs and photocatalysts.

Chapter 3: Adhesive tape based fabrication of optofluidic glass microreactor

The objective of this chapter was to develop an effective, simple, rapid, and inexpensive glass microchannel fabrication method using adhesive tape as a mask. The effect of associated parameters, such as etchant concentration, etching time, and microchannel geometry, on the final depth and etch factor was studied in detail. The microchannels with various shapes (such as Wavy, Y-shape, T-shape) were fabricated with adhesive tape as a mask, to prove the robustness of the method developed.

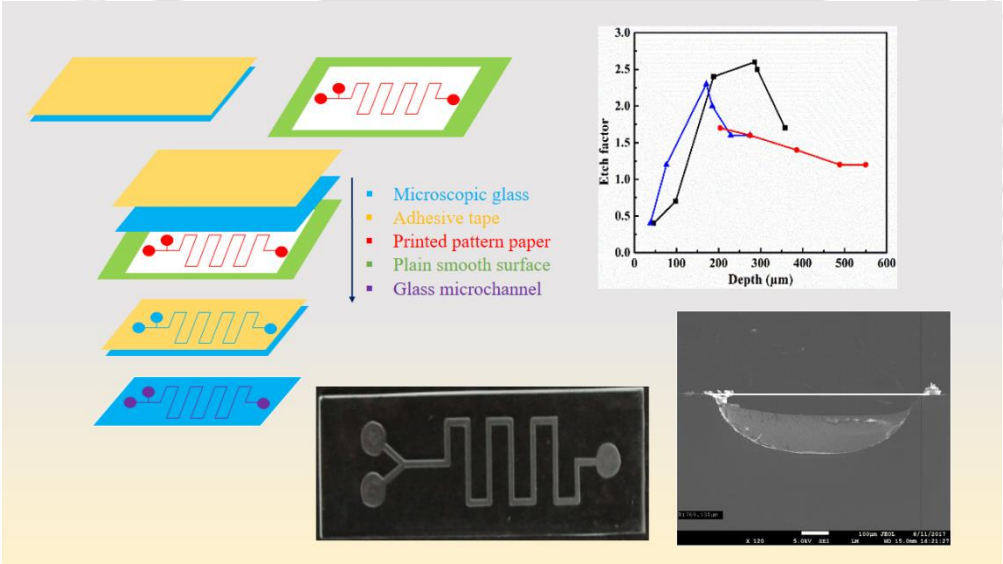

Chapter 4: Optofluidic microreactor for the photocatalytic water splitting to produce green hydrogen

This chapter explains the sol-gel method used for the CdS catalyst coating in the microreactors. The effect of liquid flow rate, geometry of microchannel and sacrificial reagent (Na_2SO_3/Na_2S) concentration on the hydrogen generation under visible light irradiation was studied in detail. A higher H_2 production rate was observed in the serpentine microreactor as compared to that

in planar and micropillared microreactors. The serpentine microreactor, having higher surface-to-volume ratio, induced the micromixing that enhanced the mass transfer of the sacrificial reagent and resulted in higher H_2 formation. Further, the multiphase photocatalytic hydrogen generation over the CdS photocatalyst in the presence of 0.1 M Na_2SO_3/Na_2S under UV light irradiation and a N_2 flow rate of 0.5 – 1 mL min^{-1} was studied in serpentine OFMR. A higher H_2 production rate (0.298 µmol h^{-1}) was observed at the gas and liquid flow rates of 1 and 0.8 mL min^{-1}, respectively. With increase of inert gas flow rate, the hydrogen evolution rate was increased at lower flow rates and the decreased reaching maximum at a flow rate of 0.8 mL min^{-1}. The increase of H_2 production rate at lower flow rates can be due to the enhanced mixing and mass transfer, while its decrease at higher flow rates was due to the gas phase occupying more photocatalyst active area.

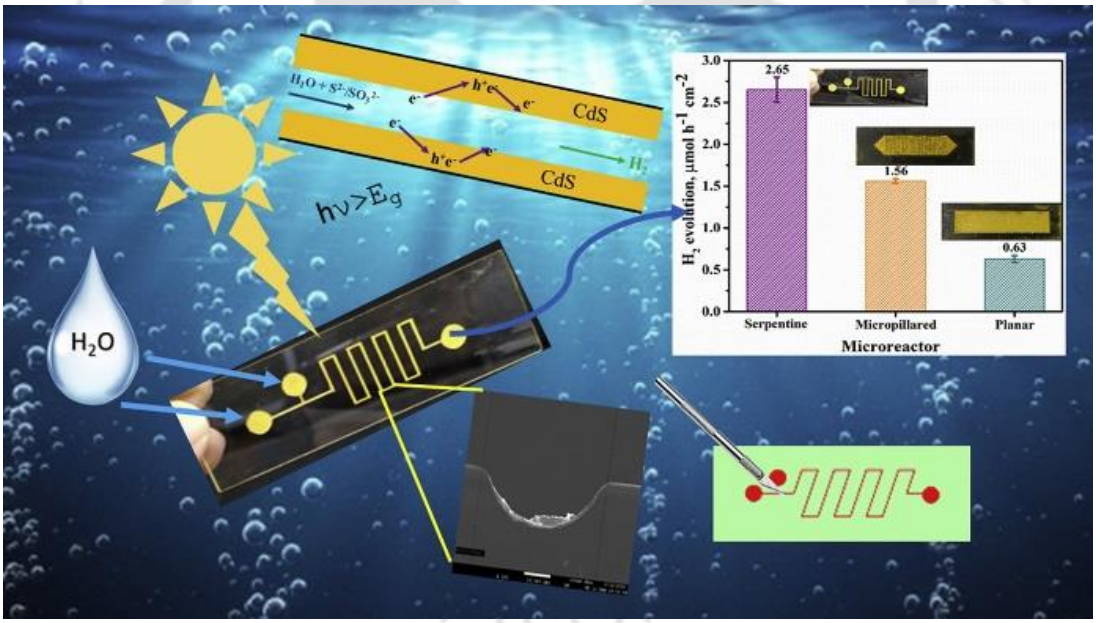

Chapter 5: In-situ synthesis of CdS nanostructures on g-C_3N_4 nanosheets in novel 3D optofluidic microreactor for enhanced photocatalytic hydrogen production

This chapter discusses a simple and cost-effective fabrication method to develop an effective corrugated serpentine OFMR (C-SOFMR) with advanced features, such as expansion/contraction and wavy microstructure. A laminar flow with no back mixing was observed in plain serpentine OFMR (P-SOFMR). While, stretching and folding of fluid along

with back mixing was observed in C-SOFMR. Further, the CdS nanowires on g-C_3N_4 nanosheet (CN/CdS) heterojunction was synthesized *in situ* both P-SOFMR and C-SOFMR and utilized the device for the photocatalytic green hydrogen generation. The CN/CdS heterojunction endowed with narrow band gap energy (2.01 eV). The longer CdS nanowires (~110 nm) benefit the electronic interface with CN in the CN/CdS heterojunction and lead to the spatial separation (reduced recombination) of excitons along the CdS axial direction. The charges generated were utilized efficiently for the HER reaction in both P-SOFMR and C-SOFMR at higher flow rates attributing to the rapid micro-mixing and mass transfer. The CN/CdS heterojunction showed the highest photocatalytic activity (6.38 µmol h^{-1} in C-SOFMR and 6.16 µmol h^{-1} in P-SOFMR at 1.0 mL min^{-1}) due to its good optronic properties.

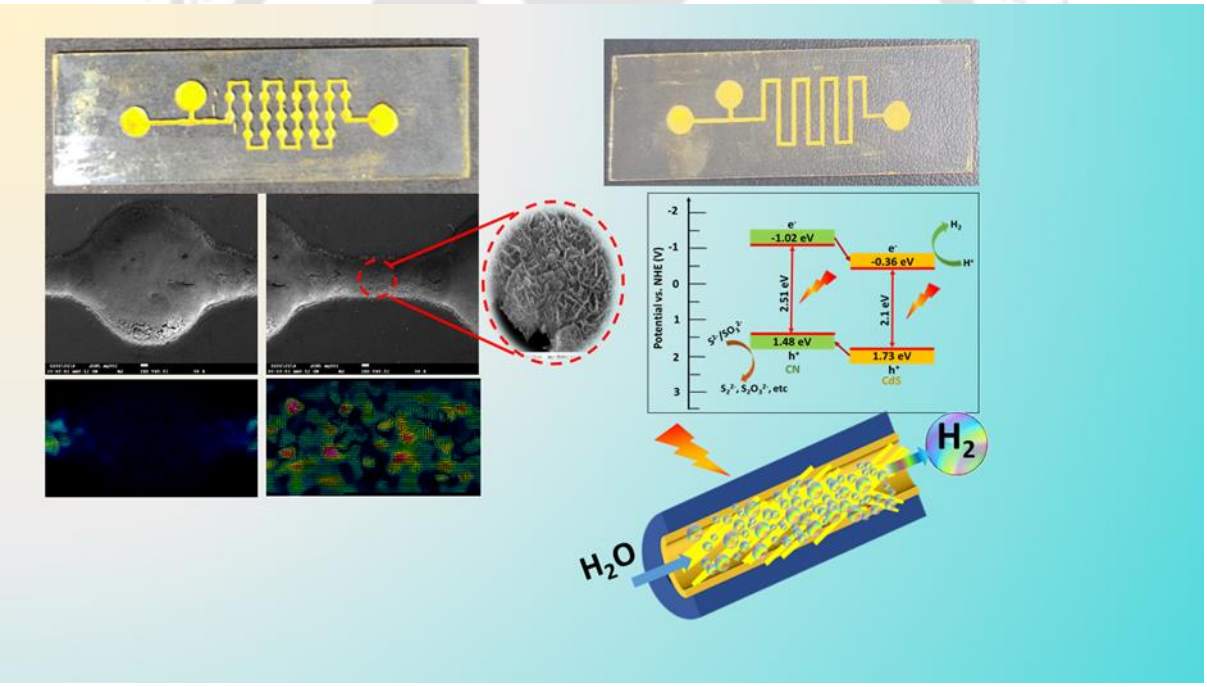

Chapter 6: Thesis conclusions and future work

This chapter provides the conclusions and future work of the photocatalytic hydrogen generation through water splitting reaction in OFMRs.

510

Chapter 2

Materials and Methodology

2.1 Materials and reagents

The list of the materials and reagents used in this study and their origin are given in Table 2.1. The chemicals are used as received without any further purification.

Table 2.1: The materials and reagents used in this study and their origin.

S.No.	Materials name	Purity (%)	Make
1	Microscopic glass (76.2 mm x 25.4 mm, thickness of 1 mm)	--	JSGW, India
2	Plain smooth surface	--	Locally available
3	Photoresist	--	Microposit S1813, USA
4	Developer	--	Shipley, USA
5	Hydrofluoric acid	48	Himedia, India
6	DI water from the Millipore unit	--	Model: Elix-3, Make: Millipore, USA
7	Adhesive tape	--	Cello, India
8	Magnifying glasses (10x)	--	Locally available
9	Surgical knife	--	Locally available
10	Iron slab with smooth edge	--	Locally available

11	Polyethylene glycol 4000 (PEG)	--	Merck, India
12	Acetic acid	99.6	Himedia, India
13	Cadmium nitrate tetrahydrade	99	Sigma Aldrich, India
14	Thiourea	99	Sigma Aldrich,India
15	Ethanol	99	Merck, India
16	Sodium sulfide	99	Sigma Aldrich, India
17	Sodium sulfite	99	Sigma Aldrich, India
18	Triethanolamine	-	Merck, India
19	Lactic acid	-	Merck, India

2.2 Methods

2.2.1 Adhesive tape based fabrication

The schematic describing the microchannel fabrication using adhesive tape as a mask is shown in **Figure 2.1**. Firstly, the patterned paper was pasted on the surface of a plain smooth surface using adhesive gum. Transparent adhesive tape was pasted on the microscopic glass and the sample was aligned with the pattern. Thereafter, using a magnifying glass (10x) and a surgical knife, the desired microchannel pattern was developed on the adhesive tape. Eventually, the patterned surface was cleaned with ethanol to minimize adhesive gum effect on microchannel geometry. Adhesive tape was also pasted to the opposite side of the patterned microscopic glass and then subjected to etching. After etching, the adhesive tape was removed and the sample was rinsed with water, thoroughly cleaned with piranha solution and rinsed with water again.

During wet etching process, the etchant concentration and the etching time were varied in the range of 5 to 49 wt.% of HF in DI water and 15 to 120 min, respectively.

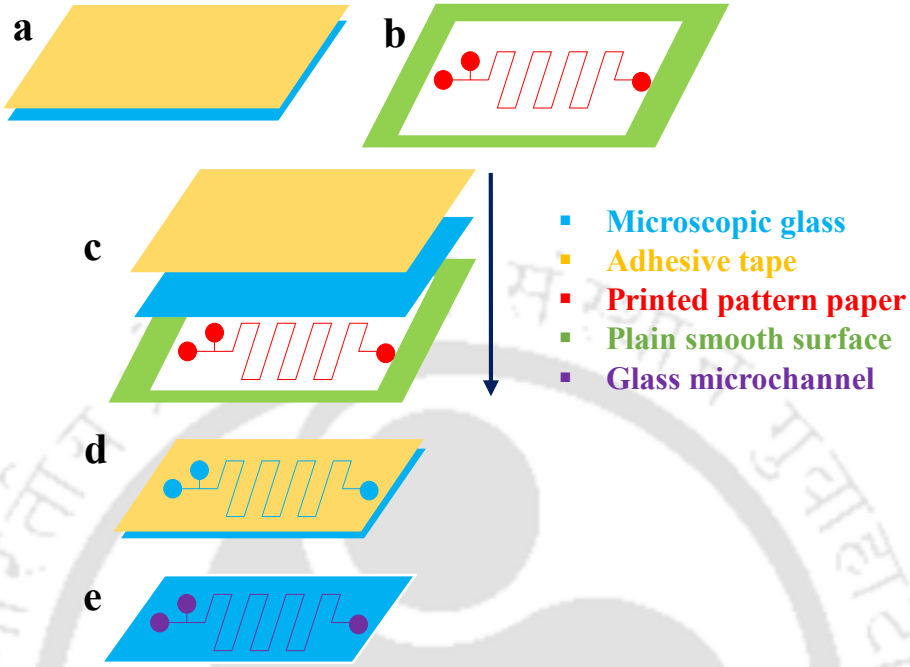

Figure 2.1: Schematic of adhesive tape based microchannel fabrication on glass: (a) applied adhesive tape microscopic glass. (b) Printed pattern paper pasted on plain glass surface. (c) Aligning (a) on (b). (d) Pattern developed by cutting and removing of the adhesive tape. (e) Glass microchannel after wet chemical etching.

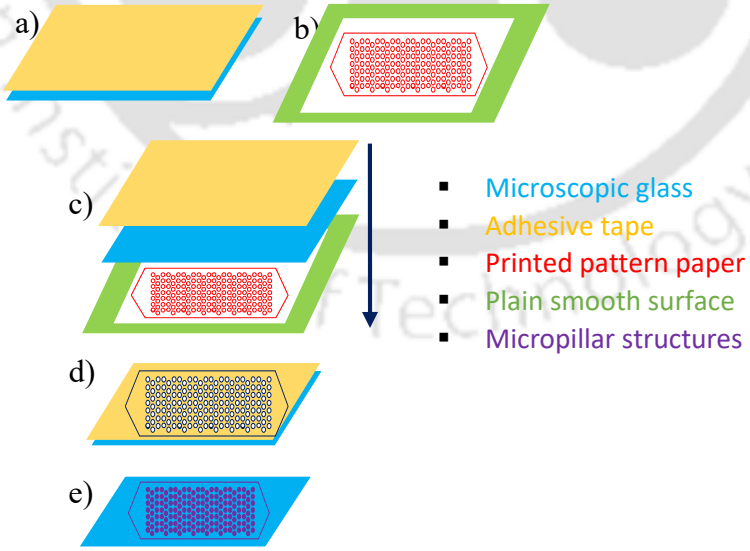

Figure 2.2: Schematic of adhesive tape based microchannel fabrication on glass: (a) applied adhesive tape microscopic glass. (b) Printed pattern paper pasted on plain glass surface. (c) Aligning (a) on (b). (d) Pattern developed by cutting and removing of the adhesive tape. (e) Micropillars after wet chemical etching.

serpentinemicrochannel with desired dimensions was achieved after etching. Micropillared and planar microreacors also fabricated using same method (**Figure 2.2**).

2.2.2 Photolithography based fabrication

In photolithography (**Figure 2.3**), a positive photoresist (S1813 Microposit) was first spin coated onto the microscopic glass at 3000 rpm for 10 s followed by baking at 140°C for 2 min (pre-baking). The microchannel pattern was drawn in KLayout software, exported to mask writer (Model: Dilase 250; Make: Kloe, France) and transferred onto the mask by laser writing. Photolithography writing was carriedout on the mask using 365 nm laser wavelength, 80% modulation, 1 µm spot size and 1 mm/s writing speed. The patterned substrate was then placed in the developer solution for 1 min to remove the part of photoresist that was exposed to laser. Finally, the substrate was baked at 175°C for 2 h (post-baking) and an adhesive tape was applied to the opposite side of the patterned surface. The sample was then subjected to wet etching, following a similar procedure as that presented for the adhesive tape based fabrication.

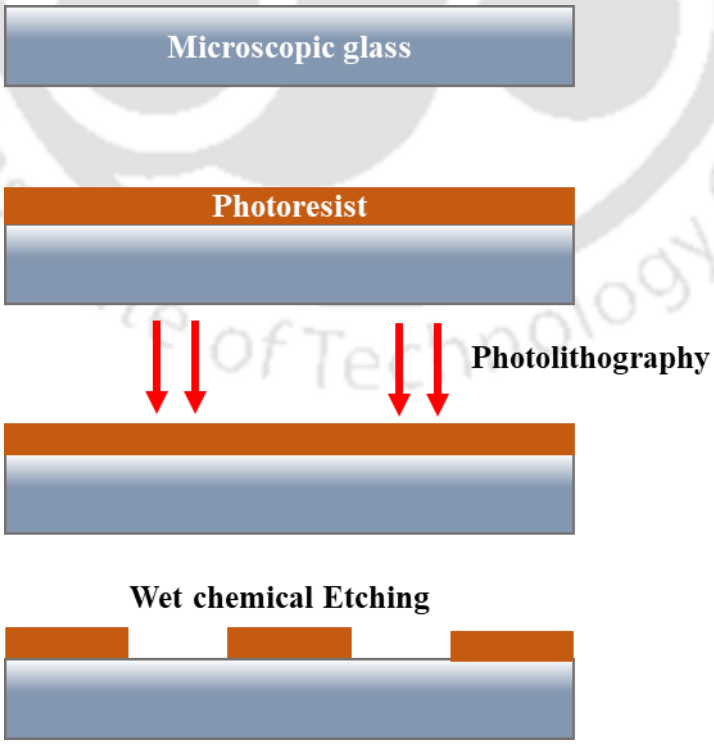

Figure 2.3: Photolithography method for glass fabrication.

2.2.3 Fabrication of corrugated serpentine OFMR (C-SOFMR)

The P-SOFMR was fabricated using a simple and low cost adhesive tape based glass fabrication method as reported previously.[44] The C-SOFMR fabrication involved the following steps: Firstly aligned the adhesive tape applied microscopic glass with a printed pattern design (**Figure 2.4a**) and the micropattern was generated by manual cutting and removal of the

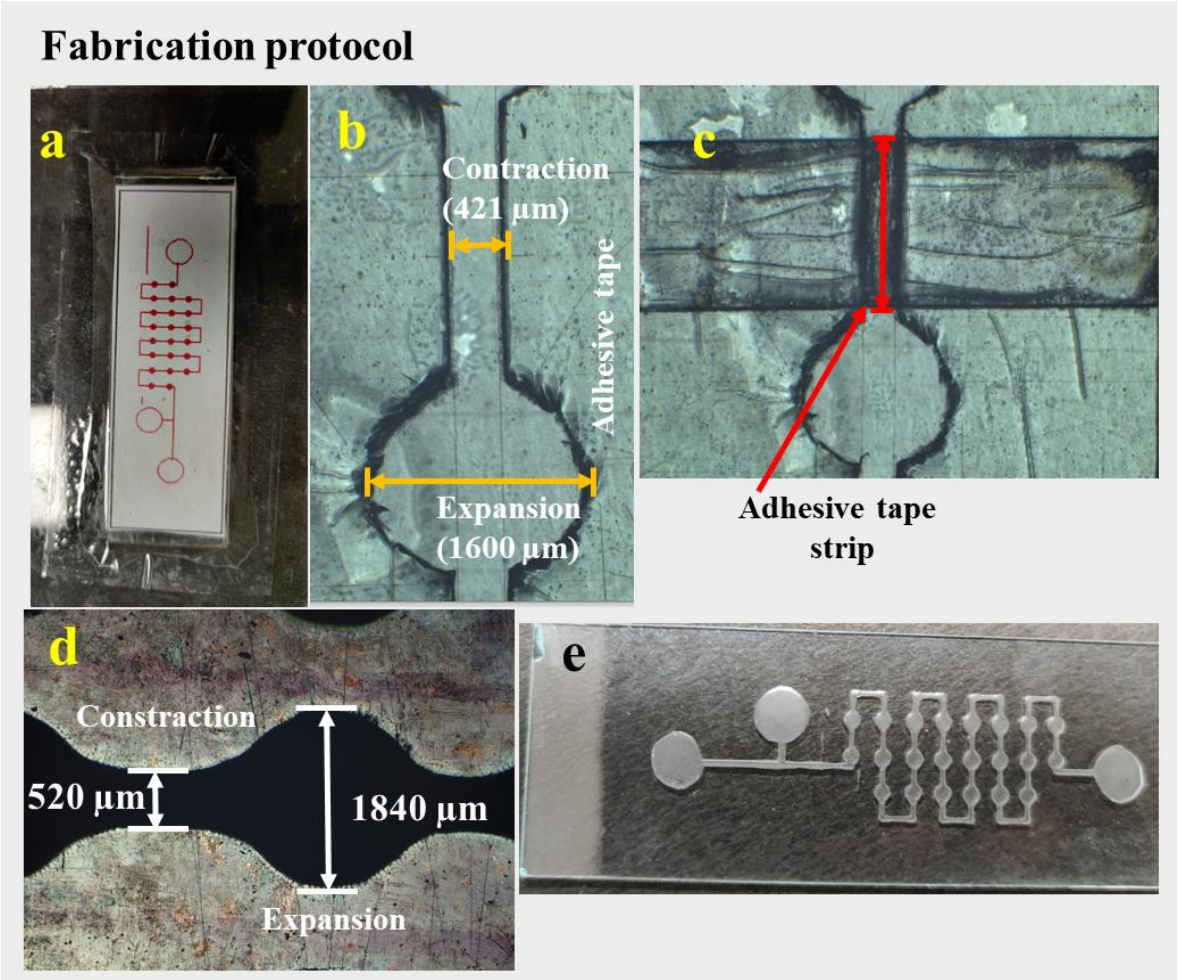

Figure 2.4: Fabrication of expansion and contraction with wavy microstructure in OFMR. (a) Alignment of microscopic glass having applied adhesive tape with the printed pattern. Optical microscope image of (b) the pattern with adhesive tape as mask (c) adhesive strip pasted at the contraction part. (d) The FESEM image of microchannel after etching (Scale: 500 µm) and (e) Optical camera image of microstructured microchannel.

unwanted adhesive tape using surgical knife and 10x magnifying lens (**Figure 2.4b**). Then, the 1700 µm of adhesive strip was glued at the contraction part (**Figure 2.4c**) to prevent etchant contact with the contraction part. The adhesive tape was also applied to the glass on the

opposite side of the pattern. The masked glass substrate was then etched for 15 min to achieve the expansion with trough microstructure in the microchannel. After this, the adhesive tape strip from the contraction part was removed and etched the glass substrate for another 15 min to attain the contraction with crest microstructure. The two different etching times helped to produce a wavy microstructure throughout the microchannel. After etching, the substrate (**Figure 2.4d** and **e**) was subjected to cleaning with piranha solution.

2.3 In-situ synthesis of CdS naospikes and nanoleaf structure in microchannel

The steps involved in the synthesis of in-situ CdS nanostructure: The equimolar (0.01 M) amounts of the cadmium nitrate and thiourea were taken in a beaker and kept on stirring for 1 h (solution 1). The equimolar (0.025M) amounts of the cadmium nitrate and hexamethylenetetramine (HMTA) were taken in another beaker and kept under stirring for 1 h (solution 2). The solution 1 is coated in the microchannel and calcined at 350˚C for 15 min. With the help of syringe pump, solution 2 was injected at a flow rate of 1 mL $min^{-1}$to the OFMR kept at 80˚C followed by heating at 160˚C for 6 h, thus the CdS nanospikes were formed in the microchannel. To achieve the CdS nanoleaf structure, the induced CdS nanospikes in the microchannel were calcined at 350˚C for 1 h.

2.4 CdS photocatalyst synthesis and coating

The following steps have been meticulously followed to achieve the synthesis of the photocatalyst using the sol-gel method. Firstly, the solution 1 was prepared through the mixing of 1.5 g of PEG, 0.5 mL of acetic acid, and 3 mL of ethanol. Simultaneously, the solution 2 was prepared through the dissolution of 2.3642 g of $Cd(NO)_3$ and 0.7612 g of thiourea in 6 mL of ethanol. After stirring for 1 h, the individual solutions 1and 2 were mixed with each other and were kept under vigorous stirring for 4 h. Thereafter, the mixture was aged for 48 h to

transform into a gel that facilitates the effective adherence of the CdS film. The sol was coated on to the optofluidic reactor plates using a spin coater (SpinNXG, India) at 2000 rpm for 30 s. The coated optofluidic plate was calcined at 350°C for 1 h in a muffle furnace. Subsequently, the excess deposits of photocatalyst at places other than channel were removed by scraping with doctor's blade followed by cleaning with ethanol. The steps from spin coating through ethanol cleaning were repeated for four cycles to achieve the desired thickness of the photocatalyst.

2.5 CN/CdS Heterojunction synthesis

2.5.1 g-C_3N_4 (CN) synthesis

The CN was prepared by simple thermal treatment according to our previous work[116]. Briefly, 1.5 g of thiourea was taken in a crucible and calcined at 550°C for 2 h in muffle furnace. The pale yellow coloured CN obtained after calcination was grinded with the help of mortar and pestle.

2.5.2 CdS nanowires on g-C_3N_4 nanosheet (CN/CdS) synthesis

The procedure for the synthesis of CdS nanowires was as following[44]: 1.5 g of polyethylene glycol (PEG) was added to 4 mL of ethanol (solution 1) and stirred for 1 h. The required amounts of cadmium nitrate tetrahydrate and thiourea were added to 6 mL of ethanol (solution 2) and stirred for 1 h. The solution 1 was added slowly to solution 2 under stirring and then the desired amount of g-C_3N_4 was added and stirred for 4 h. The final solution was kept in a black box for aging (24 h). The coating of the synthesized photocatalyst onto the inner surface of the OFMR was carried out using a spin coater operated at 2000 rpm. Then, the coated OFMR was thermally treated at 350°C for 1 h. During the thermal treatment, the CdS nanowires grow to the required size, which is termed as *in situ* growth. The schematic of the coating procedure is shown in **Figure 2.5**. The composition of the sol-gel to make thin films on the OFMR was

varied by varying the CN loading in CdS. The photocatalysts with CN loading 0.009, 0.17, 0.44, 4.46, and 89.28 wt% were named as CN/CdSx, where x is 1, 2, 3, 4, and 5, respectively. The spin coating was repeated for five times to achieve the required thickness of the film and then used for the characterization and the photocatalytic activity tests.

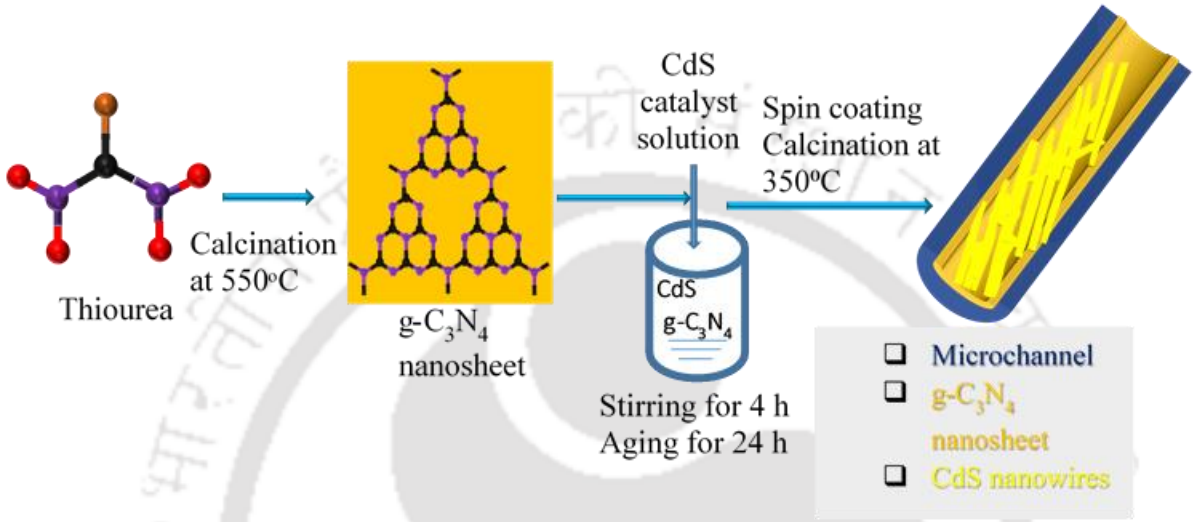

Figure 2.5: In-situ CN/CdS heterojunction synthesis in integrated optofluidic microreactor.

2.6 Characterization techniques

Physicochemical properties of microchannels, synthesized materials, and photo catalytic activity are characterized using various technical instruments (**Table 2.2**).

2.6.1 Powder X-ray diffraction (PXRD)

The powder X-ray diffraction (PXRD) analysis was performed to find out the crystallinity and the crystal phase of the photocatalysts, using diffractometer (Model: SmartLab; Make: Rigaku, Japan) with Cu Kα radiation (λ = 0.15406 nm). An amount of 20 mg dried sample was placed into the holder and the XRD patterns were recorded between 5 and 70° of 2θ angle with a step size of 0.02° and a scan speed of 20°/min.

The Crystallite size of the synthesized photocatalysts was calculated using the Scharrer equation

$$t = \frac{0.9\lambda}{\beta cos\theta}$$

Where λ, θ, β are the X-ray wavelength, Bragg's angle, and full width at half maximum.

2.6.2 UV–Vis spectrometer

The light absorption data that is obtained from UV–Vis spectrometer (Model: UV-2600, Make: Shimadzu, Japan) was used to calculate the band gap energies of synthesized photocatalysts, such as CdS, CN, and CN/CdS. The bare barium sulphate was taken as a reference and photocatalyst sample was uniformly spread over the barium sulphate pellet, then allowed to UV-visible spectra characterization.

The optical band gap energy was calculated using the Kubelka-Munk equation

$$\alpha h\nu = A(h\nu - E_g)^n$$

Where α, hν, A, and E_g are the absorption coefficient, the energy of an incident photon, and the proportionality constant. The n is 2 for indirect band gap and ½ for direct band gap of the photocatalyst (n = 2 for CdS and CN/CdS).

2.6.3 Optical microscope

An optical microscope (Model: DM2500 M; Make: Leica, Germany) was used to measure the dimensions of the patterned microchannel on adhesive tape.

2.6.4 Field emission transmission electron microscopy (FETEM)

The size and surface morphology of synthesized photocatalysts such as CN/CdS were obtained using field emission transmission electron microscopy (FETEM, Model: JEM 2100; Make: JEOL, Japan). A quantity of 1 mg specimen particles was dispersed in 10 mL ethanol and the suspension was then placed in the ultrasonic bath for 30 min to disperse particles. One drop of suspension was deposited onto the carbon-coated copper grid. The grid was allowed to vaccum dry in a desiccator for overnight. Using the same instrument, the high-resolution TEM

(HRTEM) were collected and examined for the interplanar spacing of the synthesized photocatalysts, the EDS was carried out to determine the elemental distribution and mapping, and selected area diffraction pattern (SAED) were also collected to find out the crystal planes.

2.6.5 Field emission scanning electron microscope (FESEM)

The FESEM (Model: JSM-7610F; Make: JEOL, Japan) was used to characterize the dimensions (undercut and depth) and the surface morphology of the microchannels, and the surface morphology and thickness of the coated photocatalyst in the OFMRs.

2.6.6 Profilometer

The microchannel dimensions (undercut and depth) and roughness of OFMR before and after the photocatalyst coating were examined by using the profilometer (Make: Veeco; Model: Dektak 150, The USA). Step heights of wavy microstructure in the C-SOFMR were also characterized.

2.6.7 Photoluminescence (PL) spectrometer

The PL spectra were collected using PL spectrometer (Model: Fluoromax-4; Make: Horiba Jobin Yvon, Japan) to understand the PL quenching of excitons at an excitation wavelength of 400 nm for the synthesized powder CdS, CN, and CN/CdS heterojunction photocatalysts.

2.6.8 X-ray photoelectron spectroscopy (XPS)

The XPS (Model: ESCALAB Xi^+; Make: Thermo Fisher Scientific Co., U.K.) analysis were performed with the twin anode Non Monocromated ESCALAB Xi^+ to understand the interaction of CN with CdS. The working pressure of argon, pass energy and electron take-off angle were ~3×10^{-9} mBar, 20 eV and 55°, respectively. The spectra of Cd, S, C, and N were obtained by fitting raw data with Gauss-Lorentz curve after subtraction of Shirley background using XPSPEAK4.1 software.

2.6.9 Microscale particle image velocimetry (µ-PIV)

µ-PIV experimental set-up: The schematic diagram of the µ-PIV experimental setup as shown in **Figure 2.6**. The syringe pump (Make: Harvard apparatus, Model: PHD ULTRA, USA) was used to monitor injection flow rate to the P-SOFMR and C-SOFMR. The OFMR was placed under the inverted microscope for the flow visualization. The objective lens with magnification (20×) was used in the experiments. The fluorescence illumination source (high-pressure mercury lamp) was used to illuminate the region of interest in the OFMR. A high-speed CMOS (complementary metal oxide semiconductor) camera (Make: VEO 640L Model: Phantom, The USA), with maximum resolution 2560×1600, was used to capture the image sequence, and dynamic studio (Dantec dynamics) software was used for the image processing. Experiments were conducted at room temperature and atmospheric pressure. Different sets of experiments with two-phase/single-phase flows were conducted to quantify the flow dynamics in P-SOFMR and C-SOFMR.

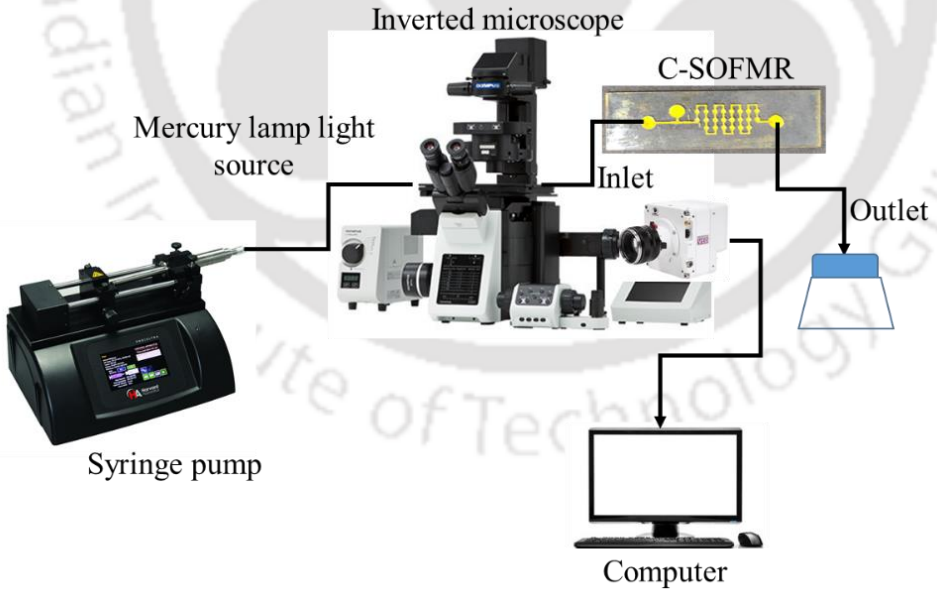

Figure 2.6: The µ-PIV experimental set-up.

Image Processing: The flow rate used in the flow visualisation experiments was 0.001 mL/min. At 40 FPS, a collection of 200 photos was taken. Dynamic studio 6.3, a commercial software, was used for the image processing (Dantec dynamics). Utilizing the micro-PIV

approach, the cross-correlation method yields the flow field. Image calibration, image pre-processing, masking, vector calculation, and vector post-processing are some of the processes involved in image processing. The image sequence is initially imported and calibrated in the software. Based on the height and width of the image, a scale factor was used. The region of interest (ROI) was chosen for the image flow field, and the dynamic range of the flow field inside the image was altered for improved contrast during image pre-processing. Background noise was removed from reflections, and unfocused particles were utilised to lower the signal-to-noise ratio (SNR). For background removal, an ensemble minimum image was computed and subtracted from the instantaneous raw images. The image masking was used to hide places where fluid was not flowing or of no importance (or the area without particles). Circles were made around the portions of the images that contained no particles after computing the image maximum.

Table 2.2: Characterization techniques used for analysis of the photocatalysts and microreactor morphology.

S.No.	Instrument	Make; Model	Specifications	Purpose
1	Optical microscope	DM2500M; Leica, Germany	---	Microchannel morphology
2	Diffuse reflectance UV-vis spectrophotometer	UV-2600; Shimadzu, Japan	BaSO4 as a reference, Wavelength 200-800 nm	Optical absorbance
3	Electron dispersive X-ray (EDX) spectroscopy	Sigma; Zeiss, Germany		Surface elemental analysis

4	Electron dispersive X-ray (EDX) spectroscopy	JEM-2100F; JEOL, Japan		Surface elemental analysis
5	Field emission scanning electron microscope (FESEM)	JSM-7610F; JEOL, Japan	15kW Current and 7V probe voltage	Size and surface morphology
6	Field emission transmission electron microscope (FETEM)	JEM-2100F; JEOL, Japan		Size and surface morphology
7	Fourier-transform infrared spectroscopy (FTIR)	IR Affinity 1; Shimadzu, Japan		Functional group characterization
8	Gas chromatography (GC)	7890A; Agilent, The USA	Oven temp 50°C, Injector temp 200°C, TCD detector 250°C	Hydrogen assessment
9	Photoluminescence (PL)	Horiba Jobin Yvon; Fluoromax-4, Japan		Photo charge carrier separation
10	Spin coater	SpinNXG-P1; Apex Instruments, India		Catalyst coating

11	Surface profilometer	Dektak 150; Veeco, USA		Thickness of the film
12	Ultrasonic bath	USC 200; ANM industries, India		Cleaning microchannels
13	X-ray photoelectron spectroscopy (XPS)	ESCALAB Xi+; Thermo Fisher Scientific Pvt. Ltd., The UK		Surface states and chemical composition
14	X-ray powder diffraction (XRD)	SmartLab, Rigaku, Japan		Crystallinity
15	Mask writer	Dilase 250; Kloe, France		Photolithography
16	High speed camera	VEO 640L; Phantom, The USA		Flow visualization
17	Inverted microscope	IX-83; Olympus, Japan		Flow visualization

2.7 Photocatalytic activity test

The CdS coated optofluidic microdevice (150×0.474×0.159 mm^3) was tested for gas-liquid and liquid (water + SR) phase water splitting reaction in the presence of SR (0.1 M Na_2SO_3/Na_2S for gas-liquid). The geometric area of the microchannel was 1.05 cm^2 and it irradiated with UV light (254 nm) for gas-liquid and metal halide lamp for liquid phase as a light source. The metal halide lamp was having an inbuilt UV blocker which effectively blocks the UV light. Moreover, the OFMRs were fabricated out of borosilicate microscopic glass which also does

not allow UV light to penetrate. Therefore, the photocatalyst was irradiated with only visible light. The schematic of the experimental setup used for this purpose is shown in **Figure 2.7**.

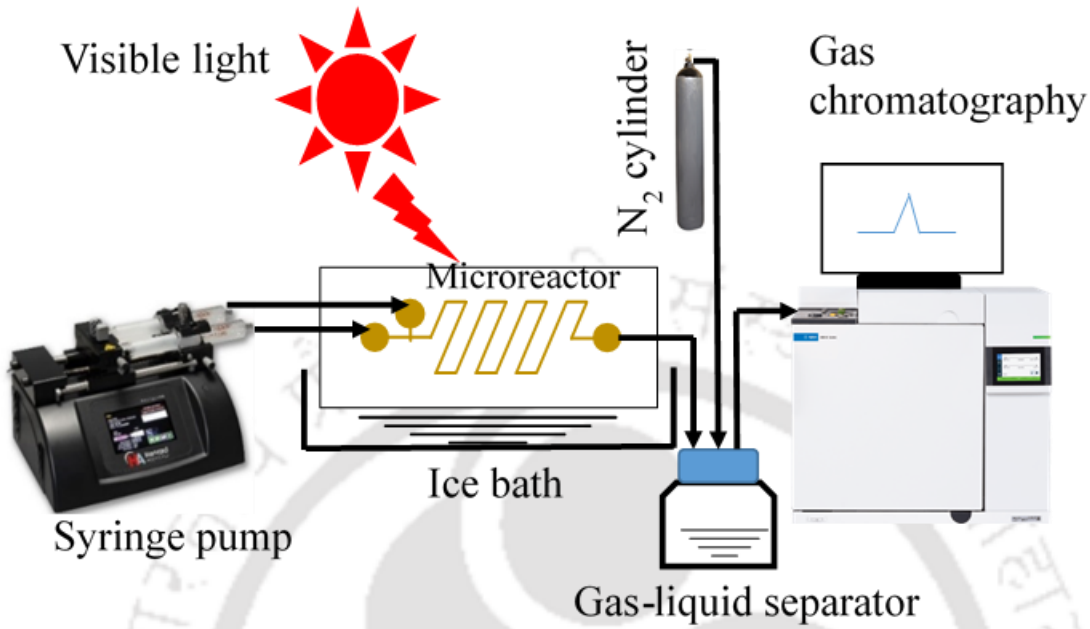

Figure 2.7: Photocatalytic water splitting experimental setup.

The gas and liquid flow rates were maintained/monitored using a mass flow controller and a syringe pump (Make: Harvard apparatus, Model: PHD ULTRA, USA), respectively. The microreactor outlet and the inert (sweep) gas inlet were connected to a gas-liquid separator. The N_2 was used as sweep gas at a flowrate of 3 mL min^{-1}. The entire system was purged with N_2 gas prior to each experimental run, to remove oxygen present. The produced H_2 gas was evaluated using offline for gas-liquid and online gas chromatography (Model: 7890A, Make: Agilent, USA) for liquid phase system that is integrated to the setup (**Figure 2.7**). The OFMR was partially submerged in an ice bath to prevent overheating of the device. The emission spectrum of 400 W metal halide lamp was recorded by the spectrophotometer and shown in **Figure 2.8**. All the experiments were performed inside the black box to avoid the interference of stray light. The generated H_2 and O_2 were analyzed at 10 min intervals using an online gas chromatograph (GC; Model: 7890A, Make: Agilent, The USA) equipped with a thermal conductivity detector (TCD) and a CP-Molsieves 5A column with the N_2 gas at a flowrate of

20 mL/min as a sweep gas. The argon was used as the carrier gas. The calibration curve for H_2 measurements is shown in

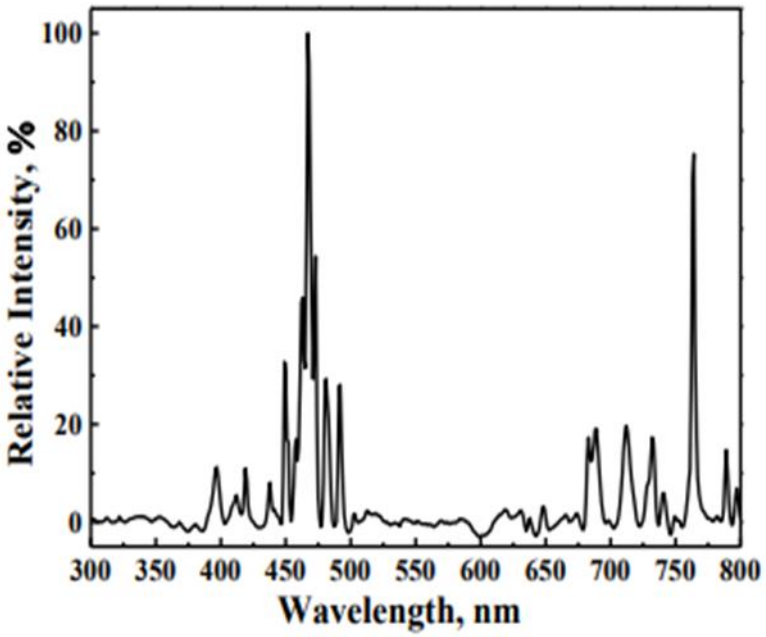

Figure 2.9.

Figure 2.8: Emission spectrum of the 400 W metal halide lamp.

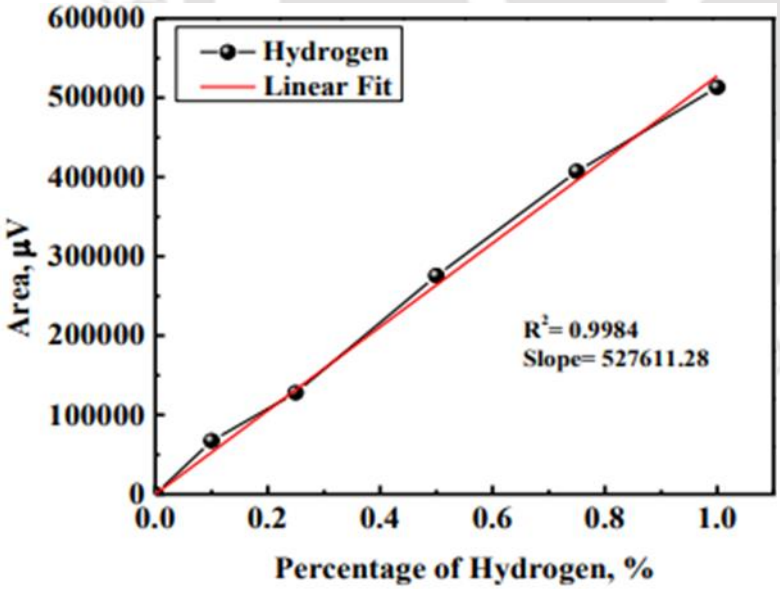

Figure 2.9: Calibration graph for H_2 gas.

2.6 Calculation details of the apparent quantum efficiency (AQE)

The energy of one photon (E_{photon}) with wavelength of λ (nm)

$$E_{photon} = \frac{hc}{\lambda}$$

h is Planck's constant = 6.626×10^{-34} J s

c is the speed of light = 3×10^{8} m s^{-1}

λ is the wavelength of the incident light = 420 nm = 4.20×10^{-7} m

The total energy of the incident monochromatic light (E_{total}):

$$E_{total} = P \times A \times t$$

Where

P (W m^{-2}) is the power density of the incident light

A (m^2) is the irradiation area and

t (s) is the duration of the incident light exposure.

As we used 400 W metal halide lamp at L = 10 cm distance,

$$P = \frac{power}{4\pi \times L^2}$$

$$A = 1.05 \times 10^{-4} (m^2)$$

$$\text{Number of incident photon rate} = \frac{E_{total}}{E_{photon}}$$

The apparent quantum efficiency (AQE) is defined as follow by substituting twice the number of H_2 molecules evolved for the number of reacted electrons.

$$\text{AQE (\%)} = \frac{H_2 \text{ production rate}}{\text{Photon incidence rate}} \times 100$$

Therefore, the AQE is calculated using the following equation:

767 $$\text{AQE}\ (\%) = \frac{2 \times n_{H_2} \times N_A}{\text{Photon incidence rate}} \times 100$$

768

769 Where,

770 n_{H2} is the H_2 evolution rate

771 N_A is Avogadro's constant = 6.022×10^{23} mol^{-1}

772

Chapter 3

Fabrication of optofluidic glass microreactor

This chapter briefs a simple, rapid, and cost effective adhesive tape based glass fabrication. A comparison of fabrication methods (such as photolithography and adhesive tape as mask) was made based on the geometrical shape and etch factor. The microchannels without any wall irregularities were obtained with the adhesive tape. The new approach developed in this study is a step forward in fabricating highly efficient and inexpensive optofluidic devices.

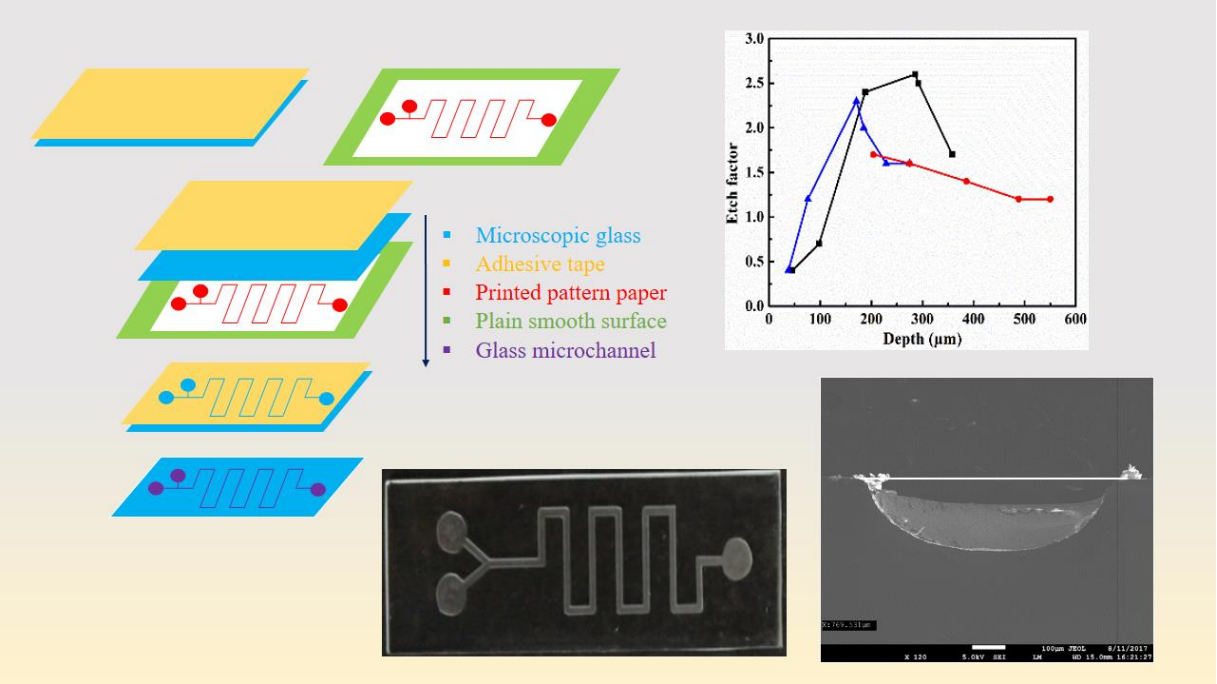

Note: Part of this chapter is published in International Journal of Hydrogen Energy.

P. Rambabu, S. Patel, D. Gogoi, R.V. Uppaluri, and N.R. Peela, Optofluidic microreactor for the photocatalytic water splitting to produce green hydrogen, *International Journal of Hydrogen Energy* 47 (2022) 2152-216.

3.1 Adhesive tape as a mask

3.1.1 Effect of etchant concentration with and without stirring

The aspect ratio is defined as the ratio of depth (D) to width (W). The undercut (U) is defined as $(W_f - W_i)/2$, here W_i and W_f are initial and final widths, respectively. A deeper microchannel with no undercut (high aspect ratio) is desired to facilitate good flow dynamics. Using mask possessing strong resistance to the etchant, a deeper microchannel can be achieved. However, due to the isotropic etching of glass in HF, the undercut is unavoidable.

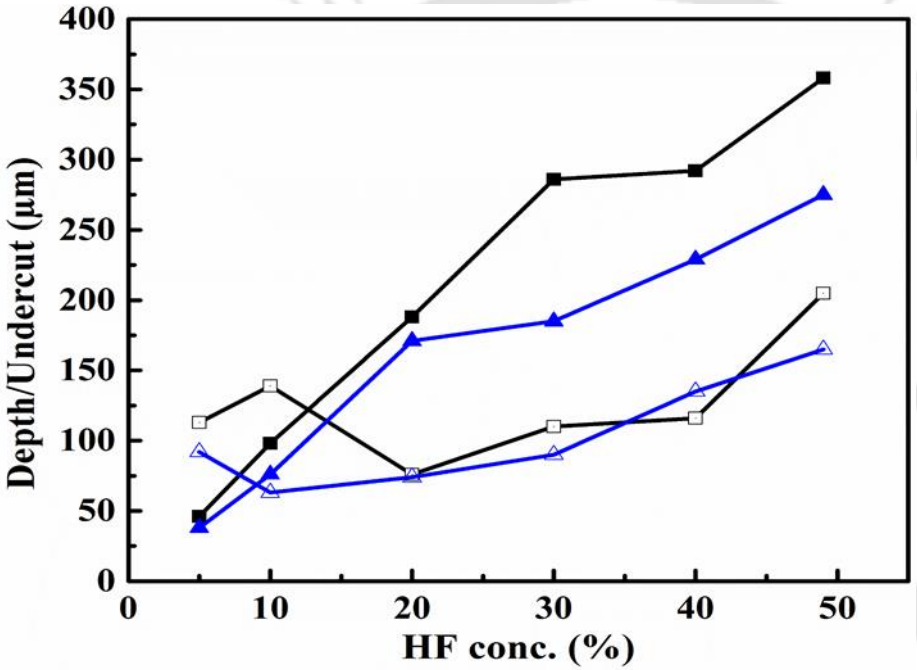

Figure 3.1: The depth (■, ▲) and undercut (□, Δ) as a function of HF concentration (%): with (■, □) and without (▲, Δ) stirring.

The effect of etchant concentration (with and without stirring) on the microchannel depth and undercut is shown in **Figure 3.1**. The depth increased from 46 to 358 μm and 38 to 275 μm for stirring and no stirring cases, respectively, as the HF concentration increased from 5-49%. As expected, the microchannel depth increased linearly with HF concentration for the both cases.

The depth with stirring was higher than that without stirring as the mixing indices enhanced mass transfer of the etchant to the surface.

The undercut varied non-linearly from 113–205 µm and 92–165 µm for stirring and without stirring cases. The minimum undercut of 63 µm was obtained for 10 wt.% of etchant for the without stirring case. The minimum undercut for stirring case was 76 µm with 20 wt.% of etchant. The higher undercut in the stirring case could be due to the transfer of etchant in the lateral direction and enhancement in the isotropic etching. For the without stirring case, the etchant is tracked[153] by an adhesive tape pattern which eventually causes vertical etching. At low HF concentrations (5% and 10%), the undercut was higher for the stirring case as compared to that without stirring. This is due to dilution brought forward to the adhesive tape due to larger quantity of water molecules and subsequent stirring force assisted etchant transport in the

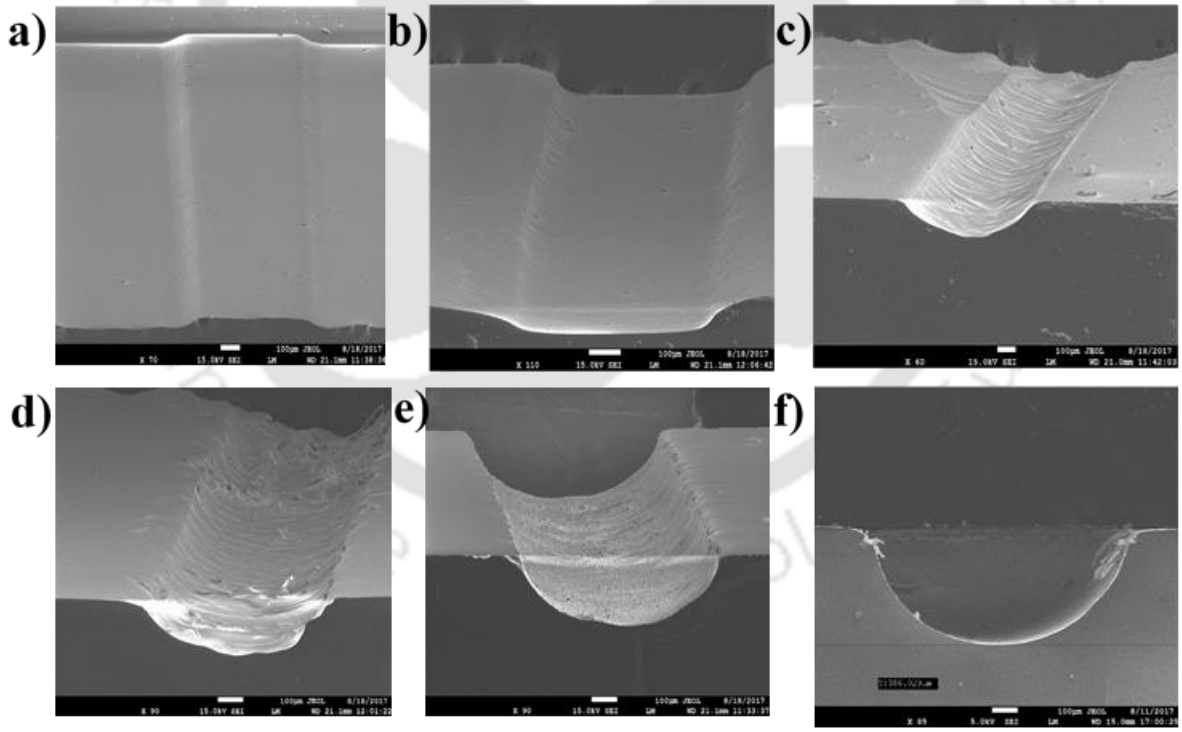

Figure 3.2: FESEM images of glass microchannels obtained at various etchant concentrations and (a) 5%, (b) 10%, (c) 20%, (d) 30%, (e) 40%, and (f) 49%. (Other conditions: Etching time = 1h and No stirring).

lateral direction. Progressively, the undercut reduced at higher HF concentration from 20 to 40%. For both the cases, the increase in undercut with HF concentration can be observed. The microchannel width expansion has been observed due to isotropic etching but not due to either peeling off or damage to the adhesive tape.

The surface morphology of the microchannels from FESEM is shown in **Figure 3.2**. It can be observed that the microchannels fabricated with intermediate HF concentrations (20 and 30%) possessed uneven structures and wall damages (**Figure 3.2c** and **d**). The microchannels with rounded edge, smooth surface, and rectangular shape were formed (**Figure 3.2a** and **b**) at low concentrations of HF (5 & 10%). At 40% and 49% HF, semi-circular microchannels with sharp edges and without any grooves were achieved. With increasing concentration of the etchant, microchannel morphology improved and hence the further experiments were conducted with 49% etchant concentration. With this, deeper glass microchannel with majorly sharp edges and appropriate roughness could be achieved along with minimization of minor wall defects due to elevation of the adhesive gum. Since the case without stirring provided low undercut, further experiments have been conducted for highest etchant concentration and by considering variations in the time of etching.

3.1.2 Effect of etching time

The effect of etching time on the microchannel geometry was investigated in the etching time range of 15 to 120 min at 49% etchant concentration (**Figure 3.3**). The semi-circular microchannels with sharp edges were formed at all etching times (**Figure 3.4**). The increase in the undercut with etching time was due to isotropic etching with concentrated HF and not due to peeling of the adhesive tape.

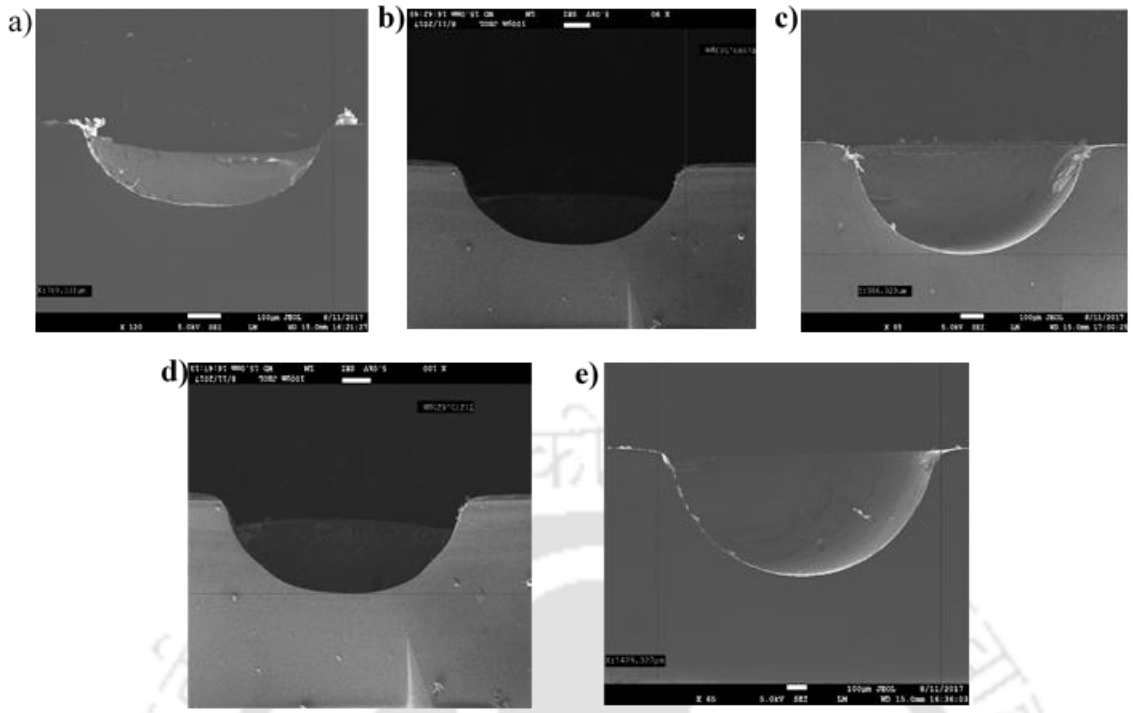

Figure 3.3: The FESEM images of glass microchannels obtained at different etching times (a) 15 min, (b) 30 min, (c) 60 min, (d) 90 min, and (e) 120 min. (Other conditions: HF concentration = 49% and no stirring).

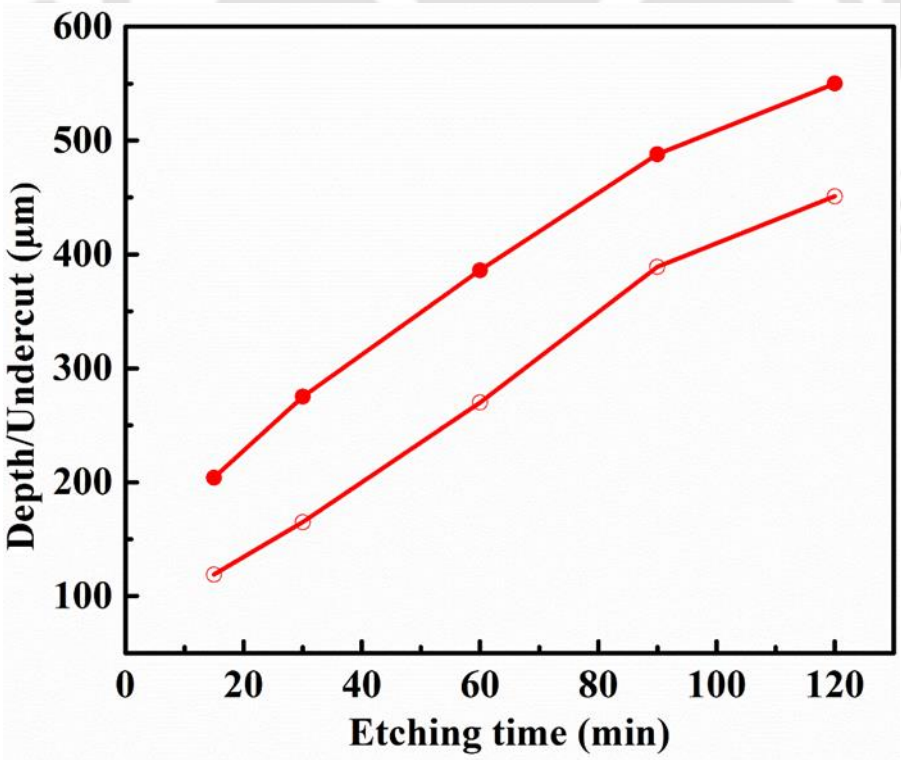

Figure 3.4: Depth (●) and undercut (○) as a function of etching time. (Other conditions: Etchant concentration 49% and No stirring).

3.2 Photoresist as mask

3.2.1 Effect of etching time

From the literature it was understood that the higher initial width of the microchannel increases the undercut[154]. Hence, the microchannel initial width in the present case was taken lower than that set during adhesive tape-based fabrication. With 20% HF as etchant, the undercut and depth were increased linearly in the range of 222 – 421 µm and 143 – 274 µm, respectively, with etching time increased from 30 to 120 min (**Figure 3.5a**). Also, longer etching time resulted in peeling off of the photoresist due to isotropic etching of glass and subsequent weakening of the photoresist film adherence or film damage.[155-156]

3.2.2 Effect of etchant concentration

At fixed etching time 1 h and stirrer speed (70 rpm), as the HF concentration was increased from 5 to 30%, the undercut (260 – 356 µm) and the depth (32 – 331 µm) were increased linearly (**Figure 3.5b**). At higher concentration of HF (40%), no channels were formed and entire photoresist got peeled off within a short time, indicating a poor photoresist survival in concentrated HF. The higher undercut in comparison with the microchannel depth could be due to mass transfer limitations[157] and etching in lateral direction.[154,158] For all cases, compared to adhesive tape case, the undercut was higher for the photoresist case.

An attempt to fabricate serpentine shaped microhannels on glass using photoresist as mask resulted in microchannels with cracks on the wall throughout the length of the channel (**Figure 3.6**). This could be attributed to overshoot during laser mask writing in curvy patterns in both X and Y directions. Hence, photolithography has a fundamental limitation to achieve high quality microchannels.

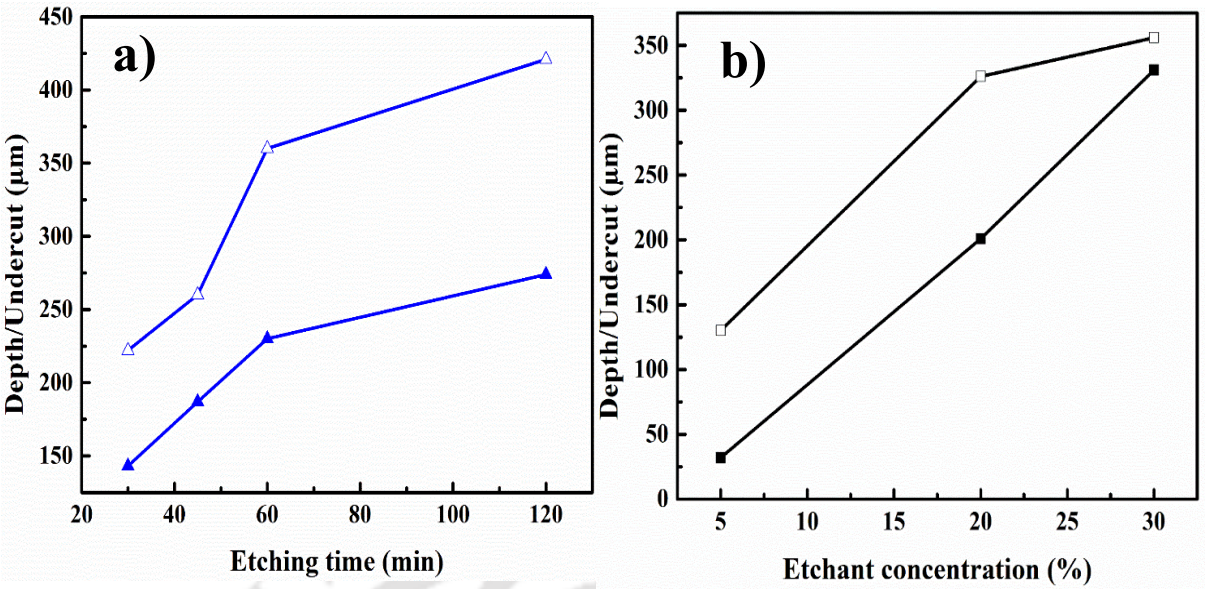

Figure 3.5: Etching time and etchnt concentration as a function of depth (■) and undercut (□) and depth (▲) and undercut (Δ) with photoresist as mask.

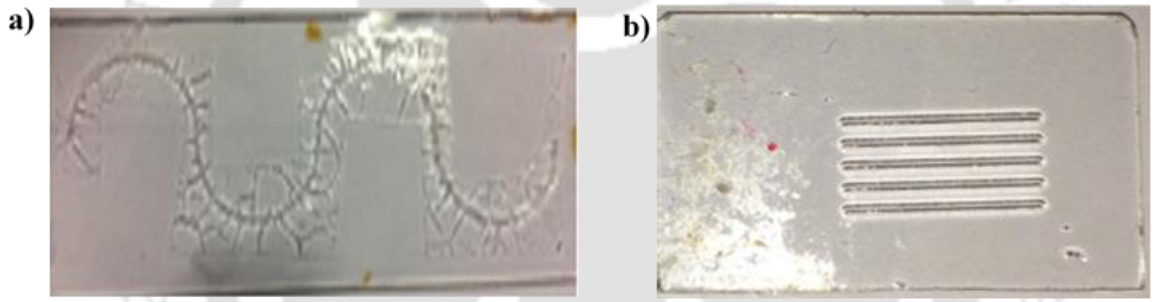

Figure 3.6: (a) Wavy and (b) straight microchannels obtained using photolithography followed by chemical etching.

3.3 Etch factor

Defined as the ratio of depth to undercut, the etch factor affirms channel aspect ratio. The etch factor as a function of depth is shown in Figure 3.6 for parameters HF concentration and etching time with adhesive tape (**Figure 3.7a**) and photoresist (**Figure 3.7b**) as mask. The etch factor Vs depth profile for variation of HF concentration with and without stirring followed a similar trend: initially increased linearly and then decreased with depth (**Figure 3.7a**). The maximum etch factor was higher under stirring conditions (2.6) as compared to that without stirring (2.3). The etch factor at lower depths was lower under stirring as compared to that without stirring

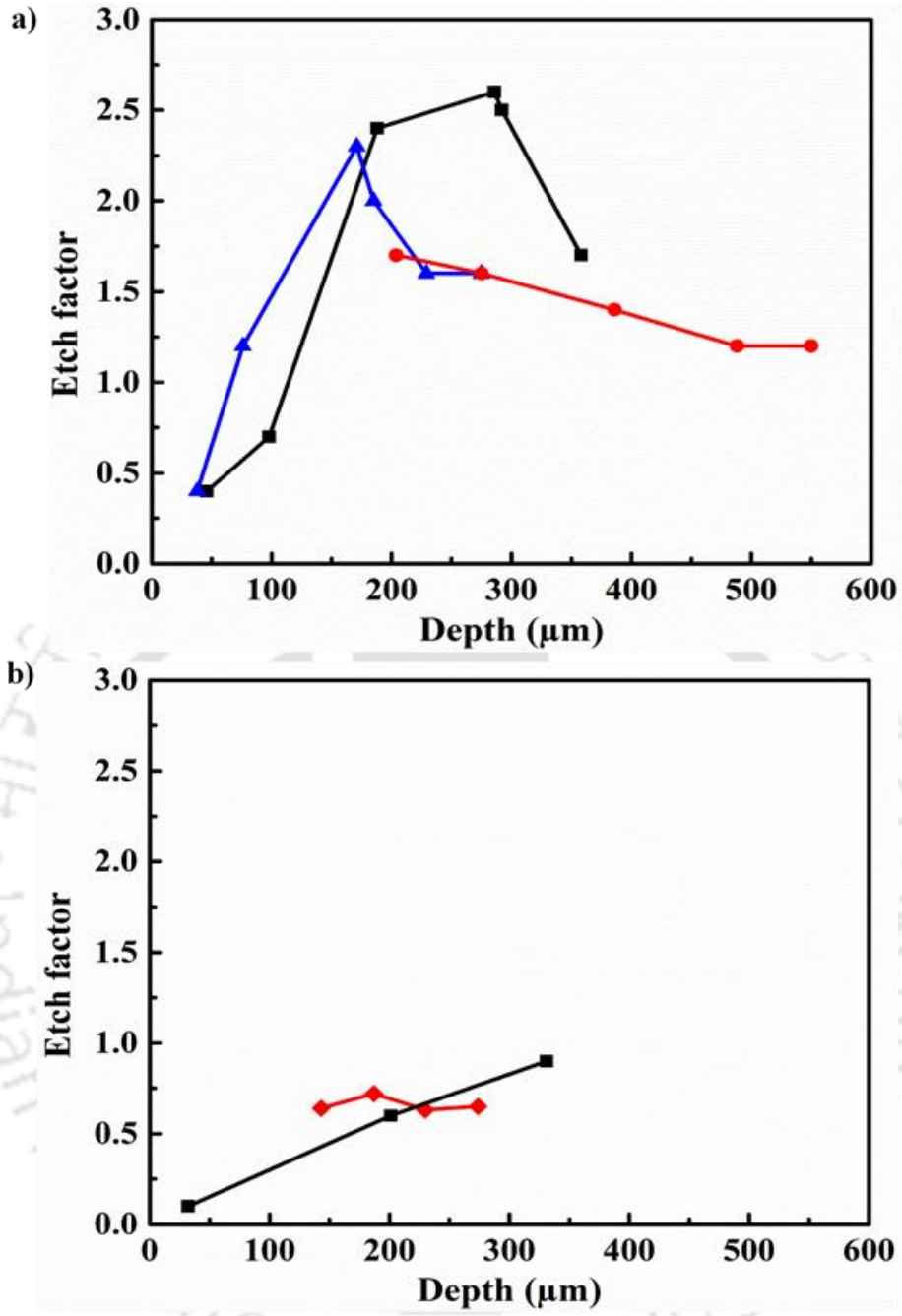

Figure 3.7: The variation of etch factor as a function of microchannel depth: Using adhesive tape (a) and photoresist (b) as mask. (Variation of HF concentration with (■) and without (▲) stirring and etching time with (♦) and without (●) stirring).

and the trend was reversed at higher depths. The etch factor was marginally decreased with depth for an etching time upto 90 min and reached to a constant value (1.2) thereafter. With photoresist as mask and for HF concentration variation (**Figure 3.7b**), the etch factor was increased with depth reaching a maximum of 0.9 at higher concentration. While, it was nearly constant (at 0.7) with etching time. However, prolonged etching escalates the photoresist film

damage and leads to peeling off of the photoresist. The highest etch factor (0.9) obtained with photoresist as mask was lower than the lowest (1.2) etch factor obtained with adhesive tape as mask. When compared at the same depths, the etch factor for adhesive tape case is higher by a factor of 2.5.

This indicates that the undercut was higher in the case of photoresist as mask. Adhesive tape as a mask resulted in lower undercut (451 µm), higher depth (550 µm), and lead to higher etch factor (1.2). The depth of the microchannels obtained with adhesive tape are not only better than that obtained from photoresist method but also was highest as compared to that reported in literature using chemical etching method (Table 1.1). This could be attributed to the strong bonding of the mask with glass. The etch factor is highly sensitive to etchant concentration but not to the etching time. Interestingly, the trend of etch factor vs depth from adhesive tape and photoresist cases were similar to each other. In the case of adhesive tape, the mask damage or peel off was not observed. However, in the case of photoresist, the mask was peeled off and damaged at higher etching times as well as at higher HF concentrations.

3.4 Microchannel morphology

Figure 3.8a presents the optical image of the pattern created on the adhesive tape using surgical knife in which the thick black horizontal line corresponds to the adhesive glue on the edges of opening. As a simple and rapid procedure, the surgical knife based cutting approach facilitated achieving good microchannels. The control on obtaining the desired shape of the microchannel was facilitated by the strong resistance of the adhesive tape mask to the chemical etchant. The strong adherence of the adhesive tape, due to its glue, contributes towards elevation of the minor crevices at the microchannel edges (**Figure 3.8b**) at which mass transfer limitations exist[159]. Well-defined shape of the microchannel can be assured due to strong adhesive nature[156] and inertness of the tape to the etchant (**Figure 3.8b**). At high HF concentration, due

to uniform etching, grooves did not form. The desired characteristic of semi-circular microchannel with a sharp edge for finer manipulation of fluidics can be achieved rather than the rounded wall edge of the channels.[160,161] Using photoresist as a mask, neither deeper microchannels nor well-defined edges were obtained, which was due to the poor photoresist adherence during etching. Microchannels with rounded wall edges were formed with photolithography (**Figure 3.8c**), which is not desirable attribute of the microchannel, given the fact that the fluid flow cannot be confined and controlled in such a microchannel. The fluid flow over the rounded wall edge acts as a dead zone and does not indicate higher transport efficiency.

In summary, compared to the photoresist case, microchannels with low undercut (451 µm) and maximum depth (550 µm) were obtained using adhesive tape as mask and this translates into higher aspect ratios (etch factor = 1.2). Moreover, adhesive tape can eliminate typical procedures associated to photoresist such as parameter sensitivity against the etchant, coating, thickness factor, annealing and expensive photoresists. Further, cutting with the knife eliminates the expensive laser writing step.

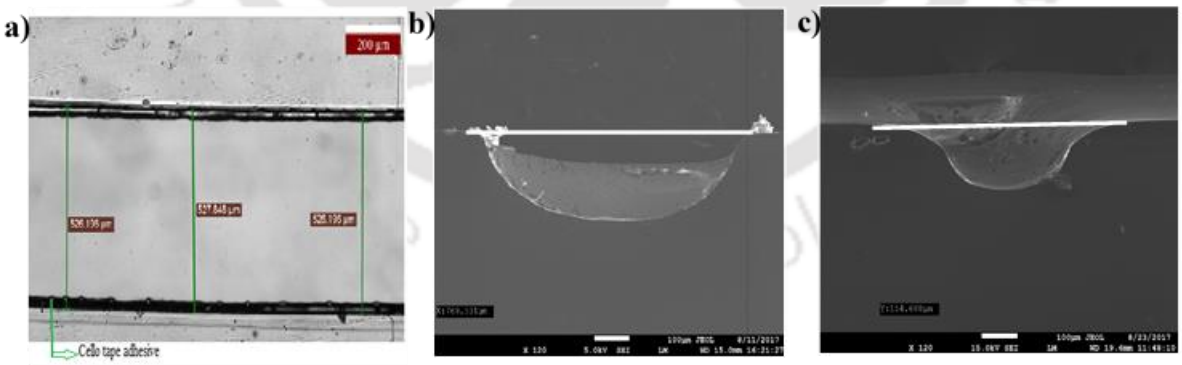

Figure 3.8: The optical microscope image of the pattern created by cutting the adhesive tape (a); The FESEM image of microchannel obtained using adhesive tape (b) and photoresist (c) as mask.

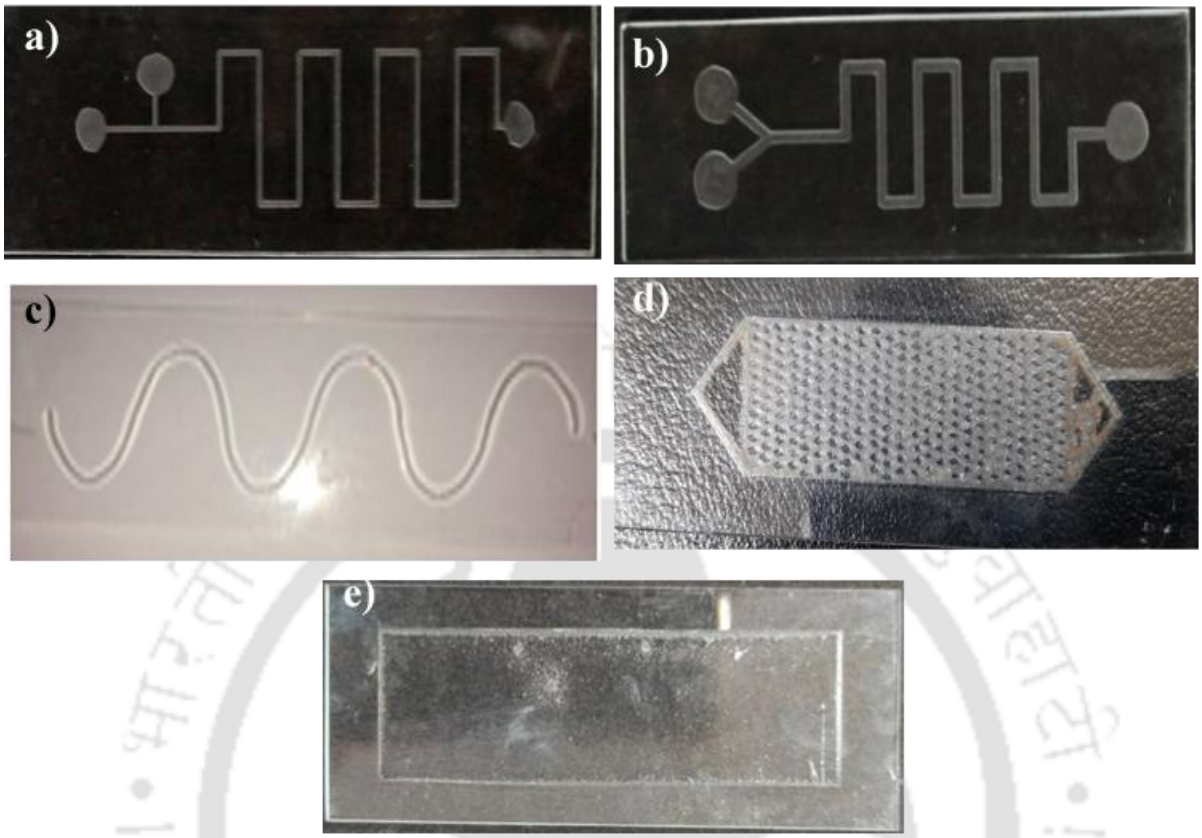

Figure 3.9: Various microchannel shapes fabricated using adhesive tape as mask: Serpentine microchannels with (a) T-Joint (b) Y-shaped, (c) wavy, (d) micro pillar, and (e) planar microchannel.

Microchannels with various shapes namely serpentine microchannel with inlet and outlet reservoirs, and T-joint (**Figure 3.9a**) or Y-shaped (**Figure 3.9b**) inlets, wavy microchannel without reservoirs (**Figure 3.9c**), micropillared (**Figure 3.9d**), and planar (**Figure 3.9e**) were successfully fabricated using adhesive tape and 49% HF solution as an etchant. Compared to all other methods reported in the literature[64,160,] this method is inexpensive as it requires only an adhesive tape, a surgical knife and a microscopic lens for visualization. Robotic extensions of the method can be adopted for better precision, if necessary. However, the developed simple method effectively demonstrates the generation of microchannels in semi-circular shape without any wall irregularities.

3.5 Inlet and outlet connections

A similar procedure was followed to make inlet and outlet connections on the cover plate. The adhesive tape was applied on both sides of the cover plate and was cut in a rectangular shape at the inlet and outlet holes, followed by etching with 49%. A 1/16" plastic tube was attached to the etched inlet and outlet holes using glue and glass powder to achieve leak-proof inlet and outlet connections (**Figure 3.10**).

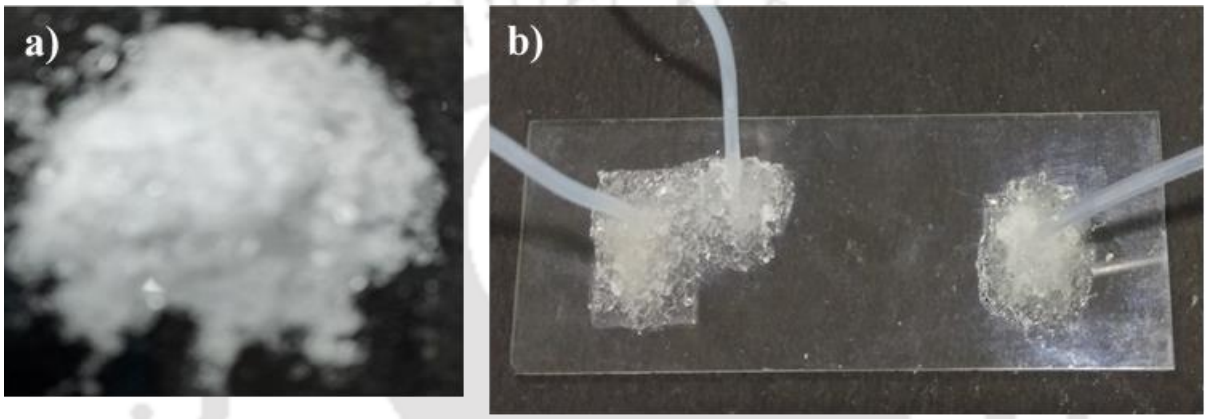

Figure 3.10: (a) Crushed microscopic glass powder (b) Cover plate with inlet and outlet tubing.

3.6 Assembly of microreactor modules

The photocatalyst coated optofluidic plate (Section 2.4) and the cover plate were combined with each other to form a complete optofluidic reactor using a UV curable glue. The UV curable glue was applied on the cover plate and then the optofluidic plate was attached to it. Then the glue was cured for 15 min under UV light. Thereafter, the optofluidic reactor was checked for leaks by submerging it into a water bath and passing an inert gas through the channels.

3.7 Conclusions

This work demonstrated the successful generation of glass microchannels with superior characteristics using adhesive tape as a mask. The method is simple, rapid, robust, and overcome the critical issues associated with photoresist masks such as adherence. Deeper

959 microchannels with sharp edges and without wall-irregularities were obtained. The depth and
960 undercut of 550 µm and 451 µm (etch factor 1.2), respectively, were obtained for an optimal
961 etchant concentration of 49% and etching time of 120 min. Using the developed method,
962 various microchannel shapes were successfully fabricated. The adhesive tape based fabrication
963 method, developed in this study, could enable achieving versatile microfluidic channels on the
964 glass.

965

966

967

968

969

970

971

972

973

974

975

976

977

978

979

Chapter 4

Optofluidic microreactor for the photocatalytic water splitting to green hydrogen production

This chapter describes various in-situ CdS photocalysts synthesis methods such as dynamic techniques and sol-gel method to coat in microchannel. The effect of parameters such as flow rate of the reactant and the concentration of sacrificial reagent (Na_2SO_3/Na_2S) on the photocatalytic hydrogen evolution experiments over the coated CdS photocatalyst under the visible light irradiation was studied. The H_2 evolution rate comparison in various OFMR designs such as serpentine, micropillared, and planar was undertaken. Finally, multiphase photocatalytic H_2 evolution in the serpentine OFMR studied by varying gas and liquid flow rates.

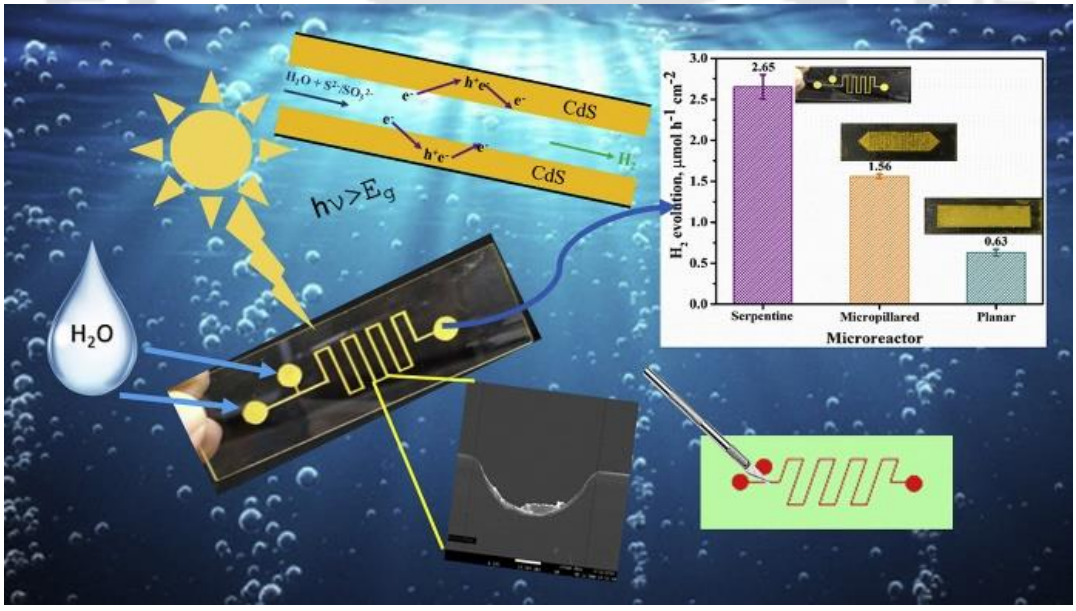

Note: Part of this chapter is published in Internation Journal of Hydrogen Energy.

P. Rambabu, S. Patel, D. Gogoi, R.V. Uppaluri, and N.R. Peela, Optofluidic microreactor for the photocatalytic water splitting to produce green hydrogen, *International Journal of Hydrogen Energy* 47 (2022) 2152-216.

4.1 CdS catalyst synthesis and coating in microchannel

4.1.1 In-situ CdS structural changes by dynamic method

The hexamethylenetetramine (HMTA) in the aqueous catalyst solution enabled the in situ CdS nanospikes growth in the microchannels at temperature 80 °C, as shown in **Figure 4.1**. The HMTA and heating temperature at 350 °C facilitated to obtain the CdS nanoleaf structure in the microchannel as shown in **Figure 4.2**. However, the film adherence was very poor during the photocatalytic experiments due to the developed fluid force in the microreactor. This method needs further study for the film adherence enhancement in the glass microreactor.

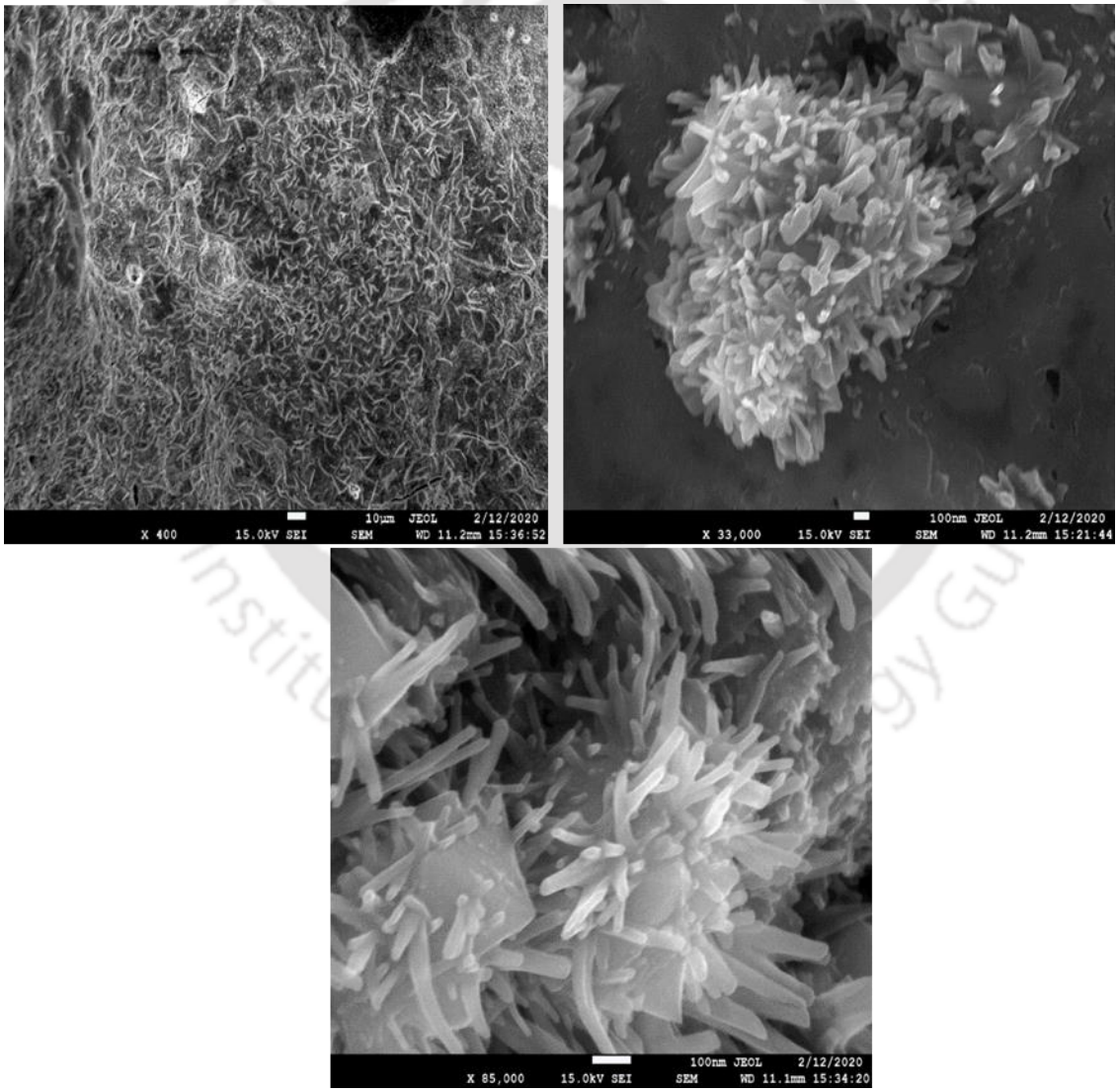

Figure 4.1: FESEM images of in-situ CdS nanospike synthesis in glass microchannel using dynamic synthesis.

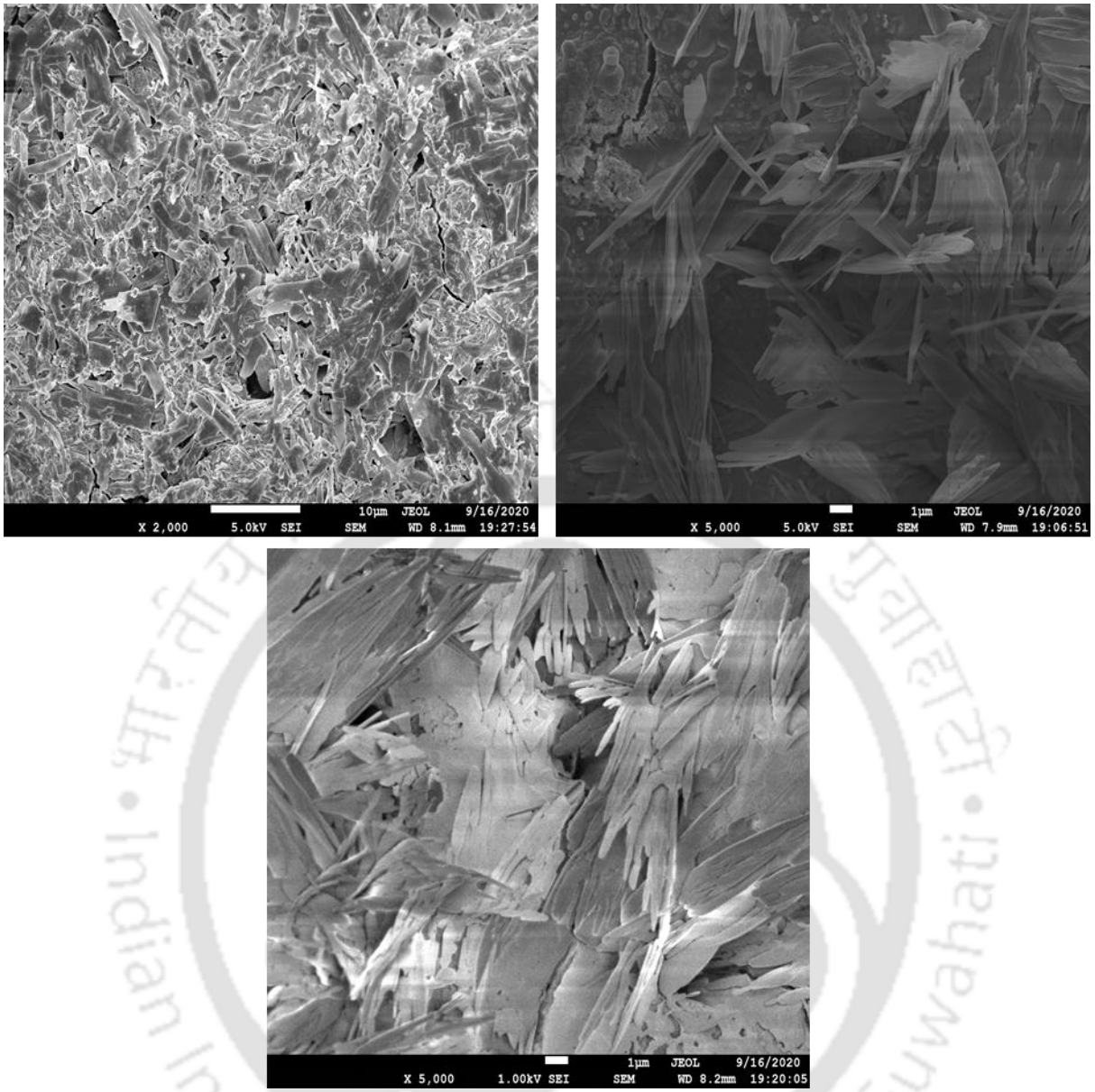

Figure 4.2: FESEM images of in-situ CdS nanoleaf structures in microchannel by chemical deposition method.

4.1.2 Characterizations of the CdS coated by sol-gel method

The rheological behavior of the catalyst solution was examined using rheometer at room temperature varying shear rate from 0 – 200 s^{-1}. At lower PEG loading (0.1 and 0.2 g), the catalyst solution exhibited a shear thinning behaviour, viscosity was decreased with the applied shear rate (**Figure 4.3a)**. At 0.3 to 0.5 g of PEG loading, the catalyst solution showed the shear thickening behaviour, viscosity was increased continuously with the shear rate. With the

addition of PEG to the catalyst, the viscosity was increased from 1.4 to 4.5 mPa s (**Figure 4.3b**), attributed to the fact that the PEG provided hydrophilic nature which facilitates the CdS particles association.

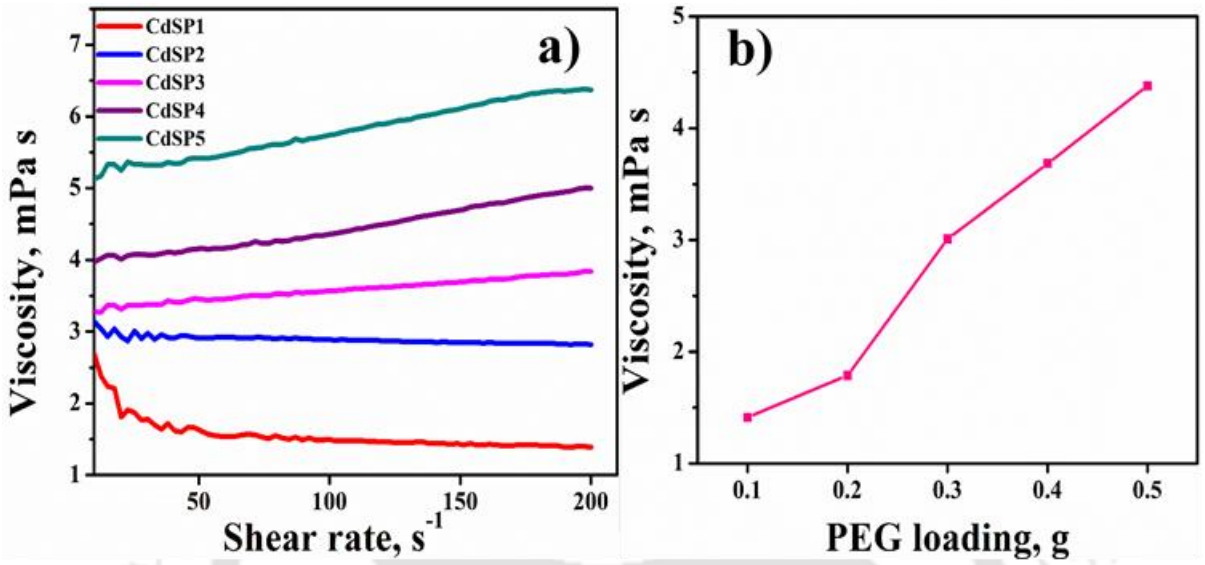

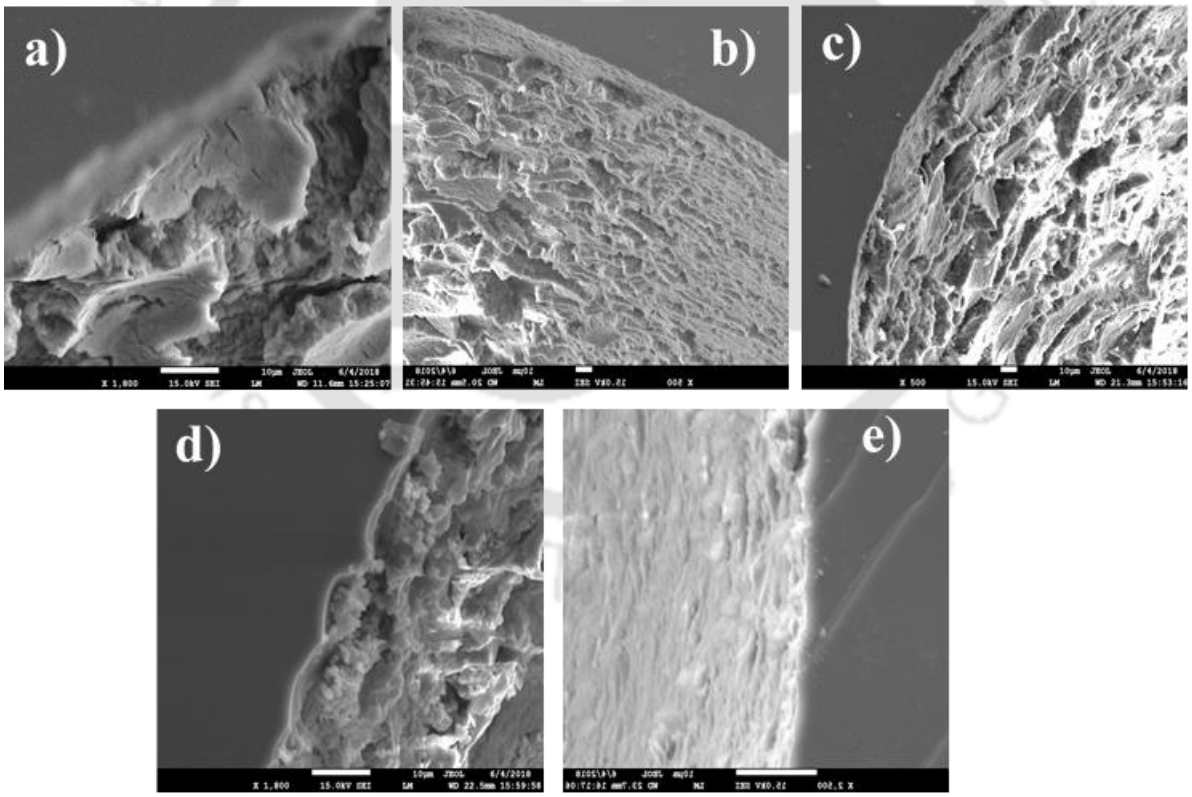

Figure 4.3: Viscosity of CdS catalyst solution with PEG loading.

Figure 4.4: FESEM images of the CdS photocatalyst coating enhancement in the microchannel with the PEG loading (g) (a) 0.1, (b) 0.2, (c) 0.3, (d) 0.4, and (e) 0.5.

The FESEM images depicts the improvement of the CdS coating in microchannels with the increase of PEG concentration (**Figure 4.4**). The CdS film induced cracks up to 0.3 g of PEG. At 0.4 g of PEG agglomerated CdS coated film coating was obtained. Continuous CdS film coating was attained at 0.5 g of PEG. Therefore, the PEG facilitated shear thickening behavior to the catalyst solution. The improved viscosity is beneficial to attaining the adherent and uniform coating in the microchannel.

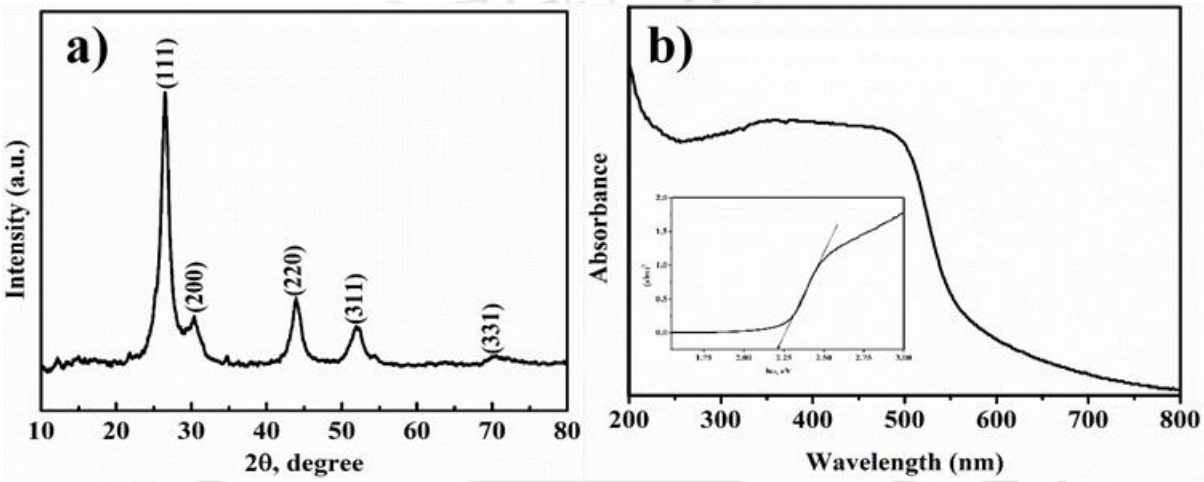

Figure 4.5: (a) XRD graph of the synthesized CdS catalyst. (b) UV–Vis absorption spectra of the CdS catalyst (inset Tauc plot).

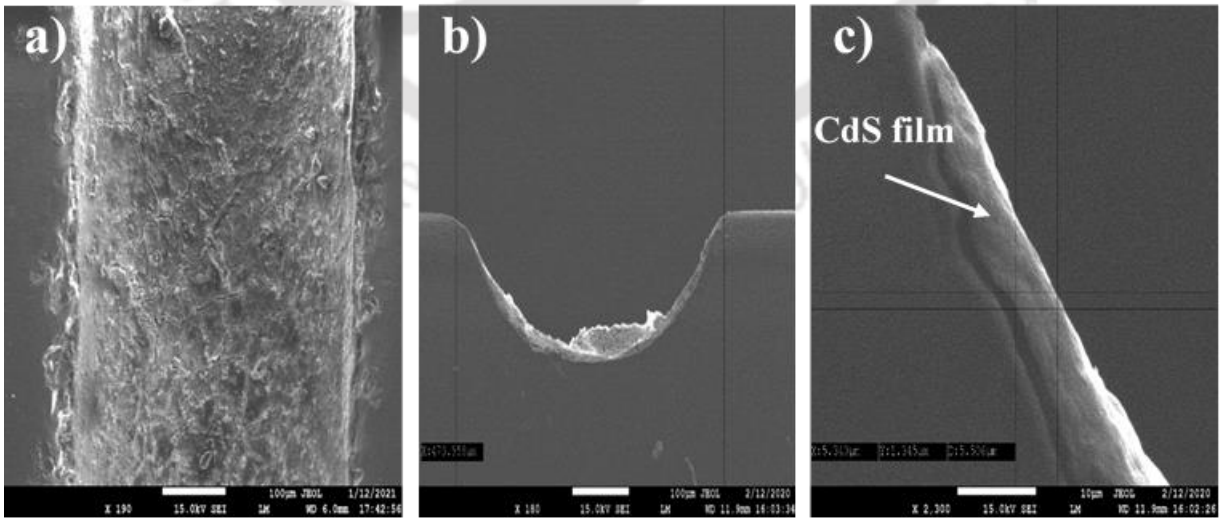

Figure 4.6: FESEM images of the CdS coated microchannel (a), (b), and (c).

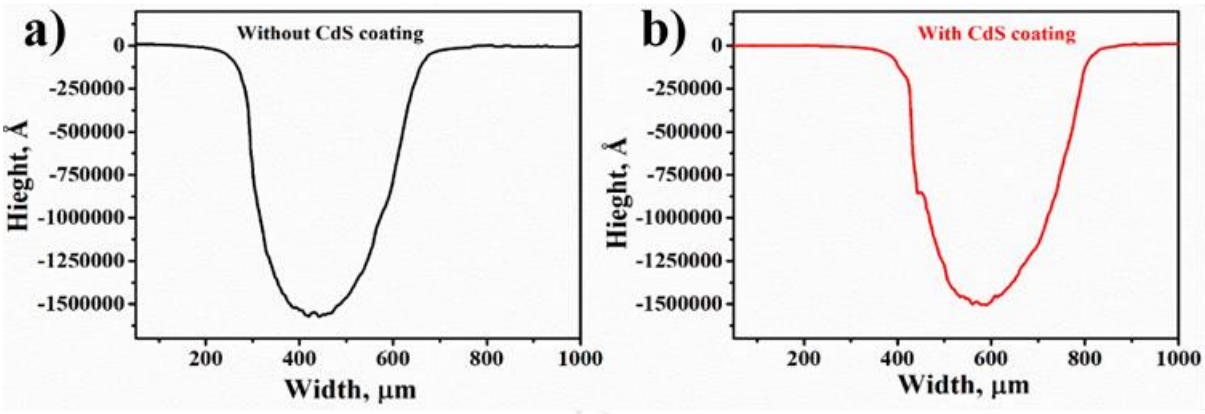

Figure 4.7: Profilometer graph indicates the microchannel geometry without (a) and with (b) CdS coating.

The XRD planes obtained at 2θ = 26.5, 30.6, 43.9, 52.0, and 70.3° affirmed the existence of the CdS photocatalyst [162] (**Figure 4.5a**). The crystallite grain size of 6.39 nm was calculated at 46.46° using the Scherrer equation ($D = K\lambda/\beta\cos\theta$). The UV-Vis absorption spectrum confirmed that the band gap energy of the synthesized CdS was 2.2 eV (**Figure 4.5b**). The FESEM images (**Figure 4.6**) of the CdS coated channel confirmed a uniform coating with an average thickness of approximately 5.5 µm. This was in good agreement with and the smooth curve in profilometer graph (**Figure 4.7**) indicates an uniform CdS coating.

4.2 Photocatalytic water splitting reaction

The morphology and film thickness of photocatalyst play an important role in the charge separation and transport and thereby enhance the hydrogen production rate [163],[164]. Therefore, the enhanced hydrogen production can be achieved through the intensification of surface reactions by using defect-free morphology [165]and optimum thickness in the optofluidic device. For metal sulphides (e.g., CdS), the hole-driven photo-oxidation of S^{2-} ions takes place to form sulphate (SO_4^{2-}) and/or sulphur (S°) [166]. A suitable sacrificial reagent with improved transport (by using optofluidic microdevice) to the active sites helps in mitigating the photo-corrosion of the photocatalyst.

The pertinent reactions at the CdS surface in the presence of the sacrificial reagent Na_2SO_3/Na_2S are as following [167]:

$$2H_2O + 2e^-_{CB} \rightarrow H_2 + 2OH^- \ldots\ldots\ldots\ldots\ldots\ldots (1)$$

$$2S^{2-} + 2h^+_{VB} \rightarrow S_2^{2-} \ldots\ldots\ldots\ldots\ldots\ldots\ldots\ldots\ldots (2)$$

$$S_2^{2-} + SO_3^{2-} \rightarrow S_2O_3^{2-} + S^{2-} \ldots\ldots\ldots\ldots\ldots\ldots (3)$$

$$SO_3^{2-} + S^{2-} + 2h^+_{VB} \rightarrow S_2O_3^{2-} \ldots\ldots\ldots\ldots\ldots\ldots (4)$$

$$S_2O_3^{2-} + 4h^+_{VB} + 6OH^- \rightarrow SO_3^{2-} + 3H_2O \ldots (5)$$

$$S^{2-} + h^+_{VB} + 6OH^- \rightarrow SO_3^{2-} + 3H_2O \ldots\ldots (6)$$

$$SO_3^{2-} + 2h^+_{VB} + 2OH^- \rightarrow SO_4^{2-} + H_2O \ldots\ldots (7)$$

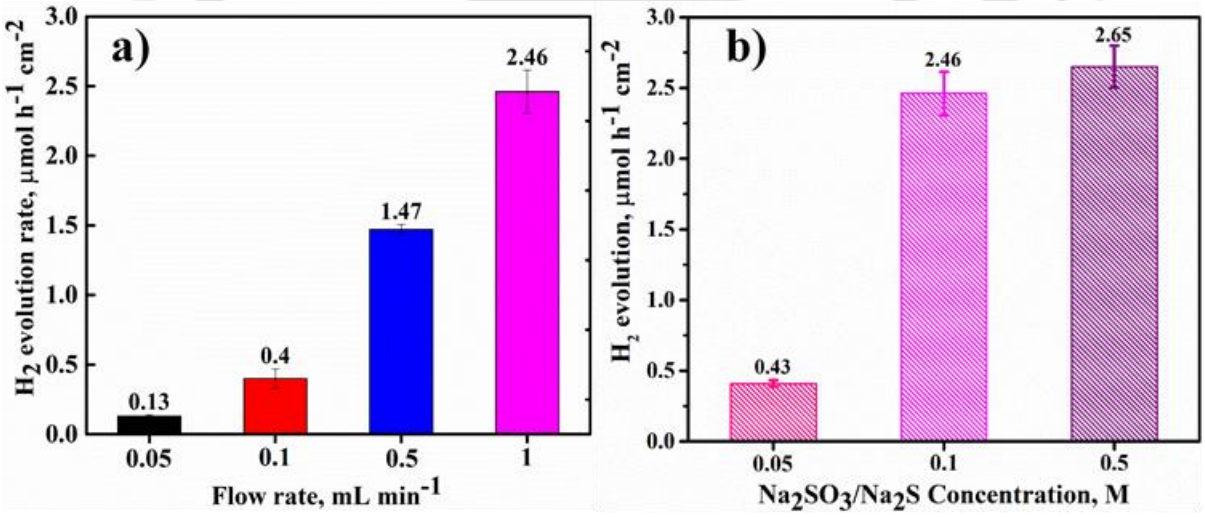

Figure 4.8: Photocatalytic hydrogen evolution rate as a function of as a function of flowrate (a) and Na_2SO_3/Na_2S concentration (b).

The hydrogen production rate in CdS coated optofluidic device was investigated as a function of feed flow rate in the presence of SR (**Figure 4.8**). The hydrogen evolution rate was increased

from 0.11 to 2.49 µmol h^{-1} cm^{-2} with the increase of liquid flow rate from 0.05 to 1.0 mL min^{-1} (**Figure 4.8a**). As the flow rate increases, the micromixing enhances [168],[169], and thereby the external diffusion of SR (Na_2SO_3/Na_2S) to the surface of CdS increases[170]. The higher flow rate represents the fast, fresh Na_2SO_3/Na_2S feed rate to the microreactor and the short residence time. This, in turn, facilitates the rapid quenching of holes in the valence band and thereby promoting the charge separation as well as suppression of photo-corrosion of CdS photocatalyst [81]. Such micro-scale phenomena potentially enhance hydrogen generation [171],[84]. The short residence times (e.g., 2.07 s at 1 mL min^{-1}) reduced the interaction time of the electron donor with the CdS, which in turn reduces the unnecessary side reactions of SR on the photocatalyst [83]. The maximum hydrogen production rate of 2.49 µmol h^{-1} cm^{-2} was obtained at flowrate 1 mL min^{-1}. Thus, the obtained results affirmed that the mass transfer rate of Na_2SO_3/Na_2S to the surface of the photocatalyst was increased with flow rate, which, in turn, facilitated the escalation of photocatalytic water reduction efficiency. This is one of the major advantages of the OFMR[172].

The effect of SR concentration (in the range of 0.05 – 0.5 M) on the H_2 generation is shown in **Figure 4.8b**. The maximum hydrogen of 2.65 µmol h^{-1} cm^{-2} was produced at 0.5 M of Na_2SO_3/Na_2S. The hydrogen production was increased with the increase of concentration of the Na_2SO_3/Na_2S from 0.05–0.5 M, due to the rapid scavenging of the holes from the CdS photocatalyst at higher concentrations of Na_2SO_3/Na_2S. The rate of increase of H_2 production rate was higher at lower Na_2SO_3/Na_2S concentration and levelled-off at higher concentrations. This indicates that the mass transport also increases with the increase of reactant concentration [81]. However, very high reactant concentration is not favourable as this may lead to adsorption of reactants/products/intermediates, poisoning the photocatalyst site [82].

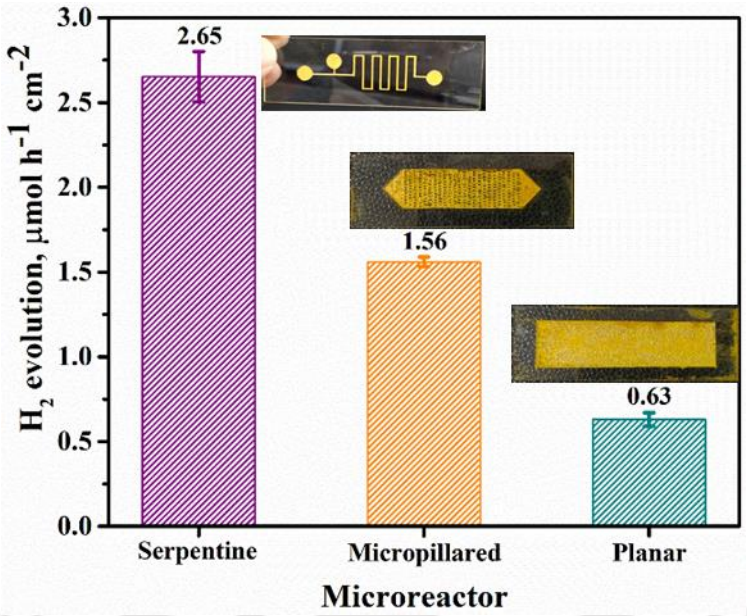

Figure 4.9: Comparison of the hydrogen production rates in serpentine, micropillared, and planar optofluidic microreactors.

To compare various reactor configurations (serpentine, planar and micropillered) for their performance in hydrogen generation, the reaction conditions that are optimized using the serpentine OFMR were used. The experiments were carried at flow rate of 1 mL min^{-1} and 0.5 M of Na_2SO_3/Na_2S for 2 h. The hydrogen production rates in planar, micropillared, and serpentine microreactors were 0.63, 1.56, and 2.65 μmol h^{-1} cm^{-2}, respectively. The H_2 production rate in micropillared microreactor was higher compared to that in planar due to the enhanced mass transfer in presence of the micropillars. The micropillared OFMR has 264 posts with an average area of 0.005 cm^2 and a height of 152 μm each (**Figure 4.9**). We note that each pillar acts as a CdS micropillar for hydrogen generation reaction, which enhances the mass transfer of Na_2SO_3/Na_2S causes to maximize the hydrogen evolution. The hydrogen evolution rate was higher with serpentine OFMR in comparison to that with planar and micropillared OFMR. The lower production rate in planar and micropillared microreactors may be due to the adsorption of the intermediate products onto the active sites of catalyst, which results in the reduction of the active photocatalyst surface area. Serpentine OFMR have the higher surface

to volume ratio compared to the planar and micropillared OFMR, which reduces the transportation limitations. The serpentine OFMR results in rapid-mixing, which in turn, establishes the uniform reactant concentration throughout the channel's cross-section [173]. Serpentine OFMR has the capability to confine the flow with homogeneity and sustain the steady process between hole scavenging and photo reduction of water. Thereby, higher hydrogen generation in this OFMR as compared to that in other two reactors (planar and micropillared) was obtained. The outlet stream of the optofluidic device is a clear solution indicating no leaching of photocatalyst coating from the microreactor channel walls. In the literature, there is an ambiguity in terms of the microreactor design that is suitable for the green hydrogen production directly from solar energy. The comparison of various microreactor designs is provided in Table 4.1. The enhancement of the transport properties, in turn, enhances the photocatalytic process efficiency [17]. The hydrogen production rates were also compared with those from literature reports (Table 4.2). It is worth noting that the catalysts used in the literature reported studies are different from the one used in this study. There are no literature reported studies in which CdS is used as a photocatalyst in optofluidic reactors for hydrogen production. Therefore, the comparison was made based on the available photocatalysts. The hydrogen production rate in serpentine OFMR was higher than that obtained in the present study as well as those reported in the literature. This could be attributed to its design which facilitates the rapid micromixing and mass transfer. In some cases, the panel reactors produced hydrogen with higher production rates. This could be attributed to various factors such as higher surface area, more active catalyst and reduced gas pressure (10 kPa) to remove the produced hydrogen [15,150]. In the serpentine OFMR, the H_2 production rate was 1.13 mmol h^{-1} g^{-1}, which is compared with the batch reactor data reported in literature. As can be seen from the Table, the H_2 production rate in serpentine OFMR is higher or nearly equal in most of the

cases even though the light harvesting area is small (1.05 cm^2). This indicates the higher effectiveness of the serpentine OFMR.

Table 4.1: Comparison of hydrogen production performance of optofluidic device in this study with that reported in literature.

Microreactor	Catalyst	Light source	H_2 production rate, mol h^{-1}	Irradiation area, cm^2	Reference
Planar#	Pt/TiO_2	UV	1.8×10^{-10}	--	149
Micropillared#	Pt/TiO_2	UV	1.8×10^{-8}	--	82
Planar#	Pt/TiO_2	UV	1.2×10^{-8}	--	82
Grooved#	Pt/TiO_2	UV	3.72×10^{-9}	--	83
Flat#	Pt/TiO_2	UV	1.42×10^{-9}	--	83
Panels†	$SrTiO_3$:Al with co-catalyst, RhCrOx (Rh 0.1wt%, Cr 0.1wt%)	300 W Xe lamp	680×10^{-6}	25	15
Panels	$Rh_{2-y}Cr_yO_3/(Ga_{1-x}Zn_x)(N_{1-x}O_x)$	300 W Xe lamp	117×10^{-6}	25	150
Planar large scale	Pt@mp-CN	Sunlight	7420×10^{-6}	7560	151
Serpentine	CdS	Visible light	2.78×10^{-6}	1.05	Present work

4.3 Pump energy consumption

The pump energy consumption is an important contributor to the overall cost of the process. For simplicity, we used the Hagen-Poiseuille equation (eq. 1) to calculate the pressure drop in the channel. The Hagen-Poiseuille equation is valid for straight channels and serpentine channels were used in this study. However, the order of magnitude of the pressure drop is similar in both the cases.

$$\Delta P = \frac{8Q\mu L}{\pi R^4} \ldots\ldots\ldots (1)$$

where ΔP is pressure drop

$$Flow\ rate\ (Q) = 1\ mL/\min = 0.016 \times 10^{-6} m^3\ s^{-1}$$

Viscosity (μ) = 10^{-3} Pa.s, Length (L) = 0.15 m

Width (a) = 473x10^{-6} m, Height (b) = 159 x10^{-6} m

$$\text{Hydraulic radius } R = \frac{Cross\ sectional\ Area}{Wetted\ Perimeter} = \frac{a \times b}{2 \times (a+b)} = 1.19 \times 10^{-4}$$

$$\Delta P = \frac{8 \times 0.016 \times 10^{-6} \times 10^{-3} \times 0.15}{3.14 \times (1.19 \times 10^{-4})^4} = 30.5\ kPa$$

$$Work\ (W) = \frac{\Delta P}{\rho \cap} = \frac{30.5}{1000 \times 0.6} = 50.8\ J/kg$$

$$Power = mW = \rho QW = 997 \times 0.016 \times 10^{-6} \times 50.8 = 0.81\ mW$$

A rectangular channel geometry was assumed with sides a = 473 μm and b = 159 μm and length 0.15 m. From the equation (1), the pressure drop in the microchannel was found to be 30.5 kPa. The power required to pump the fluid at 1 mL min^{-1} with a pumping efficiency of 60% is 0.81 mW. The maximum H_2 production rate in this study was 2.65 μmol h^{-1} cm^{-2}, one mole of H_2 contains 286 kJ energy and therefore the power content was 0.22 mW, which is less than the pump power consumption. The H_2 production rate required for the photocatalytic solar water-splitting process to be economically feasible is 129 μmol h^{-1} cm^{-2} and the corresponding power produced is 10.8 mW. In this case, the power required for pumping is approximately 7.6% of the power from produced H_2. Therefore, it can be mentioned that the power required for pumping is reasonably low under the economically feasible hydrogen production conditions.

4.4 Gas-liquid photocatalytic hydrogen evolution from the water in serpentine optofluidic microreactor

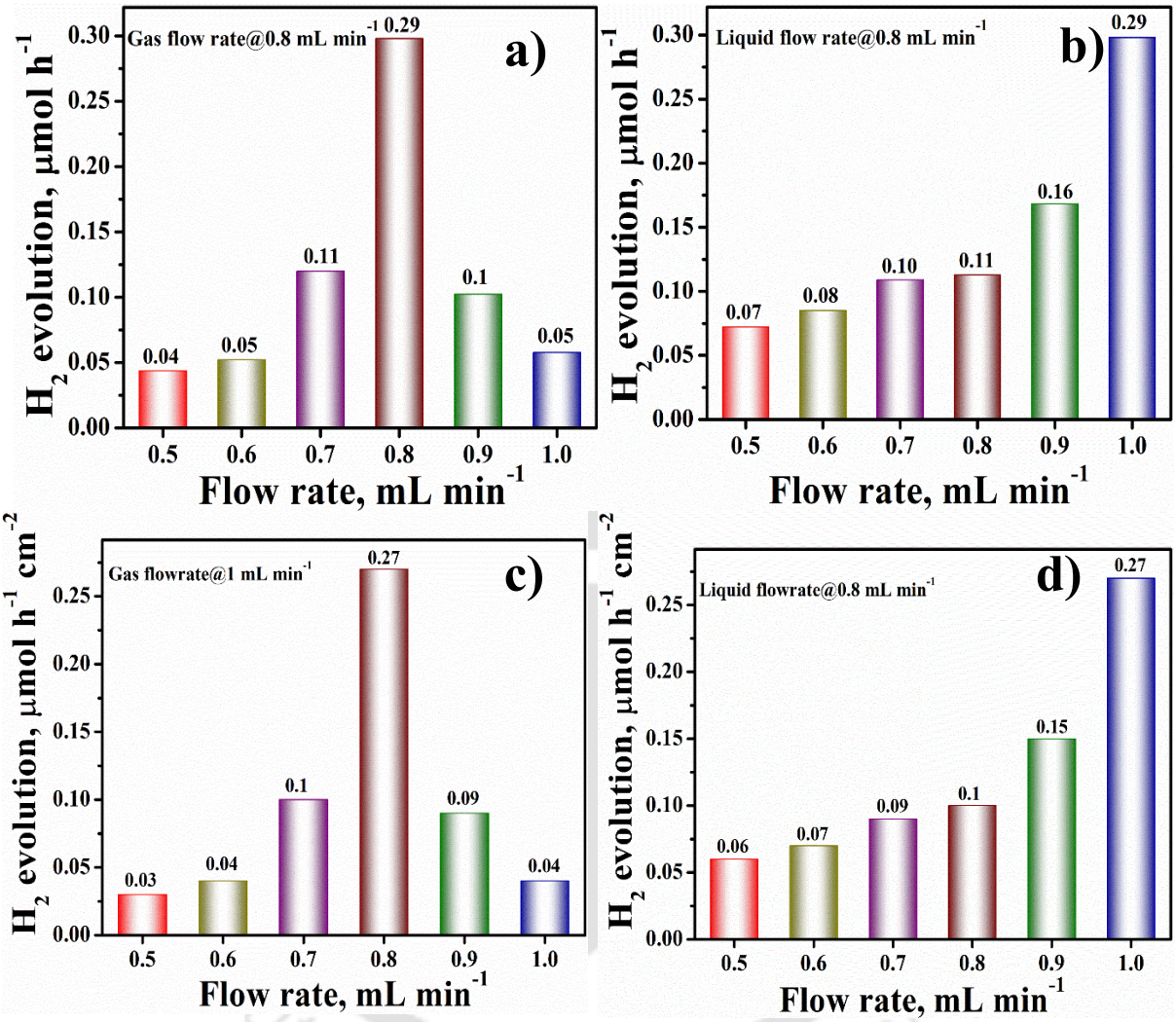

Figure 4.10: H_2 evolution rate as a function of (a and c) liquid and (b and d) gas flow rates.

inert gas (nitrogen) was introduced into the microchannel to maintain slug flow and to enhance the mixing of the reactant over the coated CdS photocatalyst and to reduce the residence time. This phenomenon favours to consume the hole within the life time of excitons resulting in the suppression of recombination. With increasing the reactant flow rates from 0.5 to 1 mL min^{-1}, the hydrogen evolution rate was first increased up to 0.8 mL min^{-1} of liquid flow rate and then decreased. A maximum HER of 0.29 µmol h^{-1} and 0.27 µmol h^{-1} cm^{-2} was obtained at a liquid flow rate of 0.8 mL min^{-1} and gas flow rate of 1 mL min^{-1} (**Figure 4.10a and c**). Replacement

of the sacrificial reagent molecules occurs by the two-phase forces over the catalyst. Mixing only in the slug beneficial to the hydrogen evolution. Usually, high mixing occurs at the interface of the two phases compared to the middle of the slug. As liquid flow rate increases slug length increases (in the range of 0.5 - 1 mL min^{-1}), so that, the mixing efficiency gradually decreases. Rapid replacement of SR molecules occurs at the interface compared to centre of the slug.

With the increase of the gas flow rate, at liquid flow rate of 0.8 mL min^{-1}, the hydrogen production rate [was] increased (Figure 4.10b and d). The maximum hydrogen production was 0.29 µmol h^{-1} and 0.27 µmol h^{-1} cm-2 at 1 mL min^{-1}. With the increase of gas flow rate (0.5 – 1 mL min^{-1}), the bubble and reactant (liquid phase) slug lengths were decreased, as shown in **Figure 4.12.** The thickness of the reactant (liquid) film and its slug length affected the photcatalytic activity in the hydrogen generation. At all the flow rates, the slug flow regime was obtained. A further increase in gas flow rate, may result in a higher hydrogen generation because of the annular flow. In this flow regime, the gas flows in the centre of the microchannel and a thin liquid film forms between microchannel wall and gas phase. And also surface area is higher in the annular flow regime compared to all the other flow regimes. From these results, it can be said that the water splitting reaction can be stimulated by gas introduction by creating

a thin film of reactant at which higher absorption of light occurs. However, the hydrogen production was low (<1 µmol h-1) due to the gas phase occupying the catalyst active area.

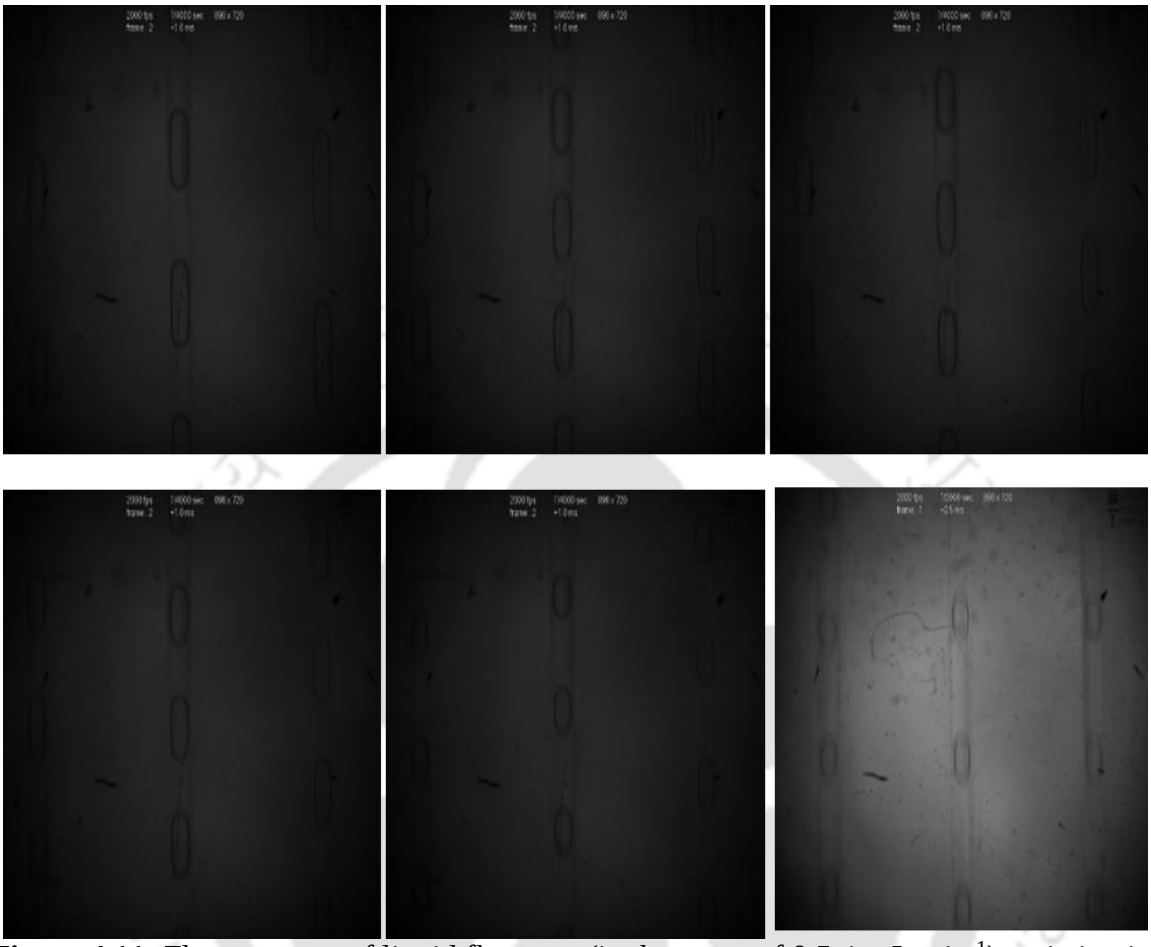

Figure 4.11: Flow patterns of liquid flow rate (in the range of 0.5-1 mL min^{-1}) variation in microchannel.

With the increase of the gas flow rate, at liquid flow rate of 0.8 mL min^{-1}, the hydrogen production rate was increased (**Figure 4.10b and d**). The maximum hydrogen production was 0.29 µmol h^{-1} and 0.27 µmol h^{-1} cm^{-2} at 1 mL min^{-1}. With the increase of gas flow rate (0.5 – 1 mL min^{-1}), the bubble and reactant (liquid phase) slug lengths were decreased, as shown in **Figure 4.12**. The thickness of the reactant (liquid) film and its slug length affected the photcatalytic activity in the hydrogen generation. At all the flow rates, the slug flow regime was obtained. A further increase in gas flow rate, may result in a higher hydrogen generation because of the annular flow. In this flow regime, the gas flows in the centre of the microchannel and a thin liquid film forms between microchannel wall and gas phase. And also surface area

is higher in the annular flow regime compared to all the other flow regimes. From these results, it can be said that the water splitting reaction can be stimulated by gas introduction by creating a thin film of reactant at which higher absorption of light occurs. However, the hydrogen production was low (<1 µmol h^{-1}) due to the gas phase occupying the catalyst active area.

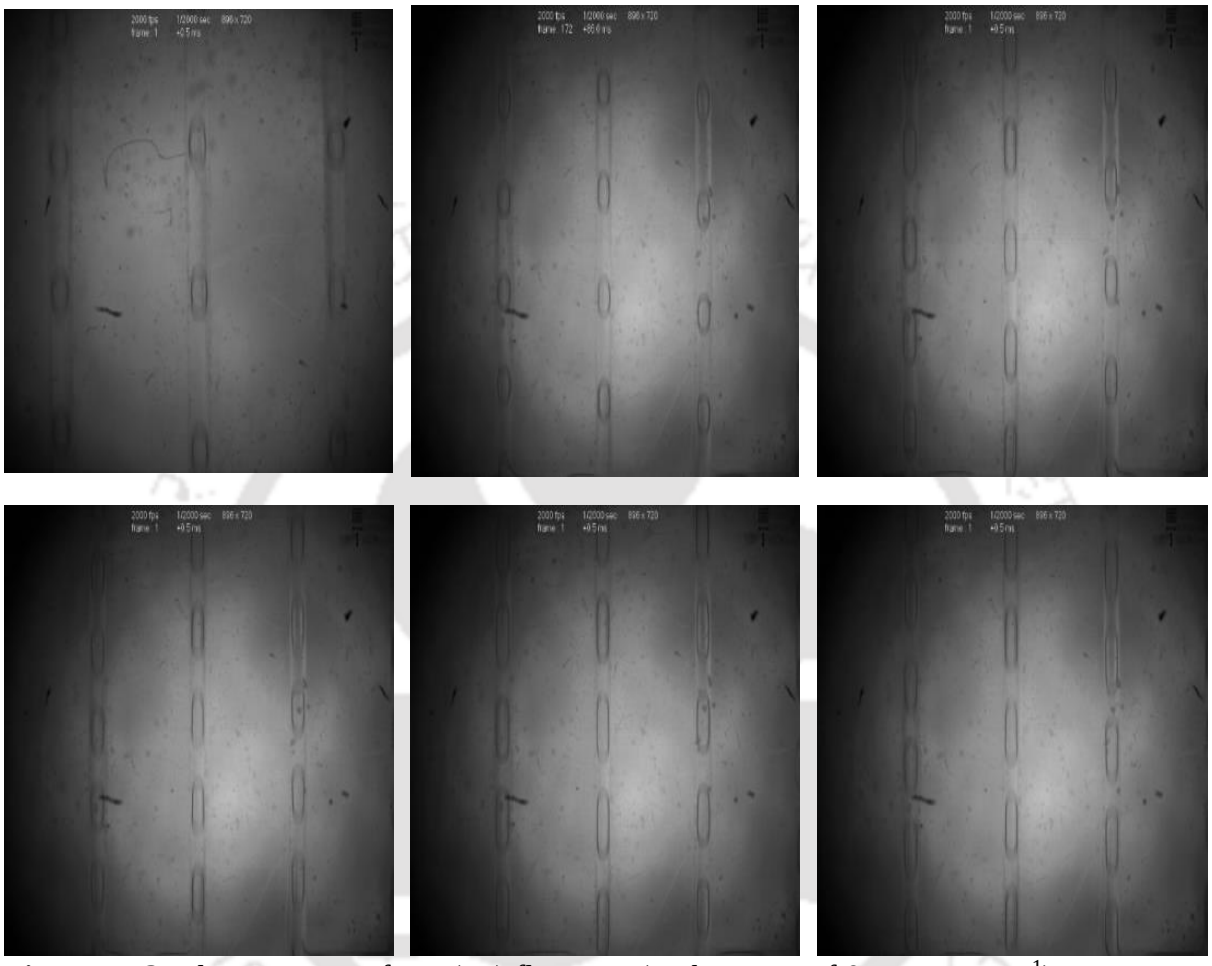

Figure 4.12: Flow patterns of gas (N_2) flow rate (in the range of 0.5-1 mL min^{-1}) variation in microchannel.

4.5 Conclusions

Three OFMRs with different geometries, such as serpentine, micropillared, and planar, were fabricated, coated with adherent CdS photocatalyst and tested for water splitting reaction to produce hydrogen. The hydrogen production rate was continuously increased with flow rate in serpentine OFMR. A maximum hydrogen production rate of 2.65 µmol h^{-1} cm^{-2} was observed at a flow rate of 1.0 mL min^{-1} in the presence of sacrificial reagent (0.5 M Na_2SO_3/Na_2S) under

visible light irradiation in serpentine OFMR. The higher hydrogen production rate obtained in the serpentine OFMR than that with other two geometries indicates that the microreactor design and shape with the higher surface-to-volume ratio are important for the efficient photo-reduction of water. While in the multiphase photocatalytic hydrogen generation, the maximum H_2 was 0.27 µmol h^{-1} cm^{-2} at liquid and gas flow rates of 0.8 and 1 mL min^{-1}. The H_2 evolution was continuously increasing with gas flow rate due to the enhanced mixing leading to enhanced mass transfer.

Chapter 5

In-situ CdS Nanowires on g-C_3N_4 Nanosheet Heterojunctions Construction in 3D-Optofluidic Microreactor for the Photocatalytic Hydrogen Generation

This chapter demonstrates the simple and cost-effective fabrication method to develop an effective corrugated serpentine OFMR (C-SOFMR) with advanced features, such as expansion/contraction and wavy microstructure. Further, the CdS nanowires on g-C3N4 nanosheet (CN/CdS) heterojunction was synthesized in situ in both P-SOFMR and C-SOFMR and utilized the device for the photocatalytic green hydrogen generation. Comparison of H_2 evolution rate in both P-SOFMR and C-SOFMR. Finally, studied flow visualization to observe the effect of flow behavior on the H_2 evolution.

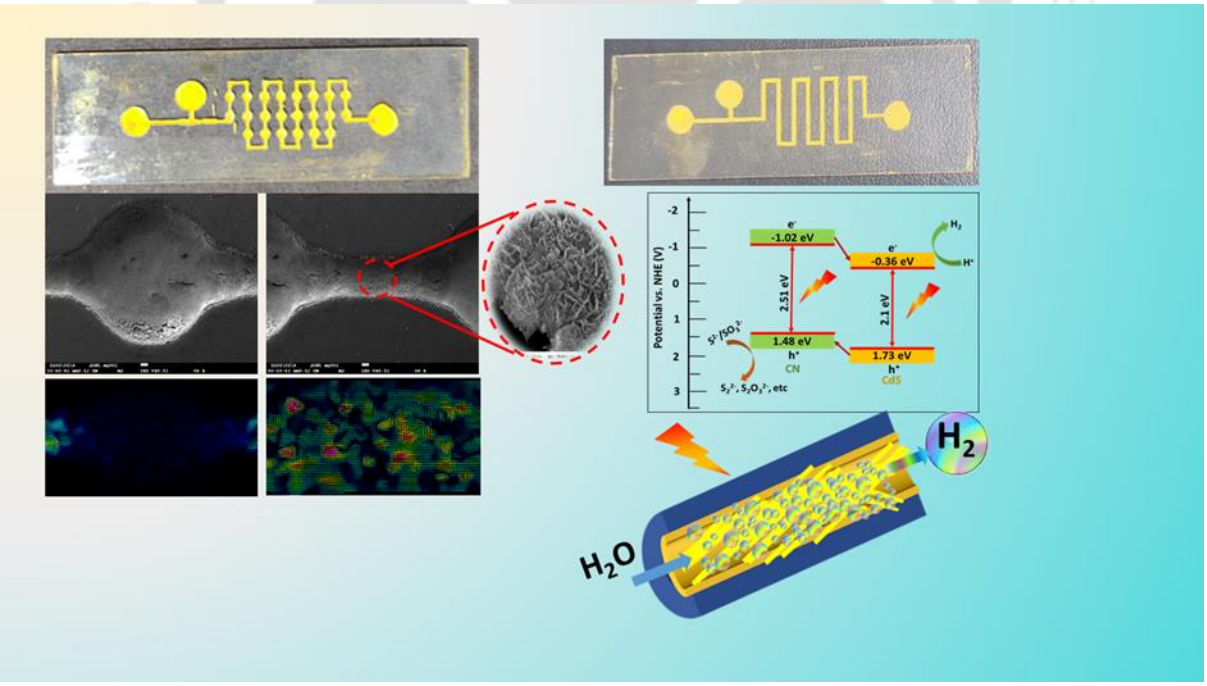

Note: This chapter is submitted to the International Journal of Hydrogen Energy.

5.1 Fabrication of C-SOFMR

Figure 5.1a shows the complete image of the fabricated C-SOFMR that was coated with CN/CdS heterojunction. **Figure 5.1b** represents the surface profile of wavy structure in the C-SOFMR. The troughs (of average depth and width of 280 and 1840 µm, respectively, **Figure 5.1b** and **c**) and crests (of average depth and width of 170 and 510 µm, respectively, **Figure 5.1b** and **d** can clearly be seen at the expansion and contraction, respectively. The CN/CdS was uniformly coated with an average thickness of about 3.5 µm (**Figure 5.2**). The microreactor shape was concave throughout the microchannel, which confines the flow significantly. The 3D flow of expansion and contraction with the wavy stream enhances the chaotic advection[174] in C-SOFMR, which in turn enhances the mixing and mass transfer.

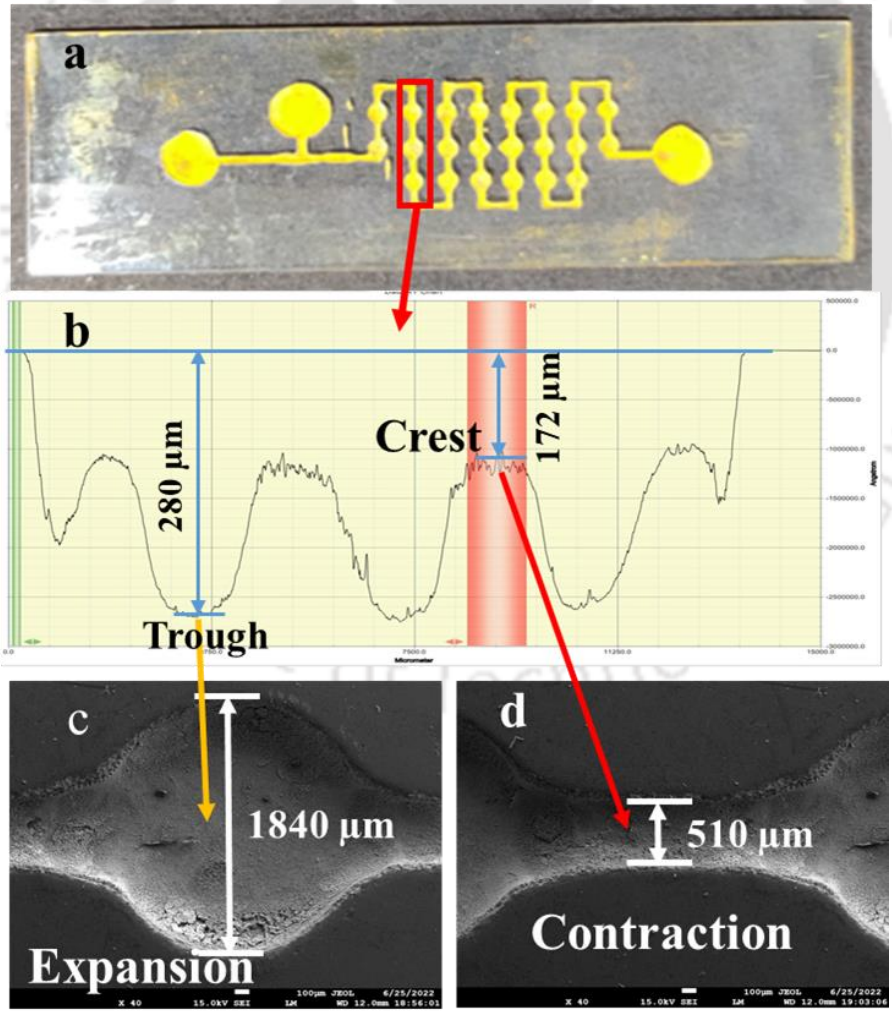

Figure 5.1: (a) CN/CdS coated M-SOFMR. (b) Surface profilometer image of the wavy structure. The FESEM images of (c) Expansion part (d) Contraction part.

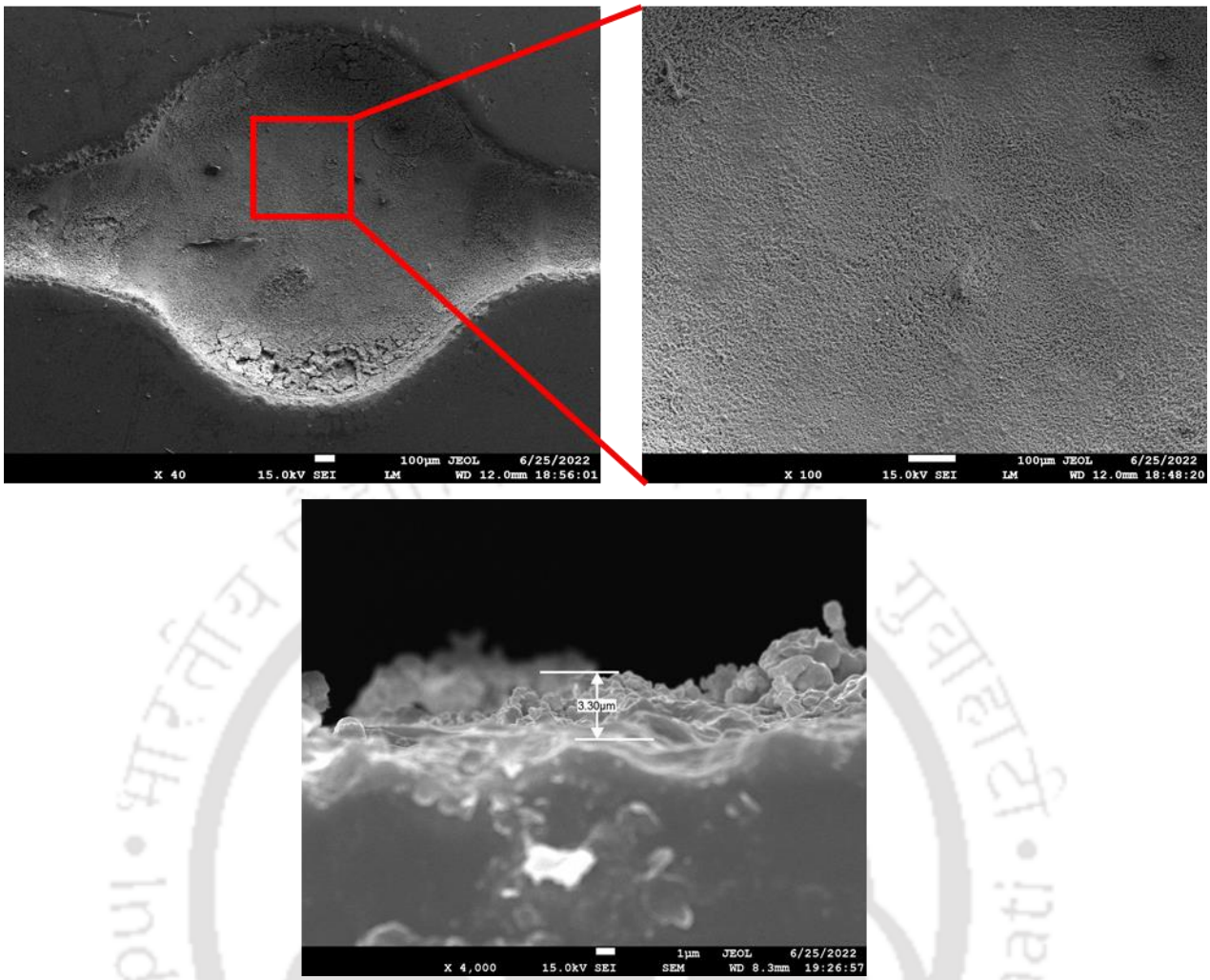

Figure 5.2: CN/CdS photocatalyst coating in C-SOFMR.

5.2 Photocatalyst Characterizations

A powder X-ray diffraction (PXRD) analysis was carried out to study the crystal phase of the synthesized CdS, g-C_3N_4, and CN/CdS heterojunction (**Figure 5.3a**). The diffraction planes of CdS[175] were at 2theeta angles 26.3 (111), 30.3 (200), 43.7 (220), 51.8 (311), and 54.2˚ (222) and those of g-C_3N_4 were at 12.81 (001), 21.6 (100), and 27.16˚ (002). The diffraction peaks of pristine CdS and g-C_3N_4 confirmed the cubic (JCPDS number 01-089-0440) and hexagonal (01-087-1526) crystal motifs of these photocatalysts, respectively. The cubic CdS structure is favourable to enhance the photocatalytic activity[176]. With the loading of CN in the CN/CdS heterojunction, the CdS intensity from all the planes was increased, which signifies that the CN

conducive to crystal growth of the synthesized CdS.[177,94,142] The 2theeta angles of the CN/CdS diffraction planes corresponding to (111), (200), and (220) were slightly shifted by 0.16, 0.36, and 0.26˚, respectively (**Figure 5.3b**). The peak shifting indicates stronger interaction of the CdS nanowires with CN nano-sheets. The peaks corresponding to CN in the CN/CdS heterojunction were not visible due to higher crystallinity of CdS and/or lower concentration of CN. The PXRD analysis ratify the formation of CN/CdS heterojunction.

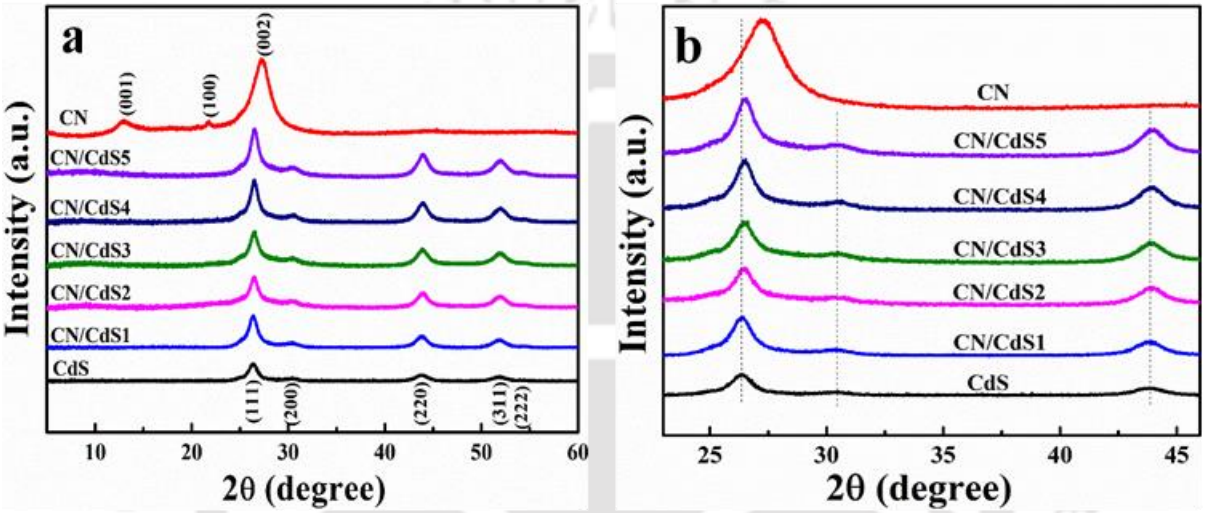

Figure 5.3: Powder X-ray diffraction (PXRD) traces (a) in the range of 2θ from 10−80° and (b) in the range of 2θ from 23−46° of the photocatalysts CdS, CN, CN/CdS1, CN/CdS2, CN/CdS3, CN/CdS4, and CN/CdS5.

The morphological features of the catalyst influence the optronic properties which in turn stimulates the photocatalytic activity. **Figure 5.4** depicts the morphology of the developed CN/CdS heterojunction. The CdS nanowires possessed an average length of 110 nm and diameter of 12.6 nm (**Figure 5.4a**). The size distribution was calculated considering 50 nanowires. The addition of polyethylene glycol and thermal treatment play a vital role in the growth of CdS nanowires on CN nanosheet with good functionalization to form heterojunction (**Figure 5.4b**). The longer CdS nanowires benefit the electronic interface with CN in the CN/CdS heterojunction and lead to the spatial separation of excitons along the CdS axial

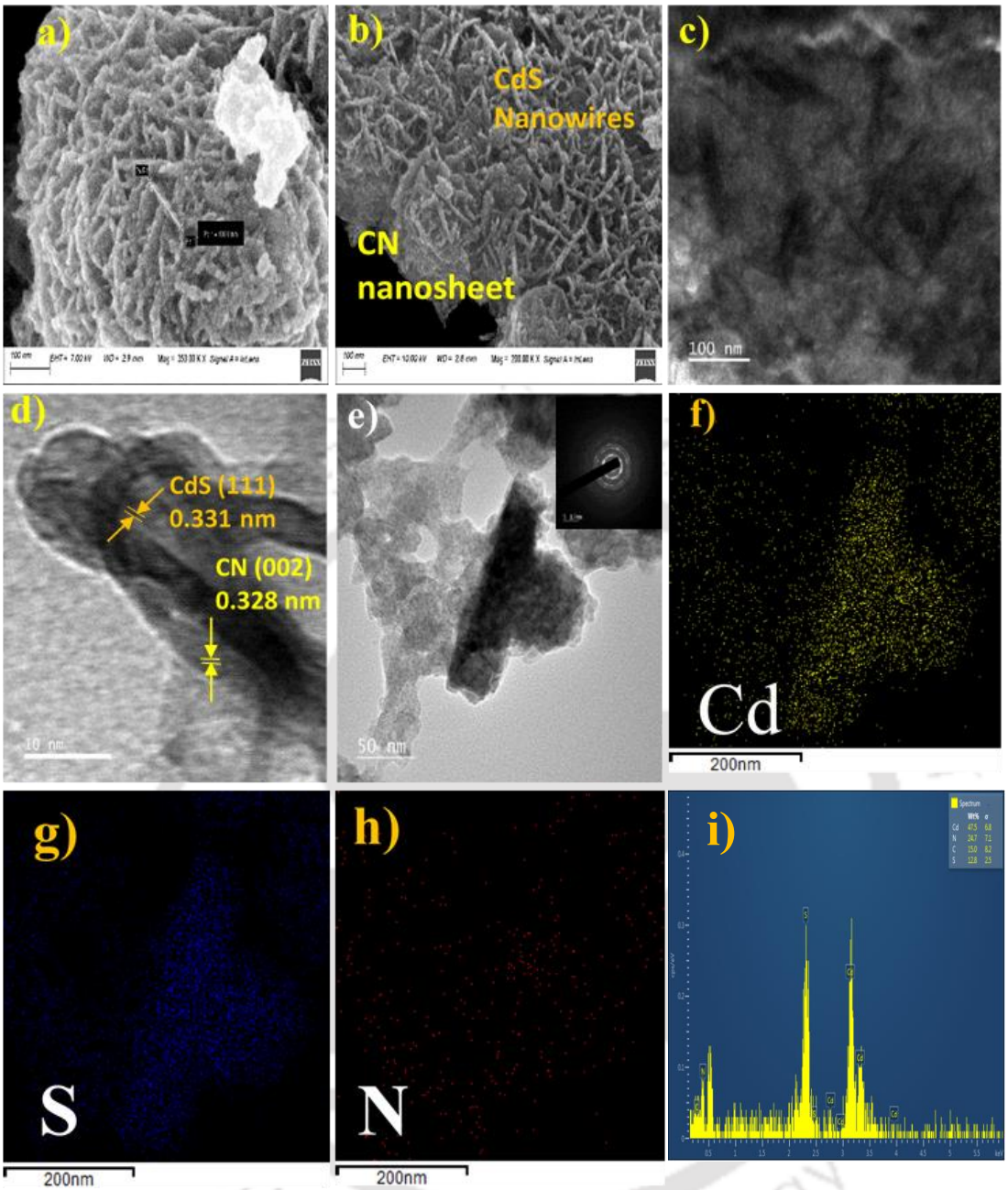

Figure 5.4: (a and b) Field emission scanning electron microscopy image of CdS and CN/CdS (c) Transmission electron microscope (TEM) image of CN/CdS (d) High resolution Field-emission transmission electron microscopic (HRTEM) image, (b) TEM image (Inset: SAED pattern), (f-h) elementary mapping of Cd, S, and N, and (i) EDX of CN/CdS.

direction.[178,12] The CdS nanowires uniformly distributed on the nanosheets of CN is a unique morphological feature of CN/CdS heterojunction which facilitates an efficient interfacial charge-carrier transfer between the CN and CdS. The TEM and HRTEM (**Figure 5.4b-e**)

images show the CN/CdS heterojunction morphology with interplanar distances of 0.331 nm and 0.328 nm, corresponding to CdS (111) and g-C_3N_4 (002) planes, respectively. The lattice fringes interlocking shows the formation of CN/CdS heterojunction. The STEM-EDS elemental mapping shows the elemental distribution and composition of Cd, S, C, and N in CN/CdS heterojunction. The mapping of Cd, S, and N elements are shown in **Figure 5.4f-h**, respectively. From the EDX results, the corresponding percentage of Cd, S, C, and N were 47.5, 12.8, 15.0, and 24.7 wt% and the catalyst weight ratio of CN/CdS was 0.65 w/w (**Figure 5.4i)**. The STEM-EDS reveals the well-organized hetero-structure of the fabricated CN/CdS heterojunction. The FTIR spectra of synthesised CdS, CN, and CN/CdSx are shown in **Figure 5.5a**. The pristine CdS peaks obtained at 605 and 1088 cm^{-1} correspond to the tensile vibrations of Cd-S[167]. The characteristic peaks of CN from 1240 to 1620 cm^{-1} ascribed to the stretching vibrations of C-N and C=N. The peak at 804 cm^{-1} attributed to the s-triazine ring[116,148]. The peaks of CN and CdS were existed in the CN/CdS, which confirmed the formation of CN/CdS hybrid structure. Further, the Raman spectra was examined to confirm the CN/CdS heterojunction formation as shown in **Figure 5.5b**. For the pristine CdS, the prominent peaks at 302 and 606 cm^{-1} were referred to the longitudinal optical (1LO) phonon and overtone optical (2LO) phonon, respectively. The CN peaks were not appeared due to the low content, well matched with the XRD results[179].

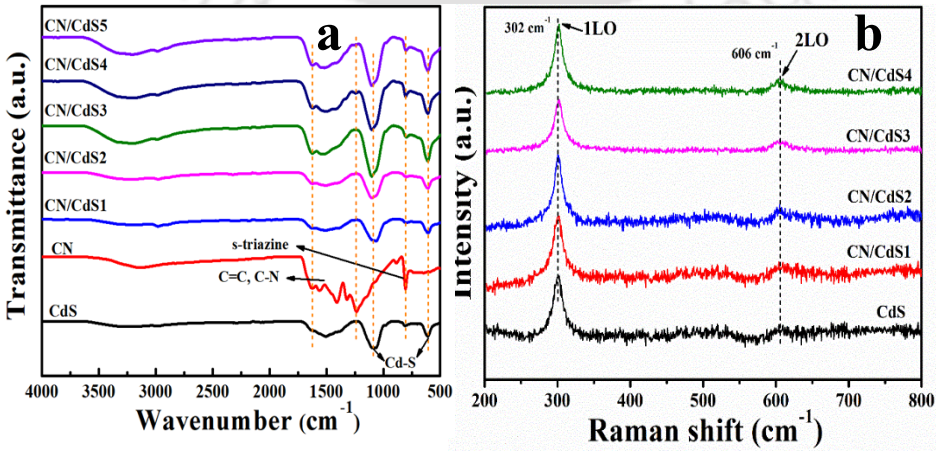

Figure 5.5: FT-IR (a) and Raman (b) spectra of synthesized CdS, CN, and CN/CdSx (from bottom to top).

The UV-visible spectra were investigated for the optical properties and for the measurement of bandgap of the synthesized photocatalysts (**Figure 5.6a** and **b**). The optical absorbance edges of the CdS, CN, and CN/CdS2 were confined at 556, 456, and 564 nm. The electronic bandgap values of CdS, CN, and CN/CdS2, as calculated from the Kubelka−Munk function using the Tauc plot, were 2.1, 2.51, and 2.01 eV, respectively. With the loading of CN, the optical absorption of CN/CdS2 was red shifted. This can be due to the photosensitization effect of CN and the heterostructure formation that contributes to the higher exciton generation and efficient interfacial transfer. The superior transport properties in SOFMRs facilitate the rapid exciton scavenging. The valence band (VB) and conduction band (CB) edge potentials of the synthesized CdS, CN, and CN/CdS2 photocatalysts were calculated at normal hydrogen potential using the following equations.

$$E_{CB} = \chi - E^e - \frac{1}{2}E_g$$

$$E_{VB} = E_{CB} + E_g$$

where E_g is band gap of semiconductor, E_{CB} is CB edge potential, E_{VB} is VB edge potential, E^e is the energy of free electrons on the hydrogen scale (~ 4.5 eV). The χ is the absolute electronegativity of the semiconductor, expressed as the geometric mean of the absolute electronegativities of the constituent atoms, which in turn are defined as the arithmetic mean of the atomic electron affinity and the first ionization energy. The values of χ for CdS and CN are 5.19 and 4.73, respectively[180,181,182,183,184]. The VB and CB edge potentials were estimated to be 1.73 and -0.36 eV for CdS and 1.48 and -1.02 eV for CN, respectively. The CB of CN was more negative than the CB of CdS and the VB of CdS was more positive than the VB of

CN. Therefore, the electrons migrate from CB of CN to CB of CdS and the holes migrate from VB of CdS to VB of CN under the light irradiation (**for** CdS and CN**c**)[147].

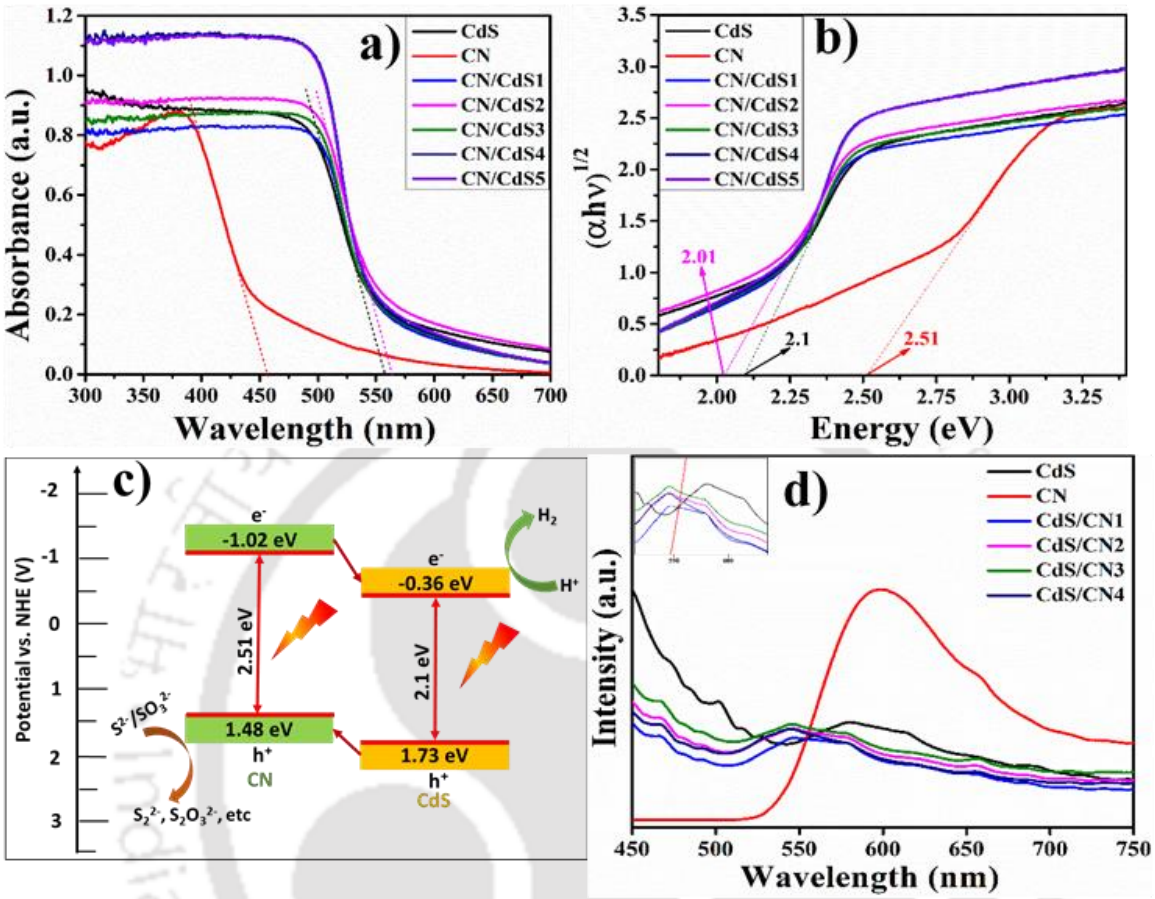

Figure 5.6: (a) UV-Visble spectra, (b) Tauc plot (α, h, and ν are the optical absorption coefficient, Planck's constant, and photonic frequency), (c) Excitons mobility, and (d) PL spectra of CdS, CN, and CN/CdS (Inset: high resolution PL spectra).

The strong PL from pristine CdS at 580 nm (2.13 eV) and from pristine CN at 597 nm (2.07 eV) indicate the strong radiative recombination of charges from these photocatalysts (**Figure 5.6d**). For the CN/CdS2 heterojunction, the PL peak of CN centred at 597 nm (2.07 eV) was disappeared. This indicates that the reduced recombination of charges in CN/CdS heterojunction which in turn can be ascribed to the strong interaction of CN with CdS. The CdS peak (580 nm) in CN/CdS was blue shifted to 546 nm (2.27 eV) which can be attributed

to the recombination of the transferred electrons from CN to CdS and excited electrons from the CdS with the holes in CdS.[181,185,146,186]

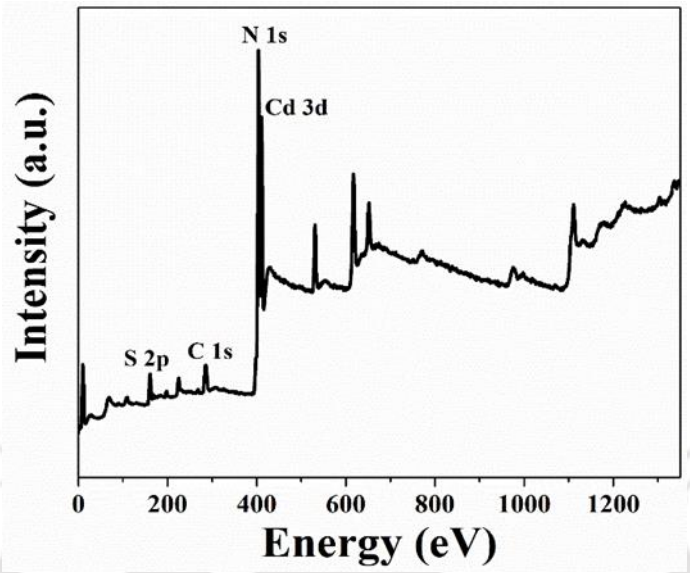

Figure 5.7: XPS survey plot of the CN/CdS heterojunction.

The survey plot shows the presence of Cd, S, C and N (**Error! Reference source not found.**). The surface composition and the chemical states of CdS, CN, and CN/CdS heterojunction were examined using XPS (**Error! Reference source not found.**). The high resolution Cd 3d spectra of pristine CdS and CN/CdS were deconvoluted and the peaks at binding energies 405.45 and 412.22 eV were assigned to the Cd $3d_{5/2}$ and Cd $3d_{3/2}$[187,146,188]. The binding energies of Cd $3d_{5/2}$ and Cd $3d_{3/2}$ of CN/CdS heterostructure were red-shifted in comparison to those of CdS by approximately 0.25 and 0.29 eV, respectively (Error! Reference source not found.**a**). The high resolution S 2p spectra were deconvoluted and the peaks corresponding to S $2p_{3/2}$ and S $2p_{1/2}$ of S^{2-} in the CdS were observed at 161.32 and 162.46 eV, respectively, and that corresponding to S atoms on CdS edge or S $2p_{1/2}$[187] was observed at 168.95 eV. [146,188] The XPS peak corresponding to S atoms on CdS edge was red-shifted (0.26 eV) in the CN/CdS heterojunction (Error! Reference source not found.**b**). The negative shift of peaks corresponding to Cd 3d and S 2p states of the CN/CdS indicates that the CdS is in reduced state.[126] The high-resolution C 1s spectra of CN and CN/CdS, exhibits binding energy peaks at 284.62, 285.98, and 2 88.08

which can be assigned to the sp^2 bonded C species (C-C/C=C), C-NH on heptazine edge, and sp^2 bonded C in tri-s-triazine ring ($N=C(-N)_2$), respectively (Error! Reference source not found.**c**).[189,116,147] The N 1s signals at 399.82, 401.34, and 404.89 eV correspond to the sp^2 hybridized N bonded in s-triazine (C-N=C), sp^3 tertiary N bonded with carbon ($N-(C)_3$), amino groups (N-H), and terminal nitrate groups and π-excitations or charging effects in CN, respectively[189,116,147] (Error! Reference source not found.**d**). In the CN/CdS, the intensity of C 1s peaks at binding energies 284.62 and 285.98 eV was decreased and N 1s peaks at 399.82 and 401.34 eV were disappeared completely due to the heterojunction formation between the CdS and CN. The high resolution XPS N 1s peak intensities of CN/CdS2 sample at binding energies 398.79 and 405.5 eV showed an opposite trend as compared to those of pristine CN sample. That is, the peak intensities were lower at 398.79 eV and higher at 405.5 eV for CN/CdS2 sample while they are higher at 398.79 eV and lower at 405.5 eV for CN sample. This could be attributed to the conjugate formation of CdS with the CN s-triazine rings[190,191]. The positive shift of C 1s and N 1s in CN/CdS2 was due to the extracted electron density. This

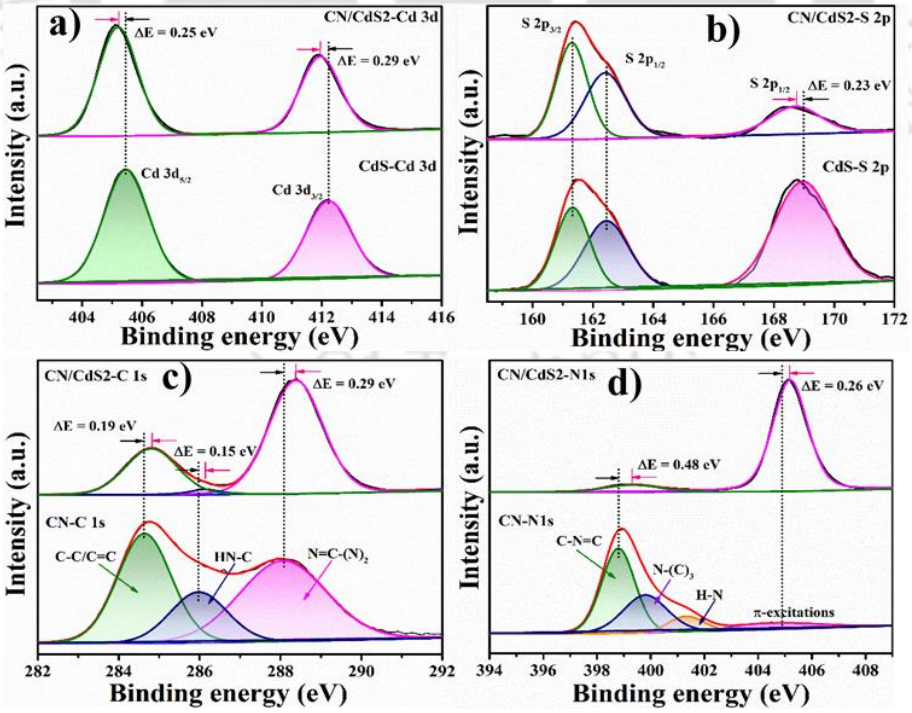

can be ascribed to the electron transfer from the CN to CdS that occurs due to the strong electronic interaction between CdS and CN in the CN/CdS2 **Figure 5.8:** X-ray photoelectron

spectroscopy (XPS) analysis of CdS, CN and CN/CdS2: (a) Cd 3d; (b) S 2p; (c) C 1s; and (d) N 1s.

heterojunction.[34,94] The XPS binding energy peak shifting in CN/CdS indicates successful formation of the CN/CdS heterojunction.

5.3 Photocatalytic activity test

The SOFMRs with high surface to volume ratio reduces the transport resistances. The heterostructured catalyst thin film enables the instantaneous exciton transfer, which enhances the photocatalytic activity.

The sacrificial reagent (SR) prevents the back reaction as well as photocorrosion by scavenging the holes from the photocatalyst's VB. The short radial diffusion length in SOFMRs facilitates the uniform mixing and narrow residence time distribution, which in turn prevents the unwanted reactions. Continuous flow of SR to the SOFMRs sustains the catalyst activity and HER rate. The HER rates in P-SOFMR obtained with the sacrificial reagents 10% lactic acid, 10% triethanolamine, and 0.5 M Na_2SO_3/Na_2S were 0.69, 1.82, and 4.24 µmol h^{-1}, respectively (**Figure 5.9a**). The photocatalytic activity was the highest in the presence of 0.5 M Na_2SO_3/Na_2S. The higher efficiency of the sacrificial reagent SO_3^{2-}/S^{2-} was due to its favourable kinetics for oxidation by holes in CN/CdS valence band.[176,192,86] The photostability

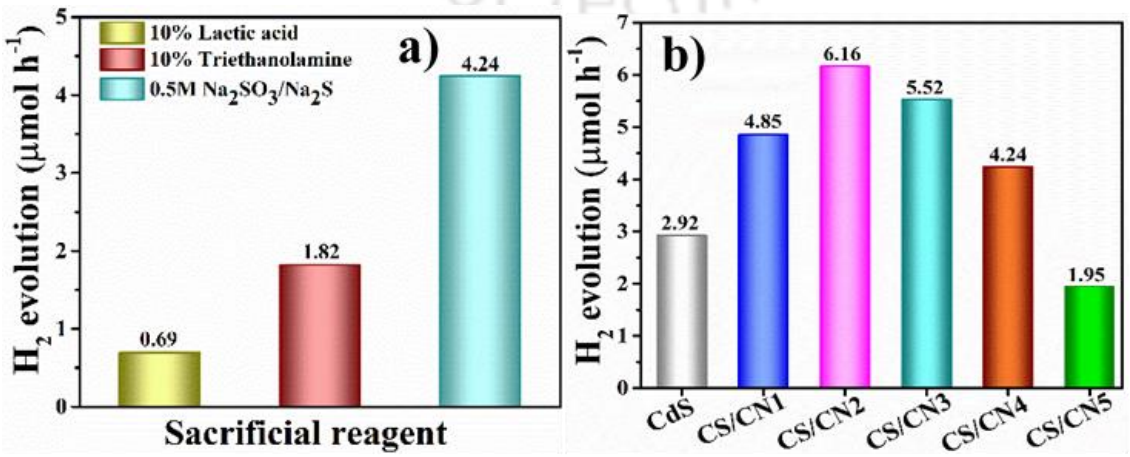

of CdS based photocatalysts is also higher in the presence of Na_2SO_3/Na_2S as a sacrificial reagent[116].

Figure 5.9: Hydrogen production rate as a function of (a) type of sacrificial reagent and (b) CN loading in CN/CdS heterojunction.

The photocatalytic activity of CdS and CN/CdS heterojunction was examined for the hydrogen evolution reaction (HER) in P-SOFMR, using 0.5 M Na_2SO_3/Na_2S as a hole scavenger at a reactant flowrate of 1 mL min^{-1}, under the visible light irradiation. **Figure 5.9b** illustrates the HER rate as a function of CN loading in the CN/CdS heterojunction. The HER rate was lower (2.92 µmol h^{-1}) with CdS photocatalyst. It was first increased and then decreased with the increase of CN wt% in the CN/CdS heterojunction, passing through maximum at 0.17 wt% of CN. At CN loadings of 0.009, 0.17, 0.44, 4.46 and 9.6 wt%, the HER rates were 4.85, 6.16, 5.52, 4.24, and 1.95 µmol h^{-1}, respectively. The CN/CdS2 heterojunction exhibited the best

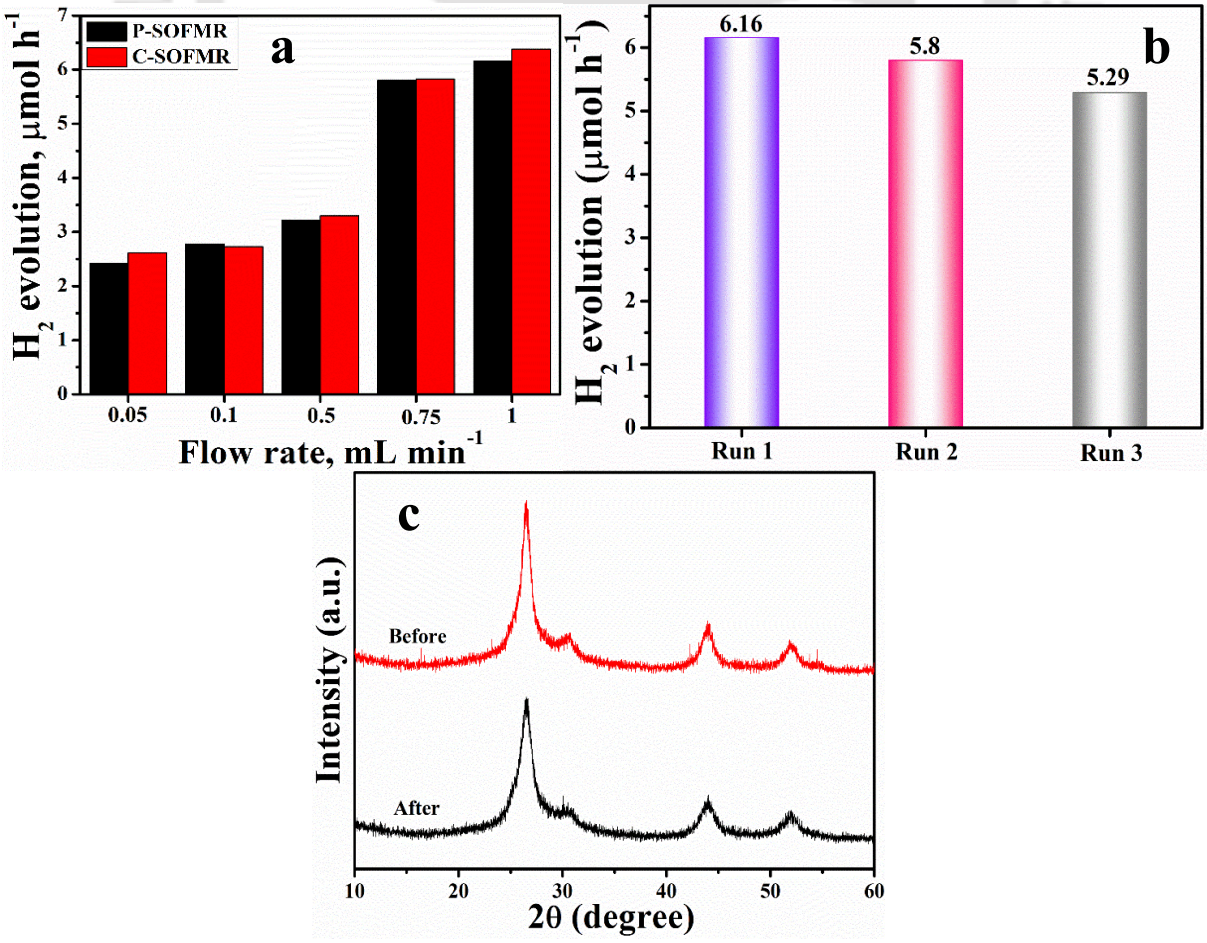

photocatalytic activity (6.16 µmol h^{-1}). The higher HER rate observed over the CN/CdS2 heterojunction was due to the narrow bandgap, higher charge mobility and suppressed

Figure 5.10: (a) Comparison of H_2 production in OFMRs against the flowrate. (b) Stability test of the CN/CdS2 for photocatalytic hydrogen evolution in P-SOFMR; and (c) Powder X-ray diffraction (PXRD) traces of CN/CdS2 before (Red) and after (Black) the reaction. recombination, as revealed from the XPS and PL analyses. Beyond 0.17 wt. % of CN loading, the photocatalytic activity of CN/CdS was decreased due to the coverage of CdS photocatalytic active sites with CN layer. This lowers the overall light absorption by the CdS, in line with the UV-Vis analysis.

Figure 5.10a demonstrates the comparison of HER rate in P-SOFMR and C-SOFMR as a function of the flow rate. The HER rate increased from 2.42 to 6.16 µmol h^{-1} in P-SOFMR and 2.61 to 6.38 µmol h^{-1} in C-SOFMR with the increase of flow rate from 0.05 to 1.0 mL min^{-1}. The HER at 1 mL min^{-1} flowrate was 2.54 and 2.44 times higher than that at 0.05 mL min^{-1} in P-SOFMR and C-SOFMR, respectively. With increasing the flow rate, the mixing length reduces due to the improved chaotic advection[193] leading to radial mixing in P-SOFMR and recirculated flow in C-SOFMR which in turn results in homogeneous 0.5 M Na_2SO_3/Na_2S concentration along the length of the optofluidic device. This improves the transport of sacrificial reagent (Na_2SO_3/Na_2S) molecules to the photocatalyst active sites,[194] which in turn boosts hole-scavenging. Enhanced mass transfer and short residence time in SOFMRs favour the suppression of surface recombination and reduces the photocorrosion[44]. **Figure 5.10b** depicts the stability of the CN/CdS2 heterojunction for the photocatalytic hydrogen evolution. The 3 recycle tests were carried out in P-SOFMR at a reactant flow rate of 1 mL min^{-1} for 2 h run. The H_2 evolution rate was marginally decreased with number of cycles, which might be due to the photocatalyst leaching from the P-SOFMR. The XRD traces of the CN/CdS2 before and after the photocatalytic hydrogen evolution reaction is shown in **Figure 5.10c**. After the

photoreaction, no change in the XRD peak intensity and position was observed in comparison to its fresh counterpart. This indicates no changes in the crystal structure of the photocatalyst CN/CdS2 heterojunction during the photocatalytic reaction[195,196,197,198,199].

5.4 Hydrodynamic study

Figure 5.11 represents the flow visualization in SOFMRs. **Figure 5.12a** demsonstrates fluid flow visualization in the C-SOFMR. At contraction, stretching and folding of fluid was

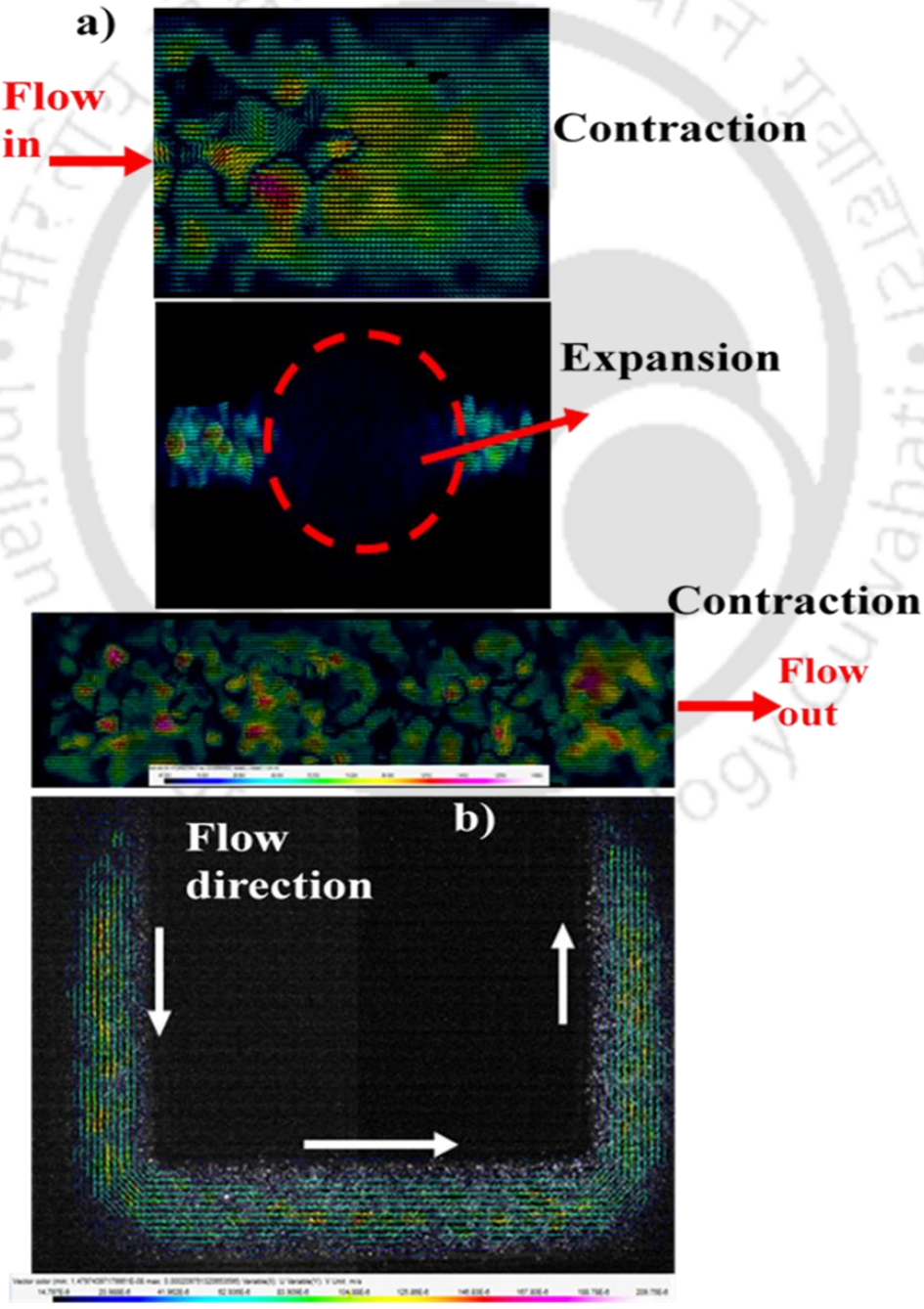

observed, owing to the chaotic advection.[193] At the expansion with trough, flow expansion with the lower velocity magnitude was observed. The higher chaotic advection or back mixing at the contraction was due to the lower cross-sectional area. This phenomenon leads to higher interfacial area and the short diffusion length,[200] resulting in rapid mixing and mass transfer[201]. However, the residence time increases due to the back mixing. Thus the intermediates and reactant molecules block photons from reaching the photocatalyst.[202] Moreover, the light scattering due to the high vorticity may result in photon energy loss. In the case of overall water splitting, back reactions may occur due to the back mixing. **Figure 5.14b** depicts the fluid flow visualization in the P-SOFMR. The flow followed a parabolic velocity profile (i.e., the velocity was higher at middle and lower at the wall) attributed to the laminar flow. Neither vortices nor back mixing was observed. Forward fluid streams in P-SOFMR reduces the photon energy loss, residence time and effect of intermediates on the photocatalytic activity as mentioned above. Further study is required to assess the full potential of the C-SOFMR. Studies are on going in our lab on various OFMR designs such as induced swirling flow with radial mixing and without back mixing for the enhanced green hydrogen production.

Figure 5.13: Velocity vector field in (a) C-SOFMR (b) P-SOFMR (frame rate 40 fps).

The hydrogen production rates over various photocatalysts in the OFMRs reported in the literature are presented in our previous publication[44]. To the best of our knowledge, this is the first report on the photocatalytic hydrogen evolution over the CN/CdS heterojunction in the OFMR. The photocatalytic activity of the CN/CdS heterojunction with P-SOFMR and C-SOFMR were compared with those reported with batch photoreactor (particulate photocatalyst) in the literature (Table 5.1). Compared to the literature reports, the apparent quantum yield (29 %) was higher in the present study, which can be ascribed to the uniform light harvesting and enhanced transport properties in the integrated CN/CdS film SOFMRs.

218 **Table 5.1:** The comparison of the present hydrogen evolution rate over the CN/CdS

219 heterojunction with the literature.

Light source	Loading (mg)	SR	H_2 (μmol h^{-1})	A.Q.E. (%)	Irradiation Area (cm^2)	References
300 W Xe lamp	50	Triethanolamine	14.83	--	18.57	[132]
400 W Xe lamp	25	0.02 M Na_2SO_3 and 0.1 M Na_2S	0.46	--	19.6	[203]
300 W Xe lamp	50	0.5 M Na_2SO_3/Na_2S	11.75	--	--	[204]
300 W Xe lamp	10	Na_2SO_3/Na_2S	21.2	--	--	[196]
PLS-SXE 300D Xe lamp	50	Triethanolamine	11.76	9.6	--	[142]
300 W Xe lamp	50	0.35 M Na_2S and 0.25 M Na_2SO_3	46	4.4	--	[145]
300 W Xe lamp	5	0.25 M Na_2S/Na_2SO_3	0.76	6.86		[146]
400 W metal halide lamp		0.5 M Na_2S/Na_2SO_3	6.16 (P-SOFMR) 6.38 (C-SOFMR)	29.56 13.68	1.05 2.34	Present work

220

5.5 Photocatalytic mechanism

Based on the photocatalytic activity test results, a photocatalytic reaction mechanism is proposed for the synthesized CN/CdS heterojunction and is shown in Fig. 11. Under the visible light irradiation, CdS and CN excited to produce the electrons and holes, respectively. The excited electrons from the conduction band (CB) of CN are transferred to the CB of CdS because the CB potential of CN is more negative than that of the CdS. The holes from the valance band (VB) of CdS are migrated to the VB of CN due to more positive VB potential of CdS than that of the CN. The excitons mobility and spatial separation indicate Type II heterojunction formation between CdS and CN, which reduces the excitons recombination effectively. The holes in the CN VB scavenged by the SR (0.5 M Na_2SO_3/Na_2S). Meanwhile, the electrons in the CdS CB reduce water to hydrogen. The CdS and CN act as reduction and oxidation sites, respectively, for the redox reactions.

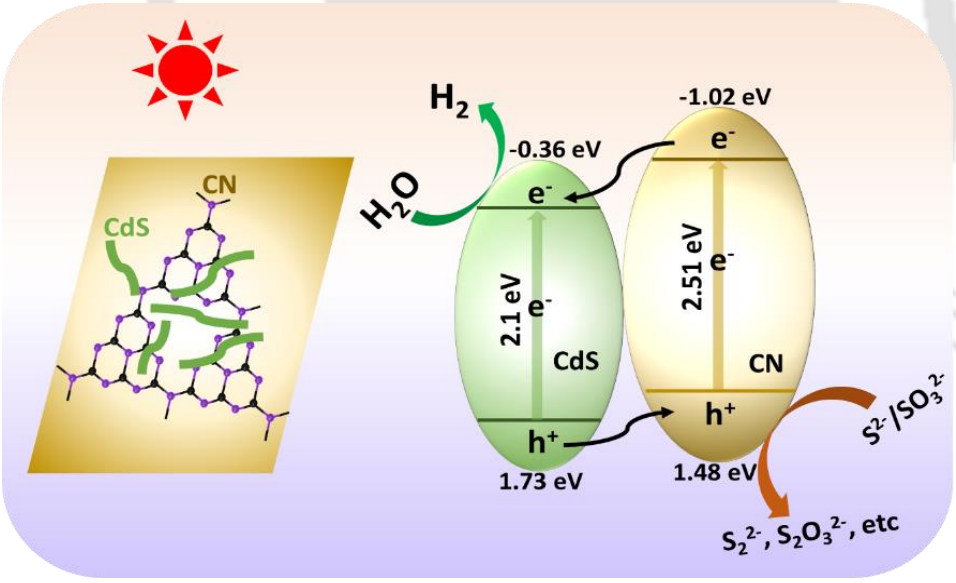

Fig. 11: Photocatalytic mechanism in the synthesized CN/CdS heterojunction.

5.6. Conclusions

A simple and cost-effective SOFMRs possessing the expansion/contraction and the wavy microstructured configuration were constructed successfully with in situ synthesized CdS nanowires on g-C_3N_4 nanosheet (CN/CdS) heterojunction. The charge generation and transport

are more efficient with CN/CdS heterojunction as compared to those with CdS alone. The CN/CdS heterojunction showed the highest photocatalytic activity (6.38 µmol h^{-1} in C-SOFMR and 6.16 µmol h^{-1} in P-SOFMR at 1.0 mL min^{-1}) in photocatalytic green hydrogen production from water-splitting, due to its good optronic properties. The higher flow rates (1 mL min^{-1}) favored the rapid scavenging of the holes and the free electrons are effectively utilized for the water-splitting reaction to produce hydrogen.

Chapter 6

Thesis Conclusions and Reccomendations of Future Scope Work

This chapter briefs the major findings and outcomes of this thesis. It also mentions the limitations and future scope to enhance the photocatalytic hydrogen evolution in continuous flow microreactor.

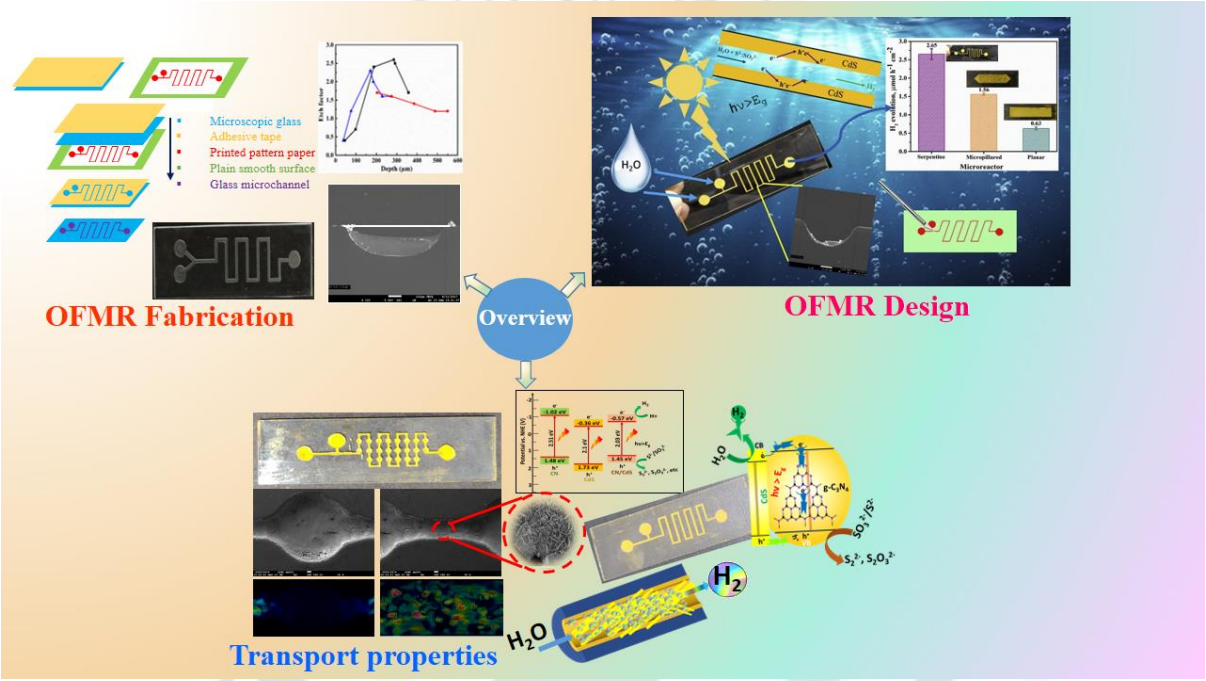

6.1 Major findings

i. **Adhesive tape based glass microreactor fabrication:** A simple, rapid, robust, and cost-effective glass microfabrication method was successfully developed which overcomes the critical issues associated with photoresist masks, such as adherence. Moreover, deeper microchannels with sharp edges and without wall-irregularities were obtained.

ii. A higher depth of 550 µm, with an etch factor of 1.2, was obtained for an optimal etchant concentration of 49% and etching time of 120 min.

iii. Using the developed method, various microchannel shapes were successfully fabricated, proving the robustness of the method. The adhesive tape-based fabrication method, developed in this study, could enable achieving versatile microfluidic channels on glass at lower cost.

iv. The significance of adhesive tape extends in microfabrication because of its adhesive nature to bond, flexibility in employing, optical transparency (beneficial for photonics), rapid, and cheaper to use.

v. **OFMR for the H_2 evolultion over CdS:** The OFMRs with various geometries, such as serpentine, micropillared, and planar were successfully fabricated, coated with adherent CdS photocatalyst and tested for water splitting reaction to produce hydrogen.

vi. A maximum hydrogen production rate of 2.65 µmol h^{-1} cm^{-2} was observed at a reactant flow rate of 1.0 mL min^{-1} in the presence of sacrificial reagent (0.5 M Na_2SO_3/Na_2S) under visible light irradiation in serpentine OFMR. The higher hydrogen production rate obtained in the serpentine OFMR than that with other two geometries indicates that the OFMRs with higher surface-to-volume ratio are more efficient for the photocatalytic water-splitting to produce hydrogen.

vii. The higher hydrogen production rate obtained in the serpentine OFMR than that with other two geometries indicates that the OFMRs with higher surface-to-volume ratio and effective hydrodynamics are more efficient for the photocatalytic water-splitting to produce hydrogen.

viii. **Induced CN/CdS Heterojunction 3D-Optofluidic Microreactor for the H_2 evolution:** The corrugated (C-SOFMR) and plain (P-SOFMR) serpentine OFMRs, with the expansion/ contraction and the wavy microstructured configuration, were successfully fabricated and tested for the photocatalytic hydrogen production.

ix. The CdS nanowires on g-C_3N_4 nanosheet (CN/CdS) heterojunction thin film successfully synthesized *in situ* P-SOFMR and C-SOFMR.

x. The charge carriers generated were utilized efficiently for the HER reaction in both P-SOFMR and C-SOFMR at higher flow rates attributing to the rapid micromixing and mass transfer.

xi. The CN/CdS heterojunction showed the highest photocatalytic activity (6.38 µmol h^{-1} in C-SOFMR and 6.16 µmol h^{-1} in P-SOFMR at 1.0 mL min^{-1}) due to its good optronic properties.

xii. The flow behaviour in C-SOFMR and P-SOFMR was studied using flow visualization method and correlated it with the photocatalytic hydrogen production in these devices. The flow visualization study reveals a laminar flow with no back mixing in plain serpentine OFMR (P-SOFMR), and stretching and folding of fluid along with back mixing in C-SOFMR.

xiii. The synergistic effect of optofluidic microreactor (OFMR) coated with the thin film of nano-structured semiconductor heterojunction is believed to improve the photocatalytic

activity by the enhanced charge separation, transfer, and utilization with the confined flow dynamics at micro-scale.

6.2 Limitations of the thesis

i. Exploration of noble metals doping may enhance the H_2 evolution reaction.

ii. Overall water splitting reaction to produce H_2 and O_2 under the visible light irradiation could not be established.

6.3 Future work directions

i. Pattern developing machine may be used for the adhesive tape-based glass fabrication to increase the speed and reduce the time of fabrication.

ii. In-depth studies are required for the gas-liquid multiphase photocatalytic water-splitting reaction to produce hydrogen with lower mass-transfer limitations.

iii. Molecular level simulations are required to understand the interaction of excitons and reactants in the OFMRs.

iv. C-SOFMR could be used to explore the other potential applications such as biosensors, gas-liquid reactions, and organic synthesis.

v. Scale up of micro processing technology for the energy conversion and utilization.

References

(1) Grayson, M. Energy Transitions. *N A T U R E* **2017**, *551* (7682), 7682.

(2) Hanley, E. S.; Deane, J. P.; Gallachóir, B. P. Ó. The Role of Hydrogen in Low Carbon Energy Futures–A Review of Existing Perspectives. *Renew. Sustain. Energy Rev.* **2018**, *82* (January 2017), 3027–3045. https://doi.org/10.1016/j.rser.2017.10.034.

(3) Schiermeier, Q.; Tollefson, J.; Scully, T.; Witze, A.; Morton, O. Energy Alternatives: Electricity without Carbon. *Nature* **2008**, *454* (7206), 816–823. https://doi.org/10.1038/454816a.

(4) York, R. Do Alternative Energy Sources Displace Fossil Fuels? *Nat. Clim. Chang.* **2012**, *2* (6), 441–443. https://doi.org/10.1038/nclimate1451.

(5) Thomas, M. S. D. and I. L. Alternative Energy Technologies. *Nature* **2016**, *414* (November), 1463–1468.

(6) Staffell, I.; Scamman, D.; Velazquez Abad, A.; Balcombe, P.; Dodds, P. E.; Ekins, P.; Shah, N.; Ward, K. R. The Role of Hydrogen and Fuel Cells in the Global Energy System. *Energy Environ. Sci.* **2019**, *12* (2), 463–491. https://doi.org/10.1039/c8ee01157e.

(7) Global Hydrogen Review 2021. *Glob. Hydrog. Rev. 2021* **2021**. https://doi.org/10.1787/39351842-en.

(8) Longden, T.; Beck, F. J.; Jotzo, F.; Andrews, R.; Prasad, M. 'Clean' Hydrogen? – Comparing the Emissions and Costs of Fossil Fuel versus Renewable Electricity Based Hydrogen. *Appl. Energy* **2022**, *306* (PB), 118145. https://doi.org/10.1016/j.apenergy.2021.118145.

(9) Balzani, V.; Credi, A.; Venturi, M. *Photochemical Conversion of Solar Energy*; 2008;

Vol. 1. https://doi.org/10.1002/cssc.200700087.

(10) Diebold, U. Photocatalysts: Closing the Gap. *Nat. Chem.* **2011**, *3* (4), 271–272. https://doi.org/10.1038/nchem.1019.

(11) Maeda, K.; Domen, K. Photocatalytic Water Splitting: Recent Progress and Future Challenges. *J. Phys. Chem. Lett.* **2010**, *1* (18), 2655–2661. https://doi.org/10.1021/jz1007966.

(12) Kalisman, P.; Nakibli, Y.; Amirav, L. Perfect Photon-to-Hydrogen Conversion Efficiency. *Nano Lett.* **2016**, *16*, 1776−1781. https://doi.org/10.1021/acs.nanolett.5b04813.

(13) Fujishima, a; Honda, K. Electrochemical Photolysis of Water at a Semiconductor Electrode. *Nature* **1972**, *238* (5358), 37–38. https://doi.org/10.1038/238037a0.

(14) Hisatomi, T.; Takanabe, K.; Domen, K. Photocatalytic Water-Splitting Reaction from Catalytic and Kinetic Perspectives. *Catal. Letters* **2014**, 95–108. https://doi.org/10.1007/s10562-014-1397-z.

(15) Goto, Y.; Hisatomi, T.; Wang, Q.; Higashi, T.; Ishikiriyama, K.; Maeda, T.; Sakata, Y.; Okunaka, S.; Tokudome, H.; Katayama, M.; Akiyama, S.; Nishiyama, H.; Inoue, Y.; Takewaki, T.; Setoyama, T.; Minegishi, T.; Takata, T.; Yamada, T.; Domen, K. A Particulate Photocatalyst Water-Splitting Panel for Large-Scale Solar Hydrogen Generation. *Joule* **2018**, *2* (3), 509–520. https://doi.org/10.1016/j.joule.2017.12.009.

(16) Nalajala, N.; Patra, K. K.; Bharad, P. A.; Gopinath, C. S. Why the Thin Film Form of a Photocatalyst Is Better than the Particulate Form for Direct Solar-to-Hydrogen Conversion: A Poor Man's Approach. *RSC Adv.* **2019**, *9* (11), 6094–6100. https://doi.org/10.1039/c8ra09982k.

(17) Wang, Q.; Domen, K. Particulate Photocatalysts for Light-Driven Water Splitting: Mechanisms, Challenges, and Design Strategies. *Chem. Rev.* **2020**, *120* (2), 919–985. https://doi.org/10.1021/acs.chemrev.9b00201.

(18) Chinnakonda S. Gopinath, and N. N. Scalable and Thin Film Approach for Solar Hydrogen Generation : A Review on Enhanced Photocatalytic Water Splitting. *J. Mater. Chem. A* **2020**, 1–19. https://doi.org/10.1039/c7ta07529d.

(19) Hisatomi, T.; Kubota, J.; Domen, K. Recent Advances in Semiconductors for Photocatalytic and Photoelectrochemical Water Splitting. *Chem. Soc. Rev.* **2014**, *43* (22), 7520–7535. https://doi.org/10.1039/C3CS60378D.

(20) Su, T.; Shao, Q.; Qin, Z.; Guo, Z.; Wu, Z. Role of Interfaces in Two-Dimensional Photocatalyst for Water Splitting. *ACS Catal.* **2018**, *8* (3). https://doi.org/10.1021/acscatal.7b03437.

(21) Moniz, S. J. A.; Shevlin, S. A.; Martin, D. J.; Guo, Z.-X.; Tang, J. Visible-Light Driven Heterojunction Photocatalysts for Water Splitting – a Critical Review. *Energy Environ. Sci.* **2015**, *8* (3), 731–759. https://doi.org/10.1039/C4EE03271C.

(22) Tee, S. Y.; Win, K. Y.; Teo, W. S.; Koh, L. D.; Liu, S.; Teng, C. P.; Han, M. Y. Recent Progress in Energy-Driven Water Splitting. *Advanced Science*. 2017. https://doi.org/10.1002/advs.201600337.

(23) Pan, Z.; Yanagi, R.; Wang, Q.; Shen, X.; Zhu, Q.; Xue, Y.; Röhr, J. A.; Hisatomi, T.; Domen, K.; Hu, S. Mutually-Dependent Kinetics and Energetics of Photocatalyst/Co-Catalyst/Two-Redox Liquid Junctions. *Energy Environ. Sci.* **2020**, *13* (1), 162–173. https://doi.org/10.1039/c9ee02910a.

(24) Low, J.; Yu, J.; Jaroniec, M.; Wageh, S.; Al-Ghamdi, A. A. Heterojunction

Photocatalysts. *Adv. Mater.* **2017**, *29* (20). https://doi.org/10.1002/adma.201601694.

(25) Wang, H.; Zhang, L.; Chen, Z.; Hu, J.; Li, S.; Wang, Z.; Liu, J.; Wang, X. Semiconductor Heterojunction Photocatalysts: Design, Construction, and Photocatalytic Performances. *Chemical Society Reviews*. 2014. https://doi.org/10.1039/c4cs00126e.

(26) Bardeen, J. Surface States and Rectification at a Metal Semi-Conductor Contact. *Phys. Rev.* **1947**, *71* (10), 717–727. https://doi.org/10.1103/PhysRev.71.717.

(27) Chen, X.; Wang, J.; Chai, Y.; Zhang, Z.; Zhu, Y. Efficient Photocatalytic Overall Water Splitting Induced by the Giant Internal Electric Field of a G-C3N4/RGO/PDIP Z-Scheme Heterojunction. *Adv. Mater.* **2021**, *33* (7), 1–7. https://doi.org/10.1002/adma.202007479.

(28) Sun, S.; Hisatomi, T.; Wang, Q.; Chen, S.; Ma, G.; Liu, J.; Nandy, S.; Minegishi, T.; Katayama, M.; Domen, K. Efficient Redox-Mediator-Free Z-Scheme Water Splitting Employing Oxysulfide Photocatalysts under Visible Light. *ACS Catal.* **2018**, *8* (3), 1690–1696. https://doi.org/10.1021/acscatal.7b03884.

(29) Maeda, K. Z-Scheme Water Splitting Using Two Different Semiconductor Photocatalysts. *ACS Catal.* **2013**, *3* (7), 1486–1503. https://doi.org/10.1021/cs4002089.

(30) Xu, Q.; Zhang, L.; Yu, J.; Wageh, S.; Al-Ghamdi, A. A.; Jaroniec, M. Direct Z-Scheme Photocatalysts: Principles, Synthesis, and Applications. *Mater. Today* **2018**, *21* (10), 1042–1063. https://doi.org/10.1016/j.mattod.2018.04.008.

(31) Kranz, C.; Wachtler, M. Characterizing Photocatalysts for Water Splitting: From Atoms to Bulk and from Slow to Ultrafast Processes. *Chem. Soc. Rev.* **2021**, *50* (2),

1407–1437. https://doi.org/10.1039/d0cs00526f.

(32) Li, X.; Yu, J.; Low, J.; Fang, Y.; Xiao, J.; Chen, X. Engineering Heterogeneous Semiconductors for Solar Water Splitting. *J. Mater. Chem. A* **2015**, *3* (6), 2485–2534. https://doi.org/10.1039/C4TA04461D.

(33) Schneider, J.; Bahnemann, D. W. Undesired Role of Sacrificial Reagents in Photocatalysis. *J. Phys. Chem. Lett.* **2013**, *4* (20), 3479–3483. https://doi.org/10.1021/jz4018199.

(34) Chen, W.; Huang, G. B.; Song, H.; Zhang, J. Efficient and Stable Charge Transfer Channels for Photocatalytic Water Splitting Activity of CdS without Sacrificial Agents. *J. Mater. Chem. A* **2020**, *8* (40), 20963–20969. https://doi.org/10.1039/d0ta06177h.

(35) Ni, M.; Leung, M. K. H.; Leung, D. Y. C.; Sumathy, K. A Review and Recent Developments in Photocatalytic Water-Splitting Using TiO2 for Hydrogen Production. *Renew. Sustain. Energy Rev.* **2007**, *11* (3), 401–425. https://doi.org/10.1016/j.rser.2005.01.009.

(36) Chen, X.; Shen, S.; Guo, L.; Mao, S. S. Semiconductor-Based Photocatalytic Hydrogen Generation. *Chem. Rev.* **2010**. https://doi.org/10.1021/cr1001645.

(37) Wang, X.; Maeda, K.; Thomas, A.; Takanabe, K.; Xin, G.; Carlsson, J. M.; Domen, K.; Antonietti, M. A Metal-Free Polymeric Photocatalyst for Hydrogen Production from Water under Visible Light. *Nat. Mater.* **2009**, *8* (1), 76–80. https://doi.org/10.1038/nmat2317.

(38) Psaltis, D.; Quake, S. R.; Yang, C. Developing Optofluidic Technology through the Fusion of Microfluidics and Optics. *Nature* **2006**, *442* (7101), 381–386.

https://doi.org/10.1038/nature05060.

(39) Schmidt, H.; Hawkins, A. R. The Photonic Integration of Non-Solid Media Using Optofluidics. *Nat. Photonics* **2011**, *5* (10), 598–604. https://doi.org/10.1038/nphoton.2011.163.

(40) Manz, A.; Graber, N.; Widmer, H. M. Miniaturized Total Chemical Analysis Systems: A Novel Concept for Chemical Sensing. *Sensors Actuators B Chem.* **1990**, *1*, 244–248. https://doi.org/10.1016/0925-4005(90)80209-I.

(41) Manz, A.; Effenhauser, C. S.; Burggraf, N.; Harrison, D. J.; Seiler, K.; Flurri, K. Electroosmotic Pumping and Electrophoretic Separations for Miniaturinzed Chemical Analysis Systems. *J. Micromechanics Microengineering* **1994**, *4*, 257.

(42) Wohlgemuth, R.; Plazl, I.; Žnidaršič-Plazl, P.; Gernaey, K. V.; Woodley, J. M. Microscale Technology and Biocatalytic Processes: Opportunities and Challenges for Synthesis. *Trends Biotechnol.* **2015**, *33* (5), 302–314. https://doi.org/10.1016/j.tibtech.2015.02.010.

(43) Bartlett, N. W.; Wood, R. J. Comparative Analysis of Fabrication Methods for Achieving Rounded Microchannels in PDMS. *J. Micromechanics Microengineering* **2016**, *26* (11), 1–10. https://doi.org/10.1088/0960-1317/26/11/115013.

(44) Rambabu, P.; Patel, S.; Gogoi, D.; Uppaluri, R. V. S.; Peela, N. R. Optofluidic Microreactor for the Photocatalytic Water Splitting to Produce Green Hydrogen. *Int. J. Hydrogen Energy* **2021**, 1–12. https://doi.org/10.1016/j.ijhydene.2021.10.171.

(45) Elliott, L. D.; Knowles, J. P.; Koovits, P. J.; Maskill, K. G.; Ralph, M. J.; Lejeune, G.; Edwards, L. J.; Robinson, R. I.; Clemens, I. R.; Cox, B.; Pascoe, D. D.; Koch, G.; Eberle, M.; Berry, M. B.; Booker-Milburn, K. I. Batch versus Flow Photochemistry: A

Revealing Comparison of Yield and Productivity. *Chem. - A Eur. J.* **2014**, *20* (46), 15226–15232. https://doi.org/10.1002/chem.201404347.

(46) Nagy, K. D.; Shen, B.; Jamison, T. F.; Jensen, K. F. Mixing and Dispersion in Small-Scale Flow Systems. *Org. Process Res. Dev.* **2012**, *16* (5), 976–981. https://doi.org/10.1021/op200349f.

(47) Yoshida, J. I.; Takahashi, Y.; Nagaki, A. Flash Chemistry: Flow Chemistry That Cannot Be Done in Batch. *Chem. Commun.* **2013**, *49* (85), 9896–9904. https://doi.org/10.1039/c3cc44709j.

(48) Camarri, S.; Mariotti, A.; Galletti, C.; Brunazzi, E.; Mauri, R.; Salvetti, M. V. An Overview of Flow Features and Mixing in Micro T and Arrow Mixers. *Ind. Eng. Chem. Res.* **2020**, *59* (9), 3669–3686. https://doi.org/10.1021/acs.iecr.9b04922.

(49) Yoshida, J. I.; Kim, H.; Nagaki, A. Green and Sustainable Chemical Synthesis Using Flow Microreactors. *ChemSusChem* **2011**, *4* (3), 331–340. https://doi.org/10.1002/cssc.201000271.

(50) Rossetti, I.; Compagnoni, M. Chemical Reaction Engineering, Process Design and Scale-up Issues at the Frontier of Synthesis: Flow Chemistry Identification of Limits and Potential of Microreactors Applied to Organic Synthesis. Review of Transport and Engineering Issues in Microreactor. *Chem. Eng. J.* **2016**, *296*, 56–70. https://doi.org/10.1016/j.cej.2016.02.119.

(51) Su, Y.; Straathof, N. J. W.; Hessel, V.; Noël, T. Photochemical Transformations Accelerated in Continuous-Flow Reactors: Basic Concepts and Applications. *Chem. - A Eur. J.* **2014**, *20*, 10562 – 10589. https://doi.org/10.1002/chem.201400283.

(52) Waheed, S.; Cabot, J. M.; Macdonald, N. P.; Lewis, T.; Guijt, R. M.; Paull, B.;

Breadmore, M. C. 3D Printed Microfluidic Devices: Enablers and Barriers. *Lab Chip* **2016**, *16* (11), 1993–2013. https://doi.org/10.1039/c6lc00284f.

(53) Berthier, E.; Young, E. W. K.; Beebe, D. Engineers Are from PDMS-Land, Biologists Are from Polystyrenia. *Lab Chip* **2012**, *12* (7), 1224–1237. https://doi.org/10.1039/c2lc20982a.

(54) Lee, J. N.; Park, C.; Whitesides, G. M. Solvent Compatibility of Poly (Dimethylsiloxane) -Based Microfluidic Devices. *Anal. Chem.* **2003**, *75* (23), 6544–6554. https://doi.org/10.1021/ac0346712.

(55) Toepke, M. W.; Beebe, D. J. PDMS Absorption of Small Molecules and Consequences in Microfluidic Applications. *Lab Chip* **2006**, *6* (12), 1484–1486. https://doi.org/10.1039/b612140c.

(56) Xia, Y.; Rogers, J. A.; Paul, K. E.; Whitesides, G. M. Unconventional Methods for Fabricating and Patterning Nanostructures. *Chem. Rev.* **1999**, *99* (7), 1823–1848. https://doi.org/10.1021/cr980002q.

(57) Wang, P.; Chu, W.; Li, W.; Tan, Y.; Qi, J.; Liao, Y.; Wang, Z.; Cheng, Y. Aberration-Insensitive Three-Dimensional Micromachining in Glass with Spatiotemporally Shaped Femtosecond Laser Pulses. *Opt. Lett.* **2018**, *43* (15), 3485–3488. https://doi.org/10.1364/OL.43.003485.

(58) Pearce, J. M. Building Research Equipment with Free, Open-Source Hardware. *Science (80-.).* **2012**, *337*, 1303–1304.

(59) Yuen, P. K.; Goral, V. N. Low-Cost Rapid Prototyping of Whole-Glass Microfluidic Devices. *J. Chem. Educ.* **2012**, *89* (10), 1288–1292. https://doi.org/10.1021/ed3000292.

(60) Bartholomeusz, D. A.; Kantak, A.; Lee, S.; Merugu, S.; Sant, H.; Boutte, R. W.; Gale, B. K.; Thomas, C.; Thomas, B. M. Xurography: Rapid Prototyping of Micro-Structures Using a Cutting Plotter. *J. MICROELECTROMECHANICAL Syst.* **2005**, *14* (6), 1364–1374.

(61) Martinez, A. W.; Phillips, S. T.; Whitesides, G. M. Three-Dimensional Microfluidic Devices Fabricated in Layered Paper and Tape. *Proc. Natl. Acad. Sci.* **2008**, *105* (50), 19606–19611. https://doi.org/10.1073/pnas.0810903105.

(62) Sims, P. A.; Greenleaf, W. J.; Duan, H.; Xie, X. S. Fluorogenic DNA Sequencing in PDMS Microreactors. *Nat. Methods* **2011**, *8* (7), 575–583. https://doi.org/10.1038/nmeth.1629.

(63) Lee, C. H.; Kim, D. R.; Zheng, X. Fabricating Nanowire Devices on Diverse Substrates by Simple Transfer-Printing Methods. *Proc. Natl. Acad. Sci.* **2010**, *107* (22), 9950–9955. https://doi.org/10.1073/pnas.0914031107.

(64) Zhang, L.; Wang, W.; Ju, X.-J.; Xie, R.; Liu, Z.; Chu, L.-Y. Fabrication of Glass-Based Microfluidic Devices with Dry Film Photoresists as Pattern Transfer Masks for Wet Etching. *RSC Adv.* **2015**, *5* (8), 5638–5646. https://doi.org/10.1039/C4RA15907A.

(65) Wang, Q.; Han, W.; Wang, Y.; Lu, M.; Dong, L. Tape Nanolithography: A Rapid and Simple Method for Fabricating Flexible, Wearable Nanophotonic Devices. *Microsystems Nanoeng.* **2018**, *4* (1), 1–12. https://doi.org/10.1038/s41378-018-0031-4.

(66) Nath, P.; Fung, D.; Kunde, Y. A.; Zeytun, A.; Branch, B.; Goddard, G. Rapid Prototyping of Robust and Versatile Microfluidic Components Using Adhesive Transfer Tapes. *Lab Chip* **2010**, *10* (17), 2286–2291. https://doi.org/10.1039/c002457k.

(67) Kim, J.; Surapaneni, R.; Gale, B. K. Rapid Prototyping of Microfluidic Systems Using a PDMS/Polymer Tape Composite. *Lab Chip* **2009**, *9* (9), 1290–1293. https://doi.org/10.1039/b818389a.

(68) Serra, M.; Pereiro, I.; Yamada, A.; Viovy, J. L.; Descroix, S.; Ferraro, D. A Simple and Low-Cost Chip Bonding Solution for High Pressure, High Temperature and Biological Applications. *Lab Chip* **2017**, *17* (4), 629–634. https://doi.org/10.1039/c6lc01319h.

(69) Comina, G.; Suska, A.; Filippini, D. Low Cost Lab-on-a-Chip Prototyping with a Consumer Grade 3D Printer. *Lab Chip* **2014**, *14* (16), 2978–2982. https://doi.org/10.1039/c4lc00394b.

(70) Pessoa De Santana, P.; Segato, T. P.; Carrilho, E.; Lima, R. S.; Dossi, N.; Kamogawa, M. Y.; Gobbi, A. L.; Piazzeta, M. H.; Piccin, E. Fabrication of Glass Microchannels by Xurography for Electrophoresis Applications. *Analyst* **2013**, *138* (6), 1660–1664. https://doi.org/10.1039/c3an36540a.

(71) Lei Zhang, Wei Wang, Xiao-Jie Ju, a Rui Xie, Z. L. and L.-Y. C. Fabrication of Glass-Based Microfluidic Devices with Dry Fi Lm Photoresists as Pattern Transfer Masks for Wet Etching †. *RSC Adv.* **2015**, *5*, 5638–5646. https://doi.org/10.1039/c4ra15907a.

(72) Nagarah, J. M.; Wagenaar, D. A. Ultradeep Fused Silica Glass Etching with an HF-Resistant Photosensitive Resist for Optical Imaging Applications. *J. Micromechanics Microengineering* **2012**, *22* (3). https://doi.org/10.1088/0960-1317/22/3/035011.

(73) Iliescu, C.; Jing, J.; Tay, F. E. H.; Miao, J.; Sun, T. Characterization of Masking Layers for Deep Wet Etching of Glass in an Improved HF/HCl Solution. *Surf. Coatings Technol.* **2005**, *198* (1-3 SPEC. ISS.), 314–318. https://doi.org/10.1016/j.surfcoat.2004.10.094.

(74) Tay, F. E. H.; Iliescu, C.; Jing, J.; Miao, J. Defect-Free Wet Etching through Pyrex Glass Using Cr/Au Mask. *Microsyst. Technol.* **2006**, *12*, 935–939. https://doi.org/10.1007/s00542-006-0116-0.

(75) Iliescu, C.; Miao, J.; Tay, F. E. H. Optimization of an Amorphous Silicon Mask PECVD Process for Deep Wet Etching of Pyrex Glass. *Surf. Coatings Technol.* **2005**, *192* (1), 43–47. https://doi.org/10.1016/j.surfcoat.2004.03.043.

(76) Lin, C.-H.; Lee, G.-B.; Lin, Y.-H.; Chang, G.-L. A Fast Prototyping Process for Fabrication of Microfluidic Systems on Soda-Lime Glass. *J. Micromechanics Microengineering* **2001**, *11* (6), 726–732. https://doi.org/10.1088/0960-1317/11/6/316.

(77) Greer, J.; Sundberg, S. O.; Wittwer, C. T.; Gale, B. K. Comparison of Glass Etching to Xurography Prototyping of Microfluidic Channels for DNA Melting Analysis. *J. Micromechanics Microengineering* **2007**, *17* (12), 2407–2413. https://doi.org/10.1088/0960-1317/17/12/003.

(78) Tay, F. E. H.; Iliescu, C.; Jing, J.; Miao, J. Defect-Free Wet Etching through Pyrex Glass Using Cr/Au Mask. In *Microsystem Technologies*; 2006. https://doi.org/10.1007/s00542-006-0116-0.

(79) Iliescu, C.; Miao, J.; Tay, F. E. H. Optimization of an Amorphous Silicon Mask PECVD Process for Deep Wet Etching of Pyrex Glass. *Surf. Coatings Technol.* **2005**, *192*, 43–47. https://doi.org/10.1016/j.surfcoat.2004.03.043.

(80) Coltro, W. K. T.; Piccin, E.; Fracassi da Silva, J. A.; Lucio do Lago, C.; Carrilho, E. A Toner-Mediated Lithographic Technology for Rapid Prototyping of Glass Microchannels. *Lab Chip* **2007**, *7*, 931–934. https://doi.org/10.1039/b702931d.

(81) Ahsan, S. S.; Gumus, A.; Erickson, D. Redox Mediated Photocatalytic Water-Splitting

in Optofluidic Microreactors. *Lab Chip* **2013**, *13* (3), 409–414. https://doi.org/10.1039/c2lc41129f.

(82) Li, L.; Chen, R.; Liao, Q.; Zhu, X.; Wang, G.; Wang, D. High Surface Area Optofluidic Microreactor for Redox Mediated Photocatalytic Water Splitting. *Int. J. Hydrogen Energy* **2014**, *39* (33), 19270–19276. https://doi.org/10.1016/j.ijhydene.2014.05.098.

(83) Chen, R.; Li, L.; Zhu, X.; Wang, H.; Liao, Q.; Zhang, M. X. Highly-Durable Optofluidic Microreactor for Photocatalytic Water Splitting. *Energy* **2015**, *83*, 797–804. https://doi.org/10.1016/j.energy.2015.02.097.

(84) Cheng, L.; Xiang, Q.; Liao, Y.; Zhang, H. CdS-Based Photocatalysts. *Energy Environ. Sci.* **2018**, *11* (6), 1362–1391. https://doi.org/10.1039/c7ee03640j.

(85) Nasir, J. A.; Rehman, Z. U.; Shah, S. N. A.; Khan, A.; Butler, I. S.; Catlow, C. R. A. Recent Developments and Perspectives in CdS-Based Photocatalysts for Water Splitting. *J. Mater. Chem. A* **2020**, *8* (40), 20752–20780. https://doi.org/10.1039/d0ta05834c.

(86) Ning, X.; Lu, G. Photocorrosion Inhibition of CdS-Based Catalysts for Photocatalytic Overall Water Splitting. *Nanoscale* **2020**, *12* (3), 1213–1223. https://doi.org/10.1039/c9nr09183a.

(87) Djordjevic, V. R.; Wallace, D. R.; Schweitzer, A.; Boricic, N.; Knezevic, D.; Matic, S.; Grubor, N.; Kerkez, M.; Radenkovic, D.; Bulat, Z.; Antonijevic, B.; Matovic, V.; Buha, A. Environmental Cadmium Exposure and Pancreatic Cancer: Evidence from Case Control, Animal and in Vitro Studies. *Environ. Int.* **2019**, *128* (January), 353–361. https://doi.org/10.1016/j.envint.2019.04.048.

(88) Buha, A.; Jugdaohsingh, R.; Matovic, V.; Bulat, Z.; Antonijevic, B.; Kerns, J. G.; Goodship, A.; Hart, A.; Powell, J. J. Bone Mineral Health Is Sensitively Related to Environmental Cadmium Exposure- Experimental and Human Data. *Environ. Res.* **2019**, *176* (May), 108539. https://doi.org/10.1016/j.envres.2019.108539.

(89) Renieri, E. A.; Sfakianakis, D. G.; Alegakis, A. A.; Safenkova, I. V.; Buha, A.; Matović, V.; Tzardi, M.; Dzantiev, B. B.; Divanach, P.; Kentouri, M.; Tsatsakis, A. M. Nonlinear Responses to Waterborne Cadmium Exposure in Zebrafish. An in Vivo Study. *Environ. Res.* **2017**, *157* (May), 173–181. https://doi.org/10.1016/j.envres.2017.05.021.

(90) Varmazyari, A.; Taghizadehghalehjoughi, A.; Sevim, C.; Baris, O.; Eser, G.; Yildirim, S.; Hacimuftuoglu, A.; Buha, A.; Wallace, D. R.; Tsatsakis, A.; Aschner, M.; Mezhuev, Y. Cadmium Sulfide-Induced Toxicity in the Cortex and Cerebellum: In Vitro and in Vivo Studies. *Toxicol. Reports* **2020**, *7* (April), 637–648. https://doi.org/10.1016/j.toxrep.2020.04.011.

(91) Lu, X.; Chen, W.; Yao, Y.; Wen, X.; Hart, J. N.; Tsounis, C.; Ying Toe, C.; Scott, J.; Ng, Y. H. Photogenerated Charge Dynamics of CdS Nanorods with Spatially Distributed MoS2 for Photocatalytic Hydrogen Generation. *Chem. Eng. J.* **2021**, *420* (P2), 127709. https://doi.org/10.1016/j.cej.2020.127709.

(92) Pan, J.; Li, H.; Li, S.; Ou, W.; Liu, Y.; Wang, J.; Song, C.; Zheng, Y.; Li, C. The Enhanced Photocatalytic Hydrogen Production of Nickel-Cobalt Bimetals Sulfide Synergistic Modified CdS Nanorods with Active Facets. *Renew. Energy* **2020**, *156*, 469–477. https://doi.org/10.1016/j.renene.2020.04.053.

(93) Su, L.; Luo, L.; Song, H.; Wu, Z.; Tu, W.; Wang, Z. jun; Ye, J. Hemispherical Shell-Thin Lamellar WS2 Porous Structures Composited with CdS Photocatalysts for

Enhanced H2 Evolution. *Chem. Eng. J.* **2020**, *388* (February), 124346. https://doi.org/10.1016/j.cej.2020.124346.

(94) Gogoi, D.; Shah, A. K.; Rambabu, P.; Qureshi, M.; Golder, A. K.; Peela, N. R. Step-Scheme Heterojunction between CdS Nanowires and Facet-Selective Assembly of MnO x -BiVO 4 for an Efficient Visible-Light-Driven Overall Water Splitting . *ACS Appl. Mater. Interfaces* **2021**. https://doi.org/10.1021/acsami.1c11740.

(95) Tian, L.; Wang, F.; Zhang, Z.; Min, S. Vanadium Diboride as an Efficient Cocatalyst Coupled with CdS for Enhanced Visible Light Photocatalytic H2 Evolution. *Int. J. Hydrogen Energy* **2020**, *45* (38), 19017–19026. https://doi.org/10.1016/j.ijhydene.2020.05.136.

(96) Banerjee, R.; Pal, A.; Ghosh, D.; Ghosh, A. B.; Nandi, M.; Biswas, P. Improved Photocurrent Response, Photostability and Photocatalytic Hydrogen Generation Ability of CdS Nanoparticles in Presence of Mesoporous Carbon. *Mater. Res. Bull.* **2021**, *134* (September 2020), 111085. https://doi.org/10.1016/j.materresbull.2020.111085.

(97) Liu, S.; Guo, Z.; Qian, X.; Zhang, J.; Liu, J.; Lin, J. Sonochemical Deposition of Ultrafine Metallic Pt Nanoparticles on CdS for Efficient Photocatalytic Hydrogen Evolution. *Sustain. Energy Fuels* **2019**, *3* (4), 1048–1054. https://doi.org/10.1039/C9SE00050J.

(98) Ren, D.; Liang, Z. Z.; Ng, Y. H.; Zhang, P.; Xiang, Q.; Li, X. Strongly Coupled 2D-2D Nanojunctions between P-Doped Ni2S (Ni2SP) Cocatalysts and CdS Nanosheets for Efficient Photocatalytic H2 Evolution. *Chem. Eng. J.* **2020**, *390* (February), 124496. https://doi.org/10.1016/j.cej.2020.124496.

(99) Zhen, W.; Ning, X.; Yang, B.; Wu, Y.; Li, Z.; Lu, G. The Enhancement of CdS

Photocatalytic Activity for Water Splitting via Anti-Photocorrosion by Coating Ni2P Shell and Removing Nascent Formed Oxygen with Artificial Gill. *Appl. Catal. B Environ.* **2018**, *221* (September 2017), 243–257. https://doi.org/10.1016/j.apcatb.2017.09.024.

(100) Zhang, T.; Meng, F.; Cheng, Y.; Dewangan, N.; Ho, G. W.; Kawi, S. Z-Scheme Transition Metal Bridge of Co9S8/Cd/CdS Tubular Heterostructure for Enhanced Photocatalytic Hydrogen Evolution. *Appl. Catal. B Environ.* **2021**, *286* (November 2020), 119853. https://doi.org/10.1016/j.apcatb.2020.119853.

(101) Iqbal, W.; Yang, B.; Zhao, X.; Rauf, M.; Waqas, M.; Gong, Y.; Zhang, J.; Mao, Y. Controllable Synthesis of Graphitic Carbon Nitride Nanomaterials for Solar Energy Conversion and Environmental Remediation: The Road Travelled and the Way Forward. *Catal. Sci. Technol.* **2018**, *8* (18), 4576–4599. https://doi.org/10.1039/c8cy01061g.

(102) Ong, W. J.; Tan, L. L.; Ng, Y. H.; Yong, S. T.; Chai, S. P. Graphitic Carbon Nitride (g-C3N4)-Based Photocatalysts for Artificial Photosynthesis and Environmental Remediation: Are We a Step Closer to Achieving Sustainability? *Chem. Rev.* **2016**, *116* (12), 7159–7329. https://doi.org/10.1021/acs.chemrev.6b00075.

(103) Yi, J.; El-Alami, W.; Song, Y.; Li, H.; Ajayan, P. M.; Xu, H. Emerging Surface Strategies on Graphitic Carbon Nitride for Solar Driven Water Splitting. *Chem. Eng. J.* **2020**, *382* (September 2019), 122812. https://doi.org/10.1016/j.cej.2019.122812.

(104) Teixeira, I. F.; Barbosa, E. C. M.; Tsang, S. C. E.; Camargo, P. H. C. Carbon Nitrides and Metal Nanoparticles: From Controlled Synthesis to Design Principles for Improved Photocatalysis. *Chem. Soc. Rev.* **2018**, *47* (20), 7783–7817. https://doi.org/10.1039/c8cs00479j.

(105) He, F.; Chen, G.; Miao, J.; Wang, Z.; Su, D.; Liu, S.; Cai, W.; Zhang, L.; Hao, S.; Liu, B. Sulfur-Mediated Self-Templating Synthesis of Tapered C-PAN/g-C3N4 Composite Nanotubes toward Efficient Photocatalytic H2 Evolution. *ACS Energy Lett.* **2016**, *1* (5), 969–975. https://doi.org/10.1021/acsenergylett.6b00398.

(106) Gao, Q.; Hu, S.; Du, Y.; Hu, Z. The Origin of the Enhanced Photocatalytic Activity of Carbon Nitride Nanotubes: A First-Principles Study. *J. Mater. Chem. A* **2017**, *5* (10), 4827–4834. https://doi.org/10.1039/c6ta09747b.

(107) Chen, L.; Song, Z.; Liu, X.; Guo, L.; Li, M. J.; Fu, F. Barbituric Acid-Modified Graphitic Carbon Nitride Nanosheets for Ratiometric Fluorescent Detection of Cu2+. *Analyst* **2018**, *143* (7), 1609–1614. https://doi.org/10.1039/c7an02089a.

(108) Raizada, P.; Sudhaik, A.; Singh, P.; Hosseini-Bandegharaei, A.; Thakur, P. Converting Type II AgBr/VO into Ternary Z Scheme Photocatalyst via Coupling with Phosphorus Doped g-C3N4 for Enhanced Photocatalytic Activity. *Sep. Purif. Technol.* **2019**, *227* (June), 115692. https://doi.org/10.1016/j.seppur.2019.115692.

(109) Liu, M.; Xia, P.; Zhang, L.; Cheng, B.; Yu, J. Enhanced Photocatalytic H2-Production Activity of g-C3N4 Nanosheets via Optimal Photodeposition of Pt as Cocatalyst. *ACS Sustain. Chem. Eng.* **2018**, *6* (8), 10472–10480. https://doi.org/10.1021/acssuschemeng.8b01835.

(110) Su, T.; Hood, Z. D.; Naguib, M.; Bai, L.; Luo, S.; Rouleau, C. M.; Ivanov, I. N.; Ji, H.; Qin, Z.; Wu, Z. 2D/2D Heterojunction of Ti 3 C 2 /g-C 3 N 4 Nanosheets for Enhanced Photocatalytic Hydrogen Evolution. *Nanoscale* **2019**, *11* (17), 8138–8149. https://doi.org/10.1039/c9nr00168a.

(111) Dong, F.; Zhao, Z.; Sun, Y.; Zhang, Y.; Yan, S.; Wu, Z. An Advanced Semimetal-Organic Bi Spheres-g-C3N4 Nanohybrid with SPR-Enhanced Visible-Light

Photocatalytic Performance for NO Purification. *Environ. Sci. Technol.* **2015**, *49* (20), 12432–12440. https://doi.org/10.1021/acs.est.5b03758.

(112) Bi, L.; Xu, D.; Zhang, L.; Lin, Y.; Wang, D.; Xie, T. Metal Ni-Loaded g-C3N4 for Enhanced Photocatalytic H2 Evolution Activity: The Change in Surface Band Bending. *Phys. Chem. Chem. Phys.* **2015**, *17* (44), 29899–29905. https://doi.org/10.1039/c5cp05158d.

(113) Zhang, J.; Zhang, M.; Lin, S.; Fu, X.; Wang, X. Molecular Doping of Carbon Nitride Photocatalysts with Tunable Bandgap and Enhanced Activity. *J. Catal.* **2014**, *310*, 24–30. https://doi.org/10.1016/j.jcat.2013.01.008.

(114) Jiao, X.; Zheng, K.; Hu, Z.; Sun, Y.; Xie, Y. Broad-Spectral-Response Photocatalysts for CO2 Reduction. *ACS Cent. Sci.* **2020**, *6* (5), 653–660. https://doi.org/10.1021/acscentsci.0c00325.

(115) Fu, J.; Chang, B.; Tian, Y.; Xi, F.; Dong, X. Novel C3N4-CdS Composite Photocatalysts with Organic-Inorganic Heterojunctions: In Situ Synthesis, Exceptional Activity, High Stability and Photocatalytic Mechanism. *J. Mater. Chem. A* **2013**, *1* (9), 3083–3090. https://doi.org/10.1039/c2ta00672c.

(116) Gogoi, D.; Shah, A. K.; Qureshi, M.; Golder, A. K.; Peela, N. R. Silver Grafted Graphitic-Carbon Nitride Ternary Hetero-Junction Ag/GC3N4(Urea)-GC3N4(Thiourea) with Efficient Charge Transfer for Enhanced Visible-Light Photocatalytic Green H2 Production. *Appl. Surf. Sci.* **2021**, *558* (February), 149900. https://doi.org/10.1016/j.apsusc.2021.149900.

(117) Liu, W.; Zhang, D.; Wang, R.; Zhang, Z.; Qiu, S. 2D/2D Interface Engineering Promotes Charge Separation of Mo2C/g-C3N4Nanojunction Photocatalysts for Efficient Photocatalytic Hydrogen Evolution. *ACS Appl. Mater. Interfaces* **2022**, *14*

(28), 31782–31791. https://doi.org/10.1021/acsami.2c03421.

(118) Zhang, Q.; Bai, X.; Hu, X.; Fan, J.; Liu, E. Efficient Photocatalytic H2 Evolution over 2D/2D S-Scheme NiTe2/g-C3N4 Heterojunction with Superhydrophilic Surface. *Appl. Surf. Sci.* **2022**, *579* (September 2021), 152224. https://doi.org/10.1016/j.apsusc.2021.152224.

(119) Ge, L.; Zuo, F.; Liu, J.; Ma, Q.; Wang, C.; Sun, D.; Bartels, L.; Feng, P. Synthesis and Efficient Visible Light Photocatalytic Hydrogen Evolution of Polymeric G-C 3N 4 Coupled with CdS Quantum Dots. *J. Phys. Chem. C* **2012**, *116* (25), 13708–13714. https://doi.org/10.1021/jp3041692.

(120) Chi, X.; Liu, F.; Gao, Y.; Song, J.; Guan, R.; Yuan, H. An Efficient B/Na Co-Doped Porous g-C3N4 Nanosheets Photocatalyst with Enhanced Photocatalytic Hydrogen Evolution and Degradation of Tetracycline under Visible Light. *Appl. Surf. Sci.* **2022**, *576* (PA), 151837. https://doi.org/10.1016/j.apsusc.2021.151837.

(121) Wang, L.; Lian, R.; Zhang, Y.; Ma, X.; Huang, J.; She, H.; Liu, C.; Wang, Q. Rational Preparation of Cocoon-like g-C3N4/COF Hybrids: Accelerated Intramolecular Charge Delivery for Photocatalytic Hydrogen Evolution. *Appl. Catal. B Environ.* **2022**, *315* (May), 121568. https://doi.org/10.1016/j.apcatb.2022.121568.

(122) Yang, T.; Shao, Y.; Hu, J.; Qu, J.; Yang, X.; Yang, F.; Ming Li, C. Ultrathin Layered 2D/2D Heterojunction of ReS2/High-Crystalline g-C3N4 for Significantly Improved Photocatalytic Hydrogen Evolution. *Chem. Eng. J.* **2022**, *448* (May), 137613. https://doi.org/10.1016/j.cej.2022.137613.

(123) Wang, X.; Wang, X.; Tian, W.; Meng, A.; Li, Z.; Li, S.; Wang, L.; Li, G. High-Energy Ball-Milling Constructing P-Doped g-C3N4/MoP Heterojunction with Mo–N Bond Bridged Interface and Schottky Barrier for Enhanced Photocatalytic H2 Evolution.

Appl. Catal. B Environ. **2022**, *303* (November 2021), 120933. https://doi.org/10.1016/j.apcatb.2021.120933.

(124) Chandra, M.; Guharoy, U.; Pradhan, D. Boosting the Photocatalytic H2Evolution and Benzylamine Oxidation Using 2 D/1D g-C3N4/TiO2Nanoheterojunction. *ACS Appl. Mater. Interfaces* **2022**. https://doi.org/10.1021/acsami.2c03230.

(125) Fu, J.; Yu, J.; Jiang, C.; Cheng, B. G-C3N4-Based Heterostructured Photocatalysts. *Adv. Energy Mater.* **2018**, *8* (3), 1–31. https://doi.org/10.1002/aenm.201701503.

(126) Wang, P.; Wu, T.; Wang, C.; Hou, J.; Qian, J.; Ao, Y. Combining Heterojunction Engineering with Surface Cocatalyst Modification to Synergistically Enhance the Photocatalytic Hydrogen Evolution Performance of Cadmium Sulfide Nanorods. *ACS Sustain. Chem. Eng.* **2017**, *5* (9), 7670–7677. https://doi.org/10.1021/acssuschemeng.7b01043.

(127) Wang, Z.; Li, C.; Domen, K. Recent Developments in Heterogeneous Photocatalysts for Solar-Driven Overall Water Splitting. *Chem. Soc. Rev.* **2019**, *48* (7), 2109–2125. https://doi.org/10.1039/c8cs00542g.

(128) Jang, J. S.; Kim, H. G.; Lee, J. S. Heterojunction Semiconductors: A Strategy to Develop Efficient Photocatalytic Materials for Visible Light Water Splitting. *Catal. Today* **2012**, *185* (1), 270–277. https://doi.org/10.1016/j.cattod.2011.07.008.

(129) Ran, Y.; Cui, Y.; Zhang, Y.; Fang, Y.; Zhang, W.; Yu, X.; Lan, H.; An, X. Assembly-Synthesis of Puff Pastry-like g-C3N4/CdS Heterostructure as S-Junctions for Efficient Photocatalytic Water Splitting. *Chem. Eng. J.* **2022**, *431* (P4), 133348. https://doi.org/10.1016/j.cej.2021.133348.

(130) Hu, T.; Dai, K.; Zhang, J.; Chen, S. Noble-Metal-Free Ni2P Modified Step-Scheme

SnNb2O6/CdS-Diethylenetriamine for Photocatalytic Hydrogen Production under Broadband Light Irradiation. *Appl. Catal. B Environ.* **2020**, *269* (March), 118844. https://doi.org/10.1016/j.apcatb.2020.118844.

(131) Li, X.; Zhang, J.; Huo, Y.; Dai, K.; Li, S.; Chen, S. Two-Dimensional Sulfur- and Chlorine-Codoped g-C3N4/CdSe-Amine Heterostructures Nanocomposite with Effective Interfacial Charge Transfer and Mechanism Insight. *Appl. Catal. B Environ.* **2021**, *280* (July 2020), 119452. https://doi.org/10.1016/j.apcatb.2020.119452.

(132) Wu, Q.; Lu, D.; Kondamareddy, K. K.; Ho, W.; Wang, Q.; Zhang, Y.; Zeng, Y.; Zhang, B.; Xie, L.; Zhao, B.; Wang, Z.; Hao, H.; Fan, H.; Wang, H. In-Situ Synthesis of Ternary Heterojunctions via g-C3N4 Coupling with Noble-Metal-Free NiS and CdS with Efficient Visible-Light-Induced Photocatalytic H2 Evolution and Mechanism Insight. *Int. J. Hydrogen Energy* **2022**, *47* (30), 14063–14076. https://doi.org/10.1016/j.ijhydene.2022.02.153.

(133) Ke, X.; Zhang, J.; Dai, K.; Fan, K.; Liang, C. Integrated S-Scheme Heterojunction of Amine-Functionalized 1D CdSe Nanorods Anchoring on Ultrathin 2D SnNb2O6 Nanosheets for Robust Solar-Driven CO2 Conversion. *Sol. RRL* **2021**, *5* (4), 1–11. https://doi.org/10.1002/solr.202000805.

(134) Yan, Z.; Sun, Z.; Liu, X.; Jia, H.; Du, P. Cadmium Sulfide/Graphitic Carbon Nitride Heterostructure Nanowire Loading with a Nickel Hydroxide Cocatalyst for Highly Efficient Photocatalytic Hydrogen Production in Water under Visible Light. *Nanoscale* **2016**, *8* (8), 4748–4756. https://doi.org/10.1039/c6nr00160b.

(135) Yuan, J.; Wen, J.; Zhong, Y.; Li, X.; Fang, Y.; Zhang, S.; Liu, W. Enhanced Photocatalytic H2 Evolution over Noble-Metal-Free NiS Cocatalyst Modified CdS Nanorods/g-C3N4 Heterojunctions. *J. Mater. Chem. A* **2015**, *3* (35), 18244–18255.

https://doi.org/10.1039/c5ta04573h.

(136) Xiao, F. X.; Miao, J.; Liu, B. Layer-by-Layer Self-Assembly of CdS Quantum Dots/Graphene Nanosheets Hybrid Films for Photoelectrochemical and Photocatalytic Applications. *J. Am. Chem. Soc.* **2014**, *136* (4), 1559–1569. https://doi.org/10.1021/ja411651e.

(137) An, X.; Yu, X.; Yu, J. C.; Zhang, G. CdS Nanorods/Reduced Graphene Oxide Nanocomposites for Photocatalysis and Electrochemical Sensing. *J. Mater. Chem. A* **2013**, *1* (16), 5158–5164. https://doi.org/10.1039/c3ta00029j.

(138) Liu, L.; Qi, Y.; Hu, J.; Liang, Y.; Cui, W. Efficient Visible-Light Photocatalytic Hydrogen Evolution and Enhanced Photostability of Core@shell Cu 2 O@g-C 3 N 4 Octahedra. *Appl. Surf. Sci.* **2015**, *351*, 1146–1154. https://doi.org/10.1016/j.apsusc.2015.06.119.

(139) Akple, M. S.; Low, J.; Wageh, S.; Al-Ghamdi, A. A.; Yu, J.; Zhang, J. Enhanced Visible Light Photocatalytic H 2 -Production of g-C 3 N 4 /WS 2 Composite Heterostructures. *Appl. Surf. Sci.* **2015**, *358*, 196–203. https://doi.org/10.1016/j.apsusc.2015.08.250.

(140) Bessekhouad, Y.; Robert, D.; Weber, J. V. Bi2S3/TiO2 and CdS/TiO2 Heterojunctions as an Available Configuration for Photocatalytic Degradation of Organic Pollutant. *J. Photochem. Photobiol. A Chem.* **2004**, *163* (3), 569–580. https://doi.org/10.1016/j.jphotochem.2004.02.006.

(141) Sun, Z.; Zheng, H.; Li, J.; Du, P. Extraordinarily Efficient Photocatalytic Hydrogen Evolution in Water Using Semiconductor Nanorods Integrated with Crystalline Ni2P Cocatalysts. *Energy Environ. Sci.* **2015**, *8* (9), 2668–2676. https://doi.org/10.1039/c5ee01310k.

(142) Gao, J.; Zhang, F.; Xue, H.; Zhang, L.; Peng, Y.; Li, X. L.; Gao, Y.; Li, N.; Lei, G. In-Situ Synthesis of Novel Ternary CdS/PdAg/g-C3N4 Hybrid Photocatalyst with Significantly Enhanced Hydrogen Production Activity and Catalytic Mechanism Exploration. *Appl. Catal. B Environ.* **2021**, *281* (18). https://doi.org/10.1016/j.apcatb.2020.119509.

(143) Gao, H.; Zhang, S.; Xu, J.; Dou, Y.; Zhou, J.; Zhou, R. Activating and Optimizing Activity of CdS@g-C3N4 Heterojunction for Photocatalytic Hydrogen Evolution through the Synergistic Effect of Phosphorus Doping and Defects. *J. Alloys Compd.* **2020**, *834*, 155201. https://doi.org/10.1016/j.jallcom.2020.155201.

(144) Wang, Y.; Zhang, X.; Liu, Y.; Zhao, Y.; Xie, C.; Song, Y.; Yang, P. Crystallinity and Phase Controlling of G-C3N4 /CdS Hetrostructures towards High Efficient Photocatalytic H2 Generation. *Int. J. Hydrogen Energy* **2019**, *44* (57), 30151–30159. https://doi.org/10.1016/j.ijhydene.2019.09.181.

(145) Chu, J.; Han, X.; Yu, Z.; Du, Y.; Song, B.; Xu, P. Highly Efficient Visible-Light-Driven Photocatalytic Hydrogen Production on CdS/Cu7S4/g-C3N4 Ternary Heterostructures. *ACS Appl. Mater. Interfaces* **2018**, *10* (24), 20404–20411. https://doi.org/10.1021/acsami.8b02984.

(146) Ren, D.; Zhang, W.; Ding, Y.; Shen, R.; Jiang, Z.; Lu, X.; Li, X. In Situ Fabrication of Robust Cocatalyst-Free CdS/g-C3N4 2D–2D Step-Scheme Heterojunctions for Highly Active H2 Evolution. *Sol. RRL* **2020**, *4* (8), 1–11. https://doi.org/10.1002/solr.201900423.

(147) Liu, H.; Cheng, D. G.; Chen, F.; Zhan, X. 2D Porous N-Deficient g-C3N4Nanosheet Decorated with CdS Nanoparticles for Enhanced Visible-Light-Driven Photocatalysis. *ACS Sustain. Chem. Eng.* **2020**, *8* (45), 16897–16904.

https://doi.org/10.1021/acssuschemeng.0c06004.

(148) Ma, W.; Zheng, D.; Xian, Y.; Hu, X.; Zhang, Q.; Wang, S.; Cheng, C.; Liu, J.; Wang, P. Efficient Hydrogen Evolution under Visible Light by Bimetallic Phosphide NiCoP Combined with G-C3N4/CdS S-Scheme Heterojunction. *ChemCatChem* **2021**, *13* (20), 4403–4410. https://doi.org/10.1002/cctc.202100833.

(149) Ahsan, S. S.; Gumus, A.; Erickson, D. Redox Mediated Photocatalytic Water-Splitting in Optofluidic Microreactors. *Lab Chip* **2013**, *13* (3), 409–414. https://doi.org/10.1039/C2LC41129F.

(150) Xiong, A.; Ma, G.; Maeda, K.; Takata, T.; Hisatomi, T.; Setoyama, T.; Kubota, J.; Domen, K. Fabrication of Photocatalyst Panels and the Factors Determining Their Activity for Water Splitting. *Catal. Sci. Technol.* **2014**, *4* (2), 325–328. https://doi.org/10.1039/c3cy00845b.

(151) Schröder, M.; Kailasam, K.; Borgmeyer, J.; Neumann, M.; Thomas, A.; Schomäcker, R.; Schwarze, M. Hydrogen Evolution Reaction in a Large-Scale Reactor Using a Carbon Nitride Photocatalyst under Natural Sunlight Irradiation. *Energy Technol.* **2015**, *3* (10), 1014–1017. https://doi.org/10.1002/ente.201500142.

(152) Rao Pala, L. P.; Peela, N. R. Green Hydrogen Production in an Optofluidic Planar Microreactor via Photocatalytic Water Splitting under Visible/Simulated Sunlight Irradiation. *Energy and Fuels* **2021**, *35* (23), 19737–19747. https://doi.org/10.1021/acs.energyfuels.1c02686.

(153) Iliescu, C. Wet Etching of Glass for MEMS Applications. *J. Mater. Chem.* **2009**, *19* (43), 8142. https://doi.org/10.1039/b913151e.

(154) Nageswara Rao, P.; Kunzru, D. Fabrication of Microchannels on Stainless Steel by

Wet Chemical Etching. *J. Micromechanics Microengineering* **2007**, *17*, N99–N106. https://doi.org/10.1088/0960-1317/17/12/N01.

(155) Iliescu, C.; Miao, J.; Tay, F. E. H. Stress Control in Masking Layers for Deep Wet Micromachining of Pyrex Glass. *Sensors Actuators, A Phys.* **2005**, *117*, 286–292. https://doi.org/10.1016/j.sna.2004.03.004.

(156) Zhu, H.; Holl, M.; Ray, T.; Bhushan, S.; Meldrum, D. R. Characterization of Deep Wet Etching of Fused Silica Glass for Single Cell and Optical Sensor Deposition. *J. Micromechanics Microengineering* **2009**, *19* (6), 1–8. https://doi.org/10.1088/0960-1317/19/6/065013.

(157) Suratwala, T. I.; Miller, P. E.; Bude, J. D.; Steele, W. A.; Shen, N.; Monticelli, M. V; Feit, M. D.; Laurence, T. A.; Norton, M. A.; Carr, C. W.; Wong, L. L. Fused Silica Optical Surfaces. *J. Am. Ceram. Soc.* **2011**, *428*, 416–428. https://doi.org/10.1111/j.1551-2916.2010.04112.x.

(158) Abgrall, P.; Gué, A. M. Lab-on-Chip Technologies: Making a Microfluidic Network and Coupling It into a Complete Microsystem - A Review. *J. Micromechanics Microengineering* **2007**, *17* (5), R15–R49. https://doi.org/10.1088/0960-1317/17/5/R01.

(159) Pekas, N.; Zhang, Q.; Nannini, M.; Juncker, D. Wet-Etching of Structures with Straight Facets and Adjustable Taper into Glass Substrates. *Lab Chip* **2010**, *10*, 494–498. https://doi.org/10.1039/b912770d.

(160) Mu, X.; Liang, Q.; Hu, P.; Ren, K.; Wang, Y.; Luo, G. Laminar Flow Used as “Liquid Etch Mask” in Wet Chemical Etching to Generate Glass Microstructures with an Improved Aspect Ratio. *Lab Chip* **2009**, *9*, 1994–1996. https://doi.org/10.1039/b904769g.

(161) Ren, K.; Zhou, J.; Wu, H. Materials for Microfluidic Chip Fabrication. *Acc. Chem. Res.* **2013**, *46* (11), 2396–2406. https://doi.org/10.1021/ar300314s.

(162) Wang, Q.; Lian, J.; Li, J.; Wang, R.; Huang, H.; Su, B.; Lei, Z. Highly Efficient Photocatalytic Hydrogen Production of Flower-like Cadmium Sulfide Decorated by Histidine. *Sci. Rep.* **2015**, *5* (September 2014), 1–9. https://doi.org/10.1038/srep13593.

(163) Jemish Parmar, Seungwook Jang, Lluís Soler, D.-P. K. and S. S. Nano-Photocatalysts in Microfluidics, Energy Conversion and Environmental Applications. *Lab Chip* **2015**, *15*, 2352–2356. https://doi.org/10.1039/c5lc90047f.

(164) Chen, X.; Bu, Y.; Li, H.; Wang, X.; Ao, J. P. The Fabrication of a Photo-Carrier Transfer Channel for a near Infrared up-Conversion Coupled Photocathodeviaa Sandwich-like Nanostructure. *J. Mater. Chem. C* **2021**, *9* (26), 8239–8248. https://doi.org/10.1039/d1tc01845k.

(165) Li, Y.; Bu, Y.; Jiang, F.; Dai, X.; Ao, J. P. Fabrication of Ultra-Sensitive Photoelectrochemical Aptamer Biosensor: Based on Semiconductor/DNA Interfacial Multifunctional Reconciliation via 2D-C3N4. *Biosens. Bioelectron.* **2020**, *150* (November 2019), 111903. https://doi.org/10.1016/j.bios.2019.111903.

(166) Weng, B.; Qi, M. Y.; Han, C.; Tang, Z. R.; Xu, Y. J. Photocorrosion Inhibition of Semiconductor-Based Photocatalysts: Basic Principle, Current Development, and Future Perspective. *ACS Catalysis*. American Chemical Society May 2019, pp 4642–4687. https://doi.org/10.1021/acscatal.9b00313.

(167) Gogoi, D.; Koyani, R.; Golder, A. K.; Peela, N. R. Enhanced Photocatalytic Hydrogen Evolution Using Green Carbon Quantum Dots Modified 1-D CdS Nanowires under Visible Light Irradiation. *Sol. Energy* **2020**, *208* (June), 966–977. https://doi.org/10.1016/j.solener.2020.08.061.

(168) Das, S.; Srivastava, V. C. Microfluidic-Based Photocatalytic Microreactor for Environmental Application: A Review of Fabrication Substrates and Techniques, and Operating Parameters. *Photochem. Photobiol. Sci.* **2016**, *15*, 714–730. https://doi.org/10.1039/c5pp00469a.

(169) Li, L.; Chen, R.; Zhu, X.; Wang, H.; Wang, Y.; Liao, Q.; Wang, D. Optofluidic Microreactors with TiO2-Coated Fiberglass. *ACS Appl. Mater. Interfaces* **2013**, *5*, 12548−12553. https://doi.org/10.1021/am403842b.

(170) Elani, Y.; Law, R. V.; Ces, O. Vesicle-Based Artificial Cells as Chemical Microreactors with Spatially Segregated Reaction Pathways. *Nat. Commun.* **2014**, *5*, 1–5. https://doi.org/10.1038/ncomms6305.

(171) Bühler, N.; Meier, K.; Reber, J. F. Photochemical Hydrogen Production with Cadmium Sulfide Suspensions. *J. Phys. Chem.* **1984**, *88* (15), 3261–3268. https://doi.org/10.1021/j150659a025.

(172) Chen, R.; Li, L.; Zhu, X.; Wang, H.; Liao, Q.; Zhang, M. Highly-Durable Opto Fl Uidic Microreactor for Photocatalytic Water Splitting. **2015**, *83*, 797–804.

(173) Liu, R. H.; Stremler, M. A.; Sharp, K. V.; Olsen, M. G.; Santiago, J. G.; Adrian, R. J.; Aref, H.; Beebe, D. J. Passive Mixing in a Three-Dimensional Serpentine Microchannel. *J. Microelectromechanical Syst.* **2000**, *9* (2), 190–197. https://doi.org/10.1109/84.846699.

(174) Lin, Y. Numerical Characterization of Simple Three-Dimensional Chaotic Micromixers. *Chem. Eng. J.* **2015**, *277*, 303–311. https://doi.org/10.1016/j.cej.2015.04.123.

(175) Nan, W.; Niu, Y.; Qin, H.; Cui, F.; Yang, Y.; Lai, R.; Lin, W.; Peng, X. Crystal

Structure Control of Zinc-Blende CdSe/CdS Core/Shell Nanocrystals: Synthesis and Structure-Dependent Optical Properties. *J. Am. Chem. Soc.* **2012**, *134* (48), 19685–19693. https://doi.org/10.1021/ja306651x.

(176) Li, K.; Han, M.; Chen, R.; Li, S. L.; Xie, S. L.; Mao, C.; Bu, X.; Cao, X. L.; Dong, L. Z.; Feng, P.; Lan, Y. Q. Hexagonal@Cubic CdS Core@Shell Nanorod Photocatalyst for Highly Active Production of H2with Unprecedented Stability. *Adv. Mater.* **2016**, *28* (40), 8906–8911. https://doi.org/10.1002/adma.201601047.

(177) Xu, Y.; Zhang, W. De. CdS/g-C3N4 Hybrids with Improved Photostability and Visible Light Photocatalytic Activity. *Eur. J. Inorg. Chem.* **2015**, *2015* (10), 1744–1751. https://doi.org/10.1002/ejic.201403193.

(178) Rasamani, K. D.; Li, Z.; Sun, Y. Significant Enhancement of Photocatalytic Water Splitting Enabled by Elimination of Surface Traps in Pt-Tipped CdSe Nanorods. *Nanoscale* **2016**, *8* (44), 18621–18625. https://doi.org/10.1039/c6nr06902a.

(179) Zhao, Y.; Han, Z.; Gao, G.; Zhang, W.; Qu, Y.; Zhu, H.; Zhu, P.; Wang, G. Dual Functions of CO2 Molecular Activation and 4f Levels as Electron Transport Bridge in Dysprosium Single Atom Composite Photocatalysts with Enhanced Visible-Light Photoactivities. *Adv. Funct. Mater.* **2021**, *31* (38), 1–10. https://doi.org/10.1002/adfm.202104976.

(180) Jin, J.; Yu, J.; Guo, D.; Cui, C.; Ho, W. A Hierarchical Z-Scheme CdS-WO3 Photocatalyst with Enhanced CO2 Reduction Activity. *Small* **2015**, *11* (39), 5262–5271. https://doi.org/10.1002/smll.201500926.

(181) Jiang, W.; Zong, X.; An, L.; Hua, S.; Miao, X.; Luan, S.; Wen, Y.; Tao, F. F.; Sun, Z. Consciously Constructing Heterojunction or Direct Z-Scheme Photocatalysts by Regulating Electron Flow Direction. *ACS Catal.* **2018**, *8* (3), 2209–2217.

https://doi.org/10.1021/acscatal.7b04323.

(182) Chen, S.; Hu, Y.; Meng, S.; Fu, X. Study on the Separation Mechanisms of Photogenerated Electrons and Holes for Composite Photocatalysts G-C3N4-WO3. *Appl. Catal. B Environ.* **2014**, *150–151*, 564–573. https://doi.org/10.1016/j.apcatb.2013.12.053.

(183) Yong, X.; Schoonen, M. A. A. The Absolute Energy Positions of Conduction and Valence Bands of Selected Semiconducting Minerals. *Am. Mineral.* **2000**, *85* (3–4), 543–556. https://doi.org/10.2138/am-2000-0416.

(184) Liu, J. Origin of High Photocatalytic Efficiency in Monolayer G-C3N4/CdS Heterostructure: A Hybrid DFT Study. *J. Phys. Chem. C* **2015**, *119* (51), 28417–28423. https://doi.org/10.1021/acs.jpcc.5b09092.

(185) Yan, H.; Huang, Y. Polymer Composites of Carbon Nitride and Poly(3-Hexylthiophene) to Achieve Enhanced Hydrogen Production from Water under Visible Light. *Chem. Commun.* **2011**, *47* (14), 4168–4170. https://doi.org/10.1039/c1cc10250h.

(186) Zhou, X.; Fang, Y.; Cai, X.; Zhang, S.; Yang, S.; Wang, H.; Zhong, X.; Fang, Y. In Situ Photodeposited Construction of Pt-CdS/g-C3N4-MnOx Composite Photocatalyst for Efficient Visible-Light-Driven Overall Water Splitting. *ACS Appl. Mater. Interfaces* **2020**, *12* (18), 20579–20588. https://doi.org/10.1021/acsami.0c04241.

(187) Liu, G.; Kolodziej, C.; Jin, R.; Qi, S.; Lou, Y.; Chen, J.; Jiang, D.; Zhao, Y.; Burda, C. MoS2-Stratified CdS-Cu2- XS Core-Shell Nanorods for Highly Efficient Photocatalytic Hydrogen Production. *ACS Nano* **2020**, *14* (5), 5468–5479. https://doi.org/10.1021/acsnano.9b09470.

(188) Pan, J.; Wang, P.; Wang, P.; Yu, Q.; Wang, J.; Song, C.; Zheng, Y.; Li, C. The Photocatalytic Overall Water Splitting Hydrogen Production of G-C3N4/ CdS Hollow Core–Shell Heterojunction via the HER/OER Matching of Pt/ MnOx. *Chem. Eng. J.* **2021**, *405* (May 2020). https://doi.org/10.1016/j.cej.2020.126622.

(189) Wang, X.; Wu, L.; Wang, Z.; Wu, H.; Zhou, X.; Ma, H.; Zhong, H.; Xing, Z.; Cai, G.; Jiang, C.; Ren, F. C/N Vacancy Co-Enhanced Visible-Light-Driven Hydrogen Evolution of g-C3N4 Nanosheets Through Controlled He+ Ion Irradiation. *Sol. RRL* **2019**, *3* (4), 1–9. https://doi.org/10.1002/solr.201800298.

(190) Liang, C.; Cui, M.; Zhao, W.; Dong, L.; Ma, S.; Liu, X.; Wang, D.; Jiang, Z.; Wang, F. Hybridizing Electron-Mediated H5PMo10V2O40 with CdS/g-C3N4 for Efficient Photocatalytic Performance of Z-Scheme Heterojunction in Wastewater Treatment. *Chemosphere* **2022**, *305* (June), 135315. https://doi.org/10.1016/j.chemosphere.2022.135315.

(191) Liang, Q.; Li, Z.; Huang, Z.; Kang, F.; Yang, Q. Holey Graphitic Carbon Nitride Nanosheets with Carbon Vacancies for Highly Improved Photocatalytic Hydrogen Production. **2015**, 6885–6892. https://doi.org/10.1002/adfm.201503221.

(192) Yuan, Y. J.; Chen, D.; Yu, Z. T.; Zou, Z. G. Cadmium Sulfide-Based Nanomaterials for Photocatalytic Hydrogen Production. *J. Mater. Chem. A* **2018**, *6* (25), 11606–11630. https://doi.org/10.1039/c8ta00671g.

(193) Stroock, A. D.; Dertinger, S. K. W.; Ajdari, A.; Mezić, I.; Stone, H. A.; Whitesides, G. M. Chaotic Mixer for Microchannels. *Science (80-.).* **2002**, *295* (5555), 647–651. https://doi.org/10.1126/science.1066238.

(194) Mengeaud, V.; Josserand, J.; Girault, H. H. Mixing Processes in a Zigzag Microchannel: Finite Element Simulations and Optical Study. *Anal. Chem.* **2002**, *74*

(16), 4279–4286. https://doi.org/10.1021/ac025642e.

(195) Liu, J.; Wei, X.; Sun, W.; Guan, X.; Zheng, X.; Li, J. Fabrication of S-Scheme CdS-g-C3N4-Graphene Aerogel Heterojunction for Enhanced Visible Light Driven Photocatalysis. *Environ. Res.* **2021**, *197* (March), 111136. https://doi.org/10.1016/j.envres.2021.111136.

(196) Wang, J.; Pan, R.; Hao, Q.; Gao, Y.; Ye, J.; Wu, Y.; van Ree, T. Constructing Defect-Mediated CdS/g-C3N4 by an In-Situ Interlocking Strategy for Cocatalyst-Free Photocatalytic H2 Production. *Appl. Surf. Sci.* **2022**, *599* (June), 153875. https://doi.org/10.1016/j.apsusc.2022.153875.

(197) Yang, H.; Zhang, J. feng; Dai, K. Organic Amine Surface Modified One-Dimensional CdSe0.8S0.2-Diethylenetriamine/Two-Dimensional SnNb2O6 S-Scheme Heterojunction with Promoted Visible-Light-Driven Photocatalytic CO2 Reduction. *Chinese J. Catal.* **2022**, *43* (2), 255–264. https://doi.org/10.1016/S1872-2067(20)63784-6.

(198) Li, X.; Wang, Z.; Zhang, J.; Dai, K.; Fan, K.; Dawson, G. Branch-like CdxZn1-XSe/Cu2O@Cu Step-Scheme Heterojunction for CO2 Photoreduction. *Mater. Today Phys.* **2022**, *26* (May), 1–10. https://doi.org/10.1016/j.mtphys.2022.100729.

(199) Dai, K.; Lv, J.; Zhang, J.; Zhu, G.; Geng, L.; Liang, C. Efficient Visible-Light-Driven Splitting of Water into Hydrogen over Surface-Fluorinated Anatase TiO2 Nanosheets with Exposed {001} Facets/Layered CdS-Diethylenetriamine Nanobelts. *ACS Sustain. Chem. Eng.* **2018**, *6* (10), 12817–12826. https://doi.org/10.1021/acssuschemeng.8b02064.

(200) Therriault, D.; White, S. R.; Lewis, J. A. Chaotic Mixing in Three-Dimensional Microvascular Networks Fabricated by Direct-Write Assembly. *Nat. Mater.* **2003**, *2*

(4), 265–271. https://doi.org/10.1038/nmat863.

(201) Janasek, D.; Franzke, J.; Manz, A. Scaling and the Design of Miniaturized Chemical-Analysis Systems. *Nature* **2006**, *442* (7101), 374–380. https://doi.org/10.1038/nature05059.

(202) Sharma, V. K.; Bhowmik, R.; Tiwari, P.; Singh, A. Pore-Scale Investigation of Immiscible Fluid Displacement Process in Randomly Distributed Bead-Based Porous Micromodels Using Micro-PIV. *J. Pet. Sci. Eng.* **2022**, *212* (February), 110301. https://doi.org/10.1016/j.petrol.2022.110301.

(203) Goswami, T.; Bhatt, H.; Yadav, D. K.; Ghosh, H. N. Interfacing G-C3N4 Nanosheets with CdS Nanorods for Enhanced Photocatalytic Hydrogen Evolution: An Ultrafast Investigation. *J. Phys. Chem. B* **2022**, *126* (2), 572–580. https://doi.org/10.1021/acs.jpcb.1c10336.

(204) Belakehal, R.; Atacan, K.; Güy, N.; Megriche, A.; Özacar, M. Fabrication of Heterostructured CdS/g-C3N4/ZnFe2O4 Nanocomposite Synthesized through Ultrasonic-Assisted Method for Efficient Photocatalytic Hydrogen Production. *Appl. Surf. Sci.* **2022**, *602* (June). https://doi.org/10.1016/j.apsusc.2022.154315.